To the Graduate Council:

I am submitting herewith a dissertation written by Qing He entitled "Study of High Temperature Superconducting Films with High Critical Current Density on Metallic Substrates." I have examined the final copy of this dissertation for form and content and recommend that it be accepted in partial fulfillment of the requirements for the degree of Doctor of Philosophy, with a major in Metallurgical Engineering.

A. J. Pedraza, Major Professor

We have read this dissertation

and recommend its acceptance:

Charlie R. Brooks

David Clutter

James R. Thompson

D. H. Lowndes

Accepted for the Council:

Associate Vice Chancellor

and Dean of The Graduate School

Study of High Temperature Superconducting Films with High Critical Current Density on Metallic Substrates

A Dissertation

Presented for

the Doctor of Philosophy

Degree

The University of Tennessee, Knoxville

Qing He

May 1998

To

my wife, Yan

ACKNOWLEDGMENTS

I would like to express my sincere appreciation to my major professor, Dr. A. J. Pedraza, and my thesis professor, Dr. D. K. Christen, for their excellent guidance and invaluable help throughout the research of this thesis. I am indebted to Dr. J. R. Thompson for giving me the opportunity for the Ph.D. study and for the continued support in the past five and half years. My appreciation also goes to my other committee members, Dr. D. H. Lowndes and Dr. C. R. Brooks for their careful review of this thesis and useful suggestions.

My deepest gratitude is extended to my colleagues in ORNL: D. P. Norton, J. D. Budai, C. E. Klabunde, R. Feenstra, H. R. Kerchner, D. M. Kroeger, A. Goyal, M. Paranthaman, E. D. Specht, and D. F. Lee. I would also like to thank my collaborators at the GE R&D Center: Dr. J. E. Tkaczyk and Dr. J. DeLuca.

I wish to give special thanks to my wife, Yan, my son, David, my father, Mr. X. J. He, and my mother, the late Mrs. S. Y. Yu, without whose unending support, patience, and understanding this work would have been impossible.

This research was cosponsored by the DOE Division of Materials Sciences and by the DOE Office of Advanced Utility Concepts, Superconductivity Technology Program, both under Contract No. DE-AC05-84OR21400 with Lockheed Martin Energy Research Corporation.

ABSTRACT

High temperature superconductors (HTS) hold great promise for widespread commercial applications, most of which require the fabrication of flexible long HTS tapes with high critical current density J_c values. In this thesis, two new processes have been developed. One is a spin-coating process, which can provide a simple, inexpensive and rapid means to fabricate *c*-axis textured high J_c $Tl_1Ba_2Ca_2Cu_3O_9$ (Tl-1223) thick films on flexible polycrystalline Ag substrates. A limited matrix study has been conducted to determine how the Tl-1223 films are affected by the Tl-source temperature, sample temperature, and reaction time. The pressing process is the key point in the technique to get *c*-axis orientation and high J_c value for the Tl-1223 films. The superconducting properties, microstructure, and structural orientation of the Tl-1223 films have been analyzed. The other process is RABiTS (Rolling-Assisted Biaxially Textured Substrates), by which biaxially textured HTS films with high J_c values could be grown on buffered flexible Ni substrates. The deposition of biaxially textured buffer layers on the aligned Ni substrates plays an important role in the RABiTS process, which should ensure epitaxy and chemical compatibility of the buffer layers with both the underlying nickel and the final HTS layer. To grow the biaxially oriented buffer layers on the Ni substrates, two approaches have been taken. The first is to grow the biaxially oriented metal or oxide buffer layers, such as Ag and CeO_2, on the Ni tapes by using oxidation-resistant Pd (or Pt) film as an intermediate layer, which transfers the biaxially oriented structure from Ni to the top buffer layers. The second approach is to grow biaxially oriented

oxide films, such as CeO_2 and $LaNiO_3$, directly on the Ni substrate by introducing forming gas ($Ar/4\%H_2$) which might prevent the formation of NiO while assuring stability of the sputtered oxides. It is found that some biaxially textured films, such as Pd and CeO_2, can be grown at room temperature and that post-annealing can improve the biaxial orientations. The effects of deposition temperature on the degree of biaxial orientations of the CeO_2 films were investigated. SEM observations show that cracking may occur on the CeO_2 buffer layer during oxygen-annealing at high temperature. To prevent the cracking, an additional YSZ layer is deposited on the CeO_2 buffered Ni substrates. It is found that good Ni surface smoothness can improve the out-of-plane orientation of the deposited films. Electrically conductive $LaNiO_3$ buffer layers with biaxial orientations have also been grown on the textured Ni at low temperature. Subsequent oxygen anneals at 850°C neither change the biaxial orientations of the film significantly nor cause any cracks on the surface of the films. The resistivity of the $LaNiO_3$ films can be reduced by oxygen-annealing at high temperature. Biaxially textured YBCO films with J_c values over 10^6 A/cm^2 at 77 K have been successfully grown on the buffered flexible Ni tapes.

TABLE OF CONTENTS

Chapter		Page
1.	INTRODUCTION	1
	1.1 Discovery of HTS	1
	1.2 Critical currents for both LTS and HTS	1
	1.3 Applications of HTS	6
	1.4 Problems for HTS applications	8
2.	CONCEPTUAL DEVELOPMENT	9
	2.1 Tl-1223 films on metals	9
	2.1.1 Tl family	9
	2.1.2 Metallic substrates for Tl-1223 films	11
	2.1.3 Methods to deposit Tl-1223 films	12
	2.2 Biaxially textured HTS films on metals	14
	2.2.1 Weak link problems	14
	2.2.2 Previous efforts on biaxially textured HTS films on metals	17
	2.2.3 New approach: RABiTS technique	19
	2.2.4 Requirements for metallic substrates	21
	2.2.5 Requirements for buffer layers	22
3.	EXPERIMENTAL	25
	3.1 Spin-coating method for Tl-1223 thick films on Ag	25

3.1.1 Precursor film depositions 25

3.1.2 Thallination 26

3.1.3 Property measurements of the Tl-1223 films 26

3.2 RABiTS technique 28

3.2.1 Preparations of biaxially textured Ni substrates 28

3.2.2 Depositions of buffer layers on Ni by sputtering 29

3.2.3 Depositions of YBCO films on buffered Ni substrates 31

3.2.4 Property measurements of the films 31

4. RESULTS AND DISCUSSION 32

4.1 Tl-1223 films on Ag by spin-coating 32

4.1.1 Effects of T_{source}, T_{sample}, and the reaction time 32

4.1.2 Effect of the pressing process 41

4.1.3 Superconducting properties of the Tl thick film 47

4.2 RABiTS technique 53

4.2.1 Noble metal buffer layers on Ni tapes 53

4.2.2 CeO_2 buffer layers on Pd-buffered Ni tapes 63

4.2.3 CeO_2 buffer layer grown directly on Ni using forming gas . . . 69

4.2.4 Conductive $LaNiO_3$ buffer layers 75

4.2.5 YSZ buffer layer on the buffered Ni tapes 83

4.2.6 The YBCO films on the buffered Ni tapes 86

5. CONCLUSION 96

REFERENCES 98

APPENDICES 107

1. Calculation of the depairing current density J_0 value at 0 K 108

2. Calculation of the depairing current density J_0 value at 77 K 109

3. Calculation of the lattice mismatches 110

VITA 111

LIST OF TABLES AND FIGURES

List of Tables

Table 1 List of T_c, H_c, H_{c2}, λ, ξ, and J_0 values for some superconductors. 3

Table 2 Comparison of typical J_c values for HTS and LTS. 5

Table 3 Some potential applications of HTS. 7

Table 4 Crystal structure, lattice constants, thermal expansion coefficient, melting point, and lattice mismatching with Ni and YBCO for some candidate buffer layers. The lattice mismatch is calculated as detailed in appendix 3. 23

List of Figures

Figure 1 Increase of the superconducting transition temperature T_c with time, reflecting the giant steps achieved by scientists in recent years. 2

Figure 2 Comparison of irreversibility lines for major HTS systems. The magnetic field H is parallel to the *c*-axis of the HTS samples. 10

Figure 3 J_c values for different deposition techniques. The interesting area is the Tl-1223 thick film (>10 μm) with appropriate high J_c values. 13

Figure 4 The J_c value across a grain boundary decreases rapidly as the misorientation angle is over 10° for three different grain boundary geometries: [001] tilt boundary, [100] tilt boundary, and [100] twist boundary. 16

Figure 5 Schematic relationship between the J_c value and the structural orientation in a HTS. 18

Figure 6 Components of the RABiTS structure: sharply biaxially-textured flexible metal substrate, biaxially textured buffer layers, and epitaxial HTS film with high J_c value. 20

Figure 7 Diagram illustrating the essential features of the two-zone Tl-reaction furnace designed for the fabrication of long flexible high J_c Tl-1223 tapes. 27

Figure 8 Tl source temperature T_{source} dependence of Tl content X in $Tl_xBa_2Ca_2Cu_3O_{7.5+1.5x}$ spin-coated thick film on Ag substrate at T_{sample} of 860°C and 2.5 hours reaction time. 33

Figure 9 Reaction time dependence of Tl content X in $Tl_xBa_2Ca_2Cu_3O_{7.5+1.5x}$ spin-coated

films on Ag substrate at T_{sample} of 860°C and T_{source} of 740°C. 35

Figure 10 Sample temperature T_{sample} dependence on Tl content X in $Tl_xBa_2Ca_2Cu_3O_{7.5+1.5x}$ spin-coated thick film on Ag substrate, at T_{source} of 740°C and 2.5 hour reaction time. 37

Figure 11 (a). SEM micrograph showing the surface morphology of Tl-1223 thick film on Ag, after treatment at T_{sample} of 866°C; (b). SEM micrograph showing the surface morphology of Tl-1223 thick film on Ag, after treatment at T_{sample} of 851°C. 38

Figure 12 (a). SEM micrograph of the surface morphology of spin-coated Tl-1223 thick films on Ag, after annealing at T_{sample} of 860°C; (b). SEM micrograph of a different view of the same sample. Notice a small amount of fan-like structure.. 39

Figure 13 Transport J_c value at 77 K as a function of T_{sample} for a spin-coated Tl-1223 thick film on Ag. T_{source} was maintained at 740°C and the reaction time was about 2.5 hours. The highest J_c value is obtained at around 857°C. 40

Figure 14 X-ray diffraction pattern from a spin-coated Tl-1223 thick film on Ag without pressing process, showing the Tl-1223 phase with random orientation. . 42

Figure 15 (a). Surface morphology of spin-coated Tl-1223 thick film on Ag without pressing process, showing rough surface; (b). Surface morphology of the spin-coated Tl-1223 thick film on Ag with pressing process, showing smooth surface. 43

Figure 16 Surface profiles of spin-coated Tl-1223 thick films on Ag: upper curve shows

the rough surface of a spin-coated thick film without pressing process, lower surface profile curve illustrates a flat surface of a spin-coated Tl-1223 thick films with pressing process.. 44

Figure 17 (a). SEM micrograph of a cross-section of spin-coated Tl-1223 thick film on Ag substrate, after annealing at 860°C. (b). SEM micrograph of the same cross-section at higher magnification. 45

Figure 18 X-ray diffraction pattern of spin-coated and pressed Tl-1223 thick film on Ag. A high degree of *c*-axis texture is indicated by the presence of only the (00*l*) peaks for the Tl-1223 phase. The rocking curve shows the FWHM for the (006) refection is 3.8°. 46

Figure 19 X-ray ϕ-scan from spin-coated Tl-1223 film on Ag substrate. Strong local in-plane texture is observed using a beam size of 0.5×0.5 mm^2. 48

Figure 20 Temperature dependence of the transport J_c value from spin-coated Tl-1223 thick films on Ag substrates. 49

Figure 21 Magnetic field, H, dependence of transport J_c values at 77 K with H parallel to the nominal *c*-axis for spin-coated Tl-1223 thick film on Ag (Tl-1223), spray-pyrolyzed Tl-1223 thick film on YSZ (Tl-1223/YSZ), and powder-in-tube Tl-1223 tape (Tl-1223-PIT). 50

Figure 22 Transport J_c values at 40 K as a function of applied magnetic field H parallel to *c*-axis for spin-coated Tl-1223 thick film on Ag, spray-pyrolyzed Tl-1223 thick film on YSZ (Tl-1223/YSZ), powder-in-tube Bi-2223 tape (Bi-2223-PIT), and powder-in-tube Tl-1223 tape (Tl-1223-PIT). 52

Figure 23 X-ray θ-2θ scan for the Ag/Pd/Ni laminates, revealing the presence of (00*l*) peaks only. The Pd was deposited at 500°C followed by Ag deposition at 300°C. 54

Figure 24 X-ray ϕ-scans for Ag (202), Pd (202), and Ni (202) in the Ag/Pd/Ni laminates, revealing clear fourfold symmetry for each layer. 55

Figure 25 X-ray ω-scans for the Ag/Pd/Ni laminates, showing the progressive improvement of out-of-plane orientation in subsequent layers. 57

Figure 26 X-ray θ-2θ scan, ω-scan, and ϕ-scan for the Pt/Ni laminates, revealing that the Pt film has good out-of-plane and in-plane orientations. 58

Figure 27 X-ray ϕ-scans through Pd (202) for the as-deposited Pd film and for the post-annealed Pd film. In-plane oriented Pd film can be grown on the Ni substrate at room temperature and the post-annealing can improve the in-plane orientation of the Pd films. 59

Figure 28 X-ray ω-scans through Pd (002) for the as-deposited Pd film and the post-annealed Pd film on the Ni. Post-annealing can also improve the out-of-plane orientation of the Pd film. 60

Figure 29 X-ray ω-scans through the Pd (002) reflection for the Pd films on polished and unpolished Ni substrate, showing that polishing can improve the out-of-plane alignment of the Pd film. 62

Figure 30 (a). X-ray θ-2θ scans for the room-temperature-deposited CeO_2 on Pd-buffered Ni substrate; (b). X-ray θ-2θ scan for the same sample that has been annealed at 700°C after deposition. 64

Figure 31 (a). ω-scans through CeO_2 (002) for as-deposited CeO_2 on Pd-buffered Ni with FWHM of 10° and for post-annealed sample with FWHM of 8°. (b). ϕ-scans through CeO_2 (202) for as-deposited CeO_2 on Pd-buffered Ni with FWHM of 15.6° and for post-annealed sample with FWHM of 11.5°. . . 65

Figure 32 Dependence on deposition temperature of the FWHM values of x-ray ω-scans through CeO_2 (002) and ϕ-scans through CeO_2 (202) for CeO_2 films deposited on Pd-buffered Ni tape. 66

Figure 33 SEM micrograph showing the surface morphology of CeO_2 film on Pd-buffered Ni substrate, annealed at 750°C for 3 hours under 1 m Torr oxygen pressure. The film surface is smooth, but shows some cracks after the high-temperature treatment. 68

Figure 34 SEM micrograph showing the surface morphology of CeO_2 film on Pd-buffered Ni substrate. The initial layer of CeO_2 film was grown at low temperature and followed by high temperature (750°C) deposition. Only small amounts of cracks remained on the CeO_2 film. 70

Figure 35 X-ray θ-2θ scan for the CeO_2 film directly deposited on the Ni substrate by using forming gas as a sputtering gas. The inset shows an x-ray ϕ-scan through the CeO_2 (202) reflection with FWHM of 7.8°. 71

Figure 36 Stability of several metal oxides as a function of temperature and hydrogen partial pressure $P(H_2)$. 72

Figure 37 Deposition temperature dependence of the FWHM from the CeO_2 (002) rocking curve for CeO_2 films deposited on YSZ (001) single crystals in

Ar+4%H_2 and in Ar+10%O_2, respectively. 74

Figure 38 X-ray θ-2θ scan of $LaNiO_3$ laminate, indicating the presence of (00*l*) peaks only. The inset shows ω-scan through $LaNiO_3$ (200), revealing good out-of-plane orientation of 5° FWHM. 77

Figure 39 X-ray φ-scans through $LaNiO_3$ (202) for: (a). as-deposited $LaNiO_3$ film; (b). $LaNiO_3$/Ni sample annealed at 750°C in 100 m Torr oxygen pressure for 1 hour; and (c). $LaNiO_3$ sample annealed at 850°C in 100 m Torr oxygen pressure for 1 hour. 78

Figure 40 SEM micrograph of $LaNiO_3$ sample annealed at 850°C in 100 m Torr oxygen pressure for 1 hour, revealing smooth and crack-free surface. 79

Figure 41 Temperature dependence of the resistance of $LaNiO_3$ (100) on $SrTiO_3$ single crystal substrate which was annealed at different temperature in 1 atm oxygen. 81

Figure 42 Temperature dependence of the resistance of $LaNiO_3$ (100) on $SrTiO_3$ single crystal substrate after annealing at 400°C under different oxygen partial pressures. 82

Figure 43 X-ray θ-2θ scan for the YSZ/CeO_2/Ni laminates, indicating the presence of (00*l*) reflections only for CeO_2 and YSZ films. The YSZ was deposited at 780°C. 84

Figure 44 SEM micrograph showing the surface morphology of YSZ film on CeO_2/Pd-buffered Ni substrate, annealed at 750°C in O_2 partial pressure, revealing no cracks on the YSZ surface. 85

Figure 45 X-ray θ-2θ scan for YSZ/$LaNiO_3$/Ni laminate, showing *c*-axis orientation for each layer. The FWHM for the ϕ-scan through YSZ (202) is 16°. 87

Figure 46 X-ray ϕ-scans showing the transference of texture through the various multilayers of RABiTS substrates: (a). YBCO/Ag/Pd/Ni; (b). YBCO/CeO_2/Ag/Pd/Ni; and (c). YBCO/YSZ/CeO_2/Pd/Ni. 88

Figure 47 X-ray θ-2θ scan for YBCO/YSZ/CeO_2/Ni multilayer structure, showing good *c*-axis orientation for each layer. 90

Figure 48 X-ray rocking curves and ϕ-scans for YBCO/YSZ/CeO_2/Ni laminate showing the out-of-plane and in-plane orientations for each layer. 91

Figure 49 Magnetic field dependence of J_c (77 K) value for YBCO/YSZ/CeO_2/Ni laminate, YBCO/$SrTiO_3$ (001), Tl-1223/YSZ (polycrystalline), and Bi-2223/Ag tape. 92

Figure 50 Temperature dependence of J_c, measured at 0, 3, and 8 T, for YBCO/YSZ/CeO_2/Ni laminate. For comparison, data are also shown for Bi-2212/Ag wire, Bi-2223/Ag tape, Tl-1223/YSZ (polycrystalline), NbTi, and Nb_3Sn. 94

LIST OF SYMBOLS AND ABBREVIATIONS

HTS	High Temperature Superconductors (or Superconductivity)
LTS	Low Temperature Superconductors
I_c	critical current
J_c	critical current density
T_c	critical transition temperature
H_{c2}	upper critical magnetic field
J_0	depairing critical current density
YBCO	$Y_1Ba_2Cu_3O_{7-y}$
Tl-1223	$Tl_1Ba_2Ca_2Cu_3O_y$
Bi-2223	$Bi_2Sr_2Ca_2Cu_3O_y$
J_e	engineering J_c value which is the I_c value per unit area of the total cross-section for the HTS conductors.
PIT	powder-in-tube process
RT	Room Temperature
sccm	standard cubic centimeter per minute
rms	root-mean-square
AFM	Atomic Force Microscopy
PLD	Pulsed Laser Deposition
r.f.	radio frequency

d.c.	direct current
X	Tl content in the spin-coated $Tl_xBa_2Ca_2Cu_3O_{7.5+1.5x}$ thick film on Ag
SEM	Scanning Electronic Microscopy
RBS	Rutherford Backscattering Spectrometry
IBAD	Ion beam-assisted deposition
RABiTS	Rolling-Assisted Biaxially Textured Substrate
FWHM	Full Width at Half Maximum
EBSP	Electron Back Scattering Patterns
H_c	thermodynamic critical magnetic field
λ	Ginzburg-Landau penetration depth
ξ	Ginzburg-Landau coherence length
Φ_0	flux quantum equal to 2.07×10^{-7} Gcm^2

1. INTRODUCTION

1.1 Discovery of HTS

Like a minor earthquake, the discovery of high-temperature superconductivity (HTS) of $(La\text{-}Ba)_2CuO_4$ with T_c values in the 30 K range by G. J. Bednorz and K. A. Muller[1] in 1986 sent a shock wave through the research world, exciting scientists to explore superconductors with higher critical transition temperature T_c. Subsequently, $Y_1Ba_2Cu_3O_{7-y}$ with T_c at 85-98 K, BiSrCaCuO with T_c of 110 K, TlBaCaCuO with T_c of 125 K, and HgBaCaCuO with T_c of 135 K, were discovered by P. Chu *et al.*,[2,3] H. Maeda *et al.*,[4] Z. Z. Sheng *et al.*,[5] and S. N. Putilin *et al.*,[6,7] respectively. When the T_c of Hg system superconductors is measured at high pressure, the T_c value can be as high as 164 K. The curve of T_c versus date in Figure 1 reflects the giant steps achieved by researchers in recent years. Very recently, C. W. Chu *et al.* discovered Tl (or Hg)-free $Ba_2Ca_{n-1}Cu_nO_x$ superconductor with T_c up to 126 K.[8] The dream of early scientists to pursue superconductors that can work in liquid nitrogen (77 K at normal atmospheric pressure) has been realized.

1.2 Critical currents for both LTS and HTS

Generally speaking, new HTS have not only higher T_c values, but also higher upper critical magnetic field H_{c2} and higher critical current density J_c than low-T_c superconductors (LTS). Typically, the H_{c2} for HTS is over 10 times higher than that for LTS,[9] as shown in Table 1. The theoretical highest critical current density is the depairing current density which

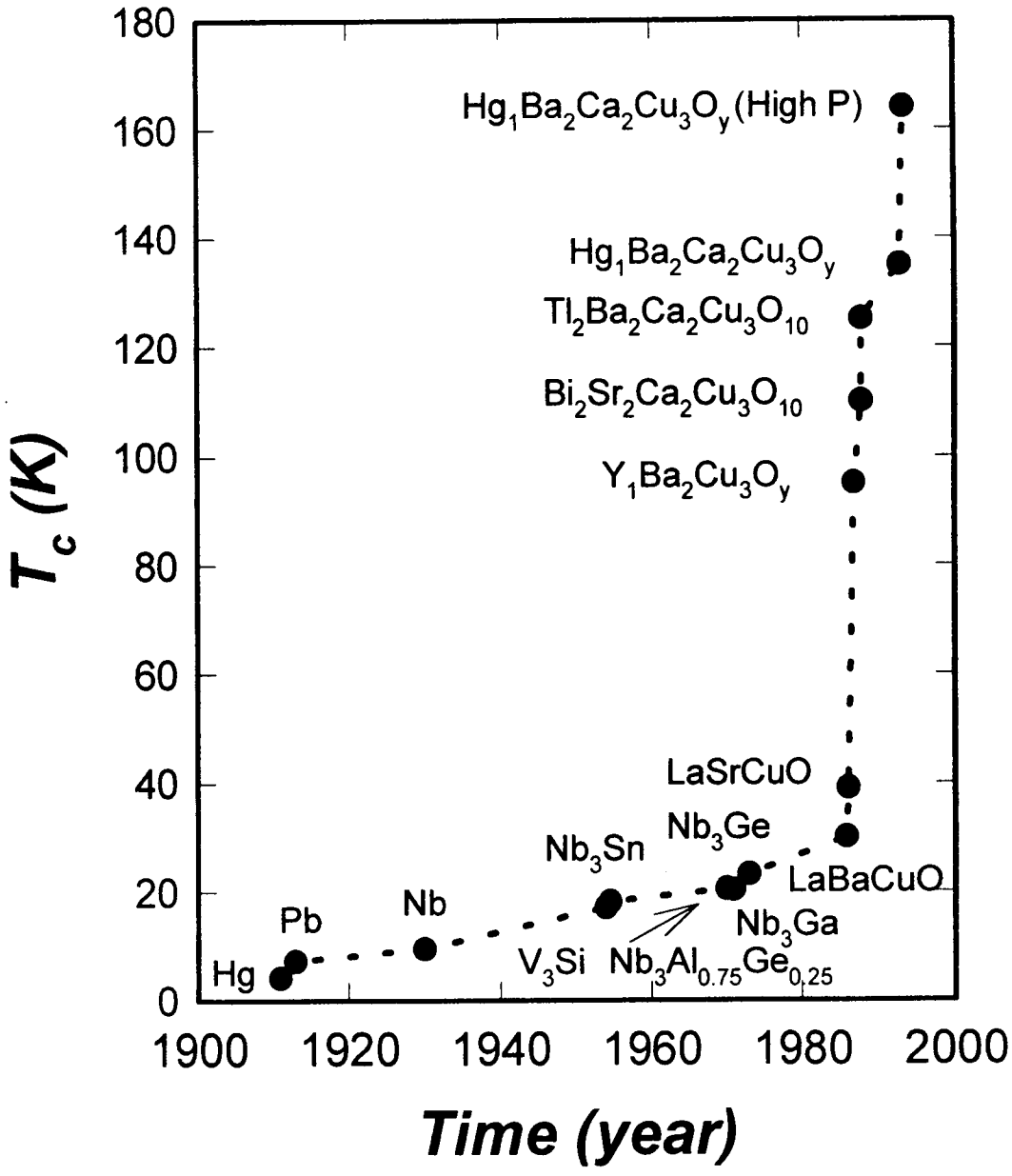


Figure 1 Increase of the superconducting transition temperature T_c with time, reflecting the giant steps achieved by scientists in recent years.

Table 1. critical transition temperature (T_c), thermodynamic critical magnetic field (H_c), upper critical magnetic field (H_{c2}), GL penetration depth (λ), GL coherence length(ξ), and depairing critical current density(J_0) values for both LTS and HTS materials. The J_0 values at 0 K and at 77 K are calculated according to the formulas in appendices 1 and 2.

LTS and HTS	T_c (K)	H_c (G)	H_{c2} (G)	λ (cm)	ξ (cm)	J_0 (0 K) (A/cm^2)	J_0 (77 K) (A/cm^2)	ref.
Nb-Ti	9.3	1.3×10^{3}	5.9×10^{4}	2.5×10^{-5}	7.5×10^{-7}	2.2×10^{7}	-	[10]
V_3Si	17	4.5×10^{3}	1.5×10^{5}	1.1×10^{-5}	4.7×10^{-7}	1.8×10^{8}	-	[10]
Nb_3Sn	18	4.5×10^{3}	1.2×10^{5}	1.0×10^{-5}	5.2×10^{-7}	1.9×10^{8}	-	[11]
Y-123	90	1.1×10^{4}	1.4×10^{6}	1.4×10^{-5}	1.5×10^{-7}	3.4×10^{8}	7.2×10^{7}	[12]
Bi-2212	85	1.0×10^{4}	5.5×10^{6}	3.0×10^{-5}	7.8×10^{-8}	1.4×10^{8}	1.7×10^{7}	[13]
Bi-2223	105	1.0×10^{4}	2.9×10^{6}	2.2×10^{-5}	1.1×10^{-7}	2.0×10^{8}	8.7×10^{7}	[13]
Tl-2223	122	1.0×10^{4}	1.7×10^{6}	1.7×10^{-5}	1.4×10^{-7}	2.5×10^{8}	1.5×10^{8}	[14]
Hg-1201	94	9.5×10^{3}	7.5×10^{5}	1.2×10^{-5}	2.1×10^{-7}	3.5×10^{8}	9.9×10^{7}	[15]
Hg-1212	120	9.9×10^{3}	8.2×10^{5}	1.2×10^{-5}	2.0×10^{-7}	3.7×10^{8}	2.2×10^{8}	[16]
Hg-1223	135	3.3×10^{4}	1.5×10^{6}	1.5×10^{-5}	1.5×10^{-7}	9.5×10^{8}	2.1×10^{8}	[17]

is limited by the pair breaking of the superconducting state induced by the current itself. Above this current, the superconductor is driven normal. The depairing critical current density J_0 at 0 K for both LTS and HTS and J_0 at 77 K for HTS have been calculated according to the formulas in appendices 1 and 2, and are shown in the Table 1. We can see that the values of J_0 at 0 K for both LTS and HTS have about the same order of magnitude. For each HTS, the value of J_0 at 77 K is a factor of 3-10 lower than that at 0 K. Table 2 shows the J_c values typically measured for some LTS and HTS materials. From the comparison of the J_0 and J_c values in Tables 1 and 2, we can see that the measured J_c at 77 K for each HTS is about one or two orders lower than J_0 (77 K), reflecting the fact that the J_c, which represents the critical depinning current density, is always bounded by J_0. For example, for YBCO, the calculated J_0 values are in the range 10^8-10^9 at 4.2 K, and 10^7-10^8 A/cm^2 at 77 K, while the measured J_c values are only 5×10^7 A/cm^2 at 4.2 K, and 5×10^6 A/cm^2 at 77 K. This may be understood, since the self-field J_c can be limited by the depinning of self-generated vortices. The approximate flux density of such a vortex structure likely will not exceed ~100 G at 77 K. therefore, either thermally-activated or Lorentz force generated depinning of these self-vortices may limit J_c (H=0) to the observed levels of $J_c/J_0 \approx 0.1$.

From Table 2, we found the YBCO films have J_c values of ~5×10^7 A/cm^2 at 4.2 K and ~5×10^6 A/cm^2 at 77 K. It is curious to find that J_c values of YBCO films at 4.2 K and 77 K are about 30 times and 100-1000 times larger than those of the YBCO single crystals, respectively. The reason is probably associated with details of flux pinning microstructural defects, which apparently is better in as-grown films than in single crystals.

Comparing the J_c values of Ag-sheathed Bi-2223 at 4.2 K in zero and in high magnetic

Table 2: Comparison of typical J_c values for HTS and LTS. Note: the J_c values for Nb-Ti, Nb_3Sn, Y-system, Bi-system, and Tl-system are from transport measurements, while the J_c values for Hg-system are from magnetic measurements.

Super-conductor	J_c (A /cm^2) in zero or low field		J_c (A /cm^2) in high field (H‖*c*-axis)		Ref.
	at 4.2 K	at 77 K	at 4.2 K	at 77 K	
Nb-Ti (bulk)	2×10^5	-	9×10^4 in 4 T	-	18
Nb_3Sn (bulk)	10^7	-	3×10^5 in 4 T	-	18
Y-123 (film)	5×10^7	5×10^6	5×10^6 in 4 T	1×10^3 in 4 T	19
Y-123 (bulk)	1.5×10^6	2×10^4		1×10^3 in 4 T	20
Bi-2212(film)	10^7	5×10^5	10^6 in 4 T	10^2 in 4 T	18
Bi-2223 (tape)	1.3×10^5	5.8×10^4	1.0×10^5 in 23 T	-	21
Tl-1223 (film)	-	1.1×10^6	-	2×10^3 in 3T	22
Hg-1201 (bulk)	2×10^7	1.5×10^5	4×10^6 in 5T	2×10^5 in 0.5T	23
Hg-1212 (bulk)	$\sim10^8$	9×10^6	1.5×10^7 in 5 T	2×10^6 in 5 T	24
Hg-1223 (bulk)	1.6×10^7	1.2×10^6	5×10^6 in 5 T	1×10^4 in 1 T	23

field, we find that J_c is essentially independent of the field up to 23 T, while it decreases rapidly for Nb-Ti and Nb_3Sn. The reason is that H_{c2} at 4.2 K is much larger than 23 T for Bi-2223, while for LTS, the H_{c2} (T) line is being approached, so that J_c is reduced.

Although the zero-field J_c values at 4.2 K for HTS are a little larger than or equal to those for LTS, the J_c values for HTS in the high magnetic field at 4.2 K are much superior to those for LTS. It is also noticed that, in zero magnetic field, the HTS materials in liquid nitrogen have about the same J_c value as LTS used in liquid helium. Therefore, HTS could be used either in liquid nitrogen or in liquid helium to replace some LTS wires, if some day we can fabricate long flexible HTS wires with high J_c value.

1.3 Applications of HTS

Due to their high T_c, high J_c and high H_{c2}, the HTS materials hold great promise for widespread commercial applications, as shown in Table 3. The worldwide markets for HTS devices over the next two decades could be over $120 billion, as derived from the report from the 5th International Superconductivity Industrial Summit (ISS-5) meeting, held in Japan on May 1996. One of the major applications of HTS is in the electric power industry. For example, the global market for HTS motors, HTS transmission lines, and HTS transformers are expected to exceed $10 billion/year, $2.5 billion/year, and $1 billion/year, respectively, within the next 20 years. The extensive commercialization of HTS could result in a new industrial revolution. Due to the large market attraction, the U.S. government has been eagerly sponsoring R&D activities on HTS materials. In fiscal year 1995, for example, about $210 million was spent on both LTS and HTS R&D. One key to the success of such

Table 3: Some potential applications of HTS.

Fields	Potential Applications of HTS
Electric Power Industry	**transmission lines, motors, generators, fault current limiters, fusion magnets, transformers, inductors, superconducting magnetic energy storage (SMES);**
Transportation Industry	**magnetically levitated trains, marine propulsion;**
Medical Industry	**magnetic resonance imaging (MRI) equipment, biotechnical engineering;**
Electronic Industry	**SQUIDs, transistors, Josephson Junction devices, circuitry connections, magnetometers, very stable voltage sources, infrared sensors, analog signal processing devices, magnetic shielding devices, hybrid microwave devices (e.g., resonators, filters, delay lines, antennas, switches limiters);**
Other Industries	**magnets for SQUID, magnets for treatment of hazardous wastes, accelerator magnets, magnetic separators, rotating machinery, bearings.**

widespread commercial exploitation of the HTS is the development of low-cost processes for the fabrication of long flexible HTS tape with high J_c value.

1.4 Problems for HTS applications

Over ten years have passed since the discovery of HTS and there is almost no commercial power application of HTS. This is due to some intrinsic problems in the HTS materials which hinder fabrication of flexible, long, HTS wires with high J_c values. These principal problems can be classified as follows: (1). brittleness of these materials which hinder the fabrication of flexible, HTS wires; (2). high anisotropy in both structure and superconducting properties; (3). high synthesizing temperature which results in chemical reaction with most metallic substrates; (4). giant flux-creep in mixed state within grains;[25, 26, 27, 28] and (5). weak link current flow phenomenon at inter-grain boundaries. In the past several years, my major research work has been focused on how to overcome these problems in order to fabricate flexible long HTS wires with high-J_c values.

2. CONCEPTUAL DEVELOPMENT

2.1 Tl-1223 films on metals

2.1.1 Tl family

Among the well-known HTS, the Tl family of superconductors is attractive for potential applications, partially because of their high T_c values. There are two main homologous series, $TlBa_2Ca_{n-1}Cu_nO_{2n+3}$ (for $n = 1, 2, 3, 4, 5$)[29, 30, 31, 32] and $Tl_2Ba_2Ca_{n-1}Cu_nO_{2n+4}$ (for $n = 1, 2, 3$),[33, 34] n being the number of consecutive Cu-O layers within a unit cell. The elements Tl and Ba in the phases of the two series can also be partially or completely replaced by Pb (or Bi) and Sr, respectively. Among the Tl family members, single Tl-O layer superconductors $Tl_1Ba_2Ca_2Cu_3O_9$ (Tl-1223) or their variants such as $(Tl_{0.5}Pb_{0.5})Sr_2Ca_2Cu_3O_9$ (Tl(Pb)-1223) have special interest, for they exhibit stronger flux pinning at 77 K and a significantly higher magnetic irreversibility line than $Tl_2Ba_2Ca_1Cu_2O_8$ (Tl-2212), $Tl_2Ba_2Ca_2Cu_3O_{10}$ (Tl-2223), $Hg_1Ba_2Ca_2Cu_3O_{10}$ (Hg-1223), $Bi_2Sr_2Ca_1Cu_2O_y$ (Bi-2212) and $Bi_2Sr_2Ca_2Cu_3O_9$ (Bi-2223).[35, 36, 37] Figure 2 shows the comparison of irreversibility lines for some major HTS systems.[38, 39, 40, 41, 42] Utilization of these materials is restricted to magnetic fields and temperatures below these irreversibility lines. The irreversibility line for Tl-1223 approaches that of YBCO in the temperature range around liquid nitrogen, and is superior to the lines of the Bi-system and the Hg-system. Therefore, like YBCO, the Tl-1223 system also has big interest in power applications.

It is worth mentioning that the effect of extrinsic defects is also demonstrated by the

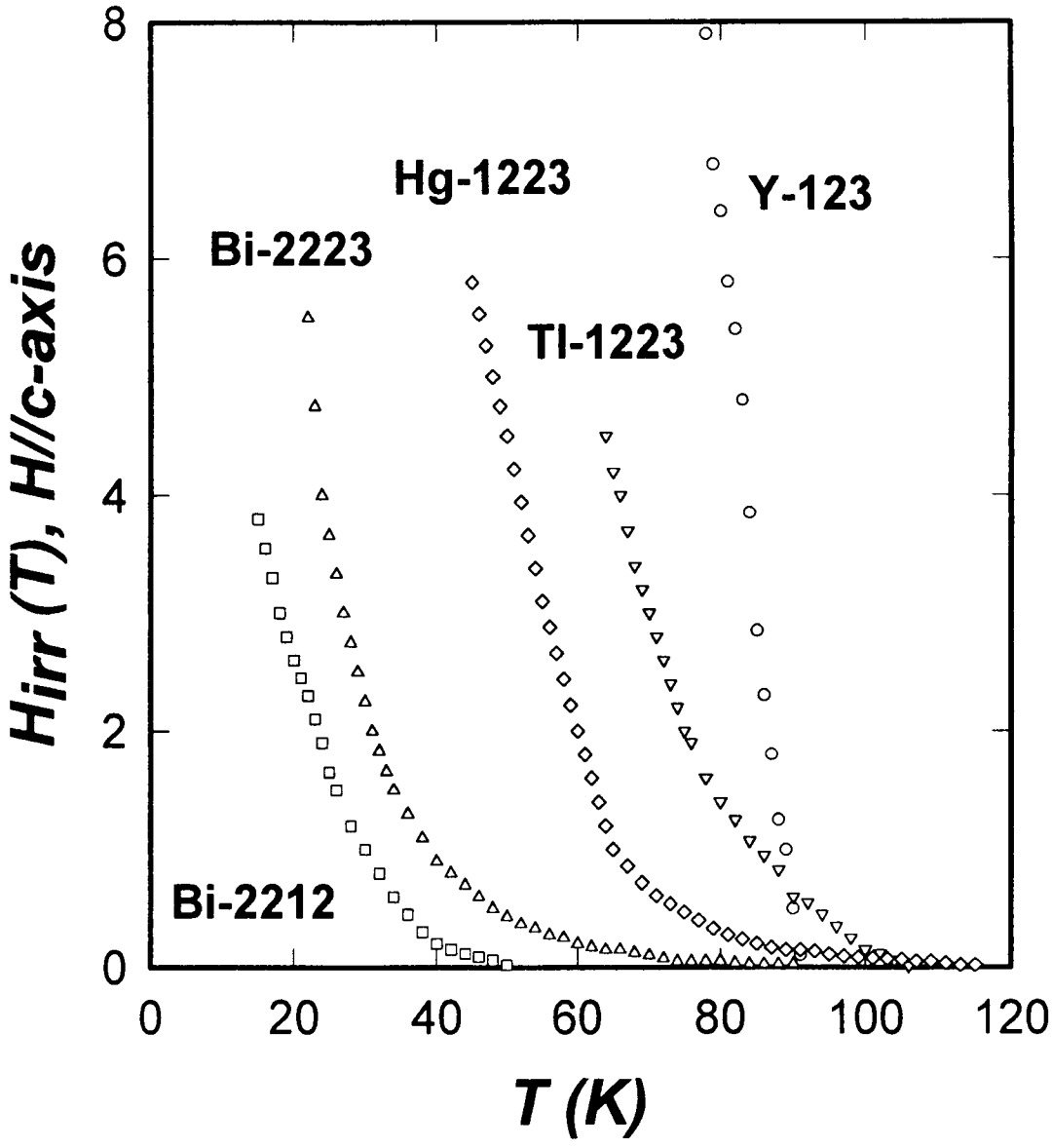


Figure 2 Comparison of irreversibility lines for major HTS systems. The magnetic field H is parallel to the *c*-axis of the HTS samples.

significant shift in the irreversibility line to higher temperature following heavy ion irradiation.[43]

2.1.2 Metallic substrates for Tl-1223 films

Since all the HTS are brittle ceramic oxides, it is hard to make flexible wires with the bulk Tl-1223 materials. To overcome the brittleness problem, a powder-in-tube (PIT) process has been developed for the Tl-system.[44, 45] However, unlike the success achieved in the Bi-system, uniaxial alignment has not been achieved from this method for Tl-1223. Here, we will investigate an alternative process to make flexible HTS Tl-1223 tape, i.e., to deposit the Tl-1223 film on some flexible metallic substrates. Silver is an appealing substrate since it provides a flexible, conductive backing, and offers the advantage that no additional buffer layers are required due to its chemical compatibility with oxide superconductors. Moreover, it has been shown that the addition of Ag in the film can reduce the processing temperature by about 35°C, and its presence is crucial for the formation of a liquid phase, thereby accelerating the growth kinetics of Tl-1223 phase.[46] A limited reaction between the high-T_c film and Ag substrate is not harmful to the superconducting properties.

DeLuca *et al.*[47] have made highly-textured Tl-1223 films on polycrystalline YSZ substrate by spray pyrolysis, which means that, unlike YBCO films, the growth of high-textured Tl superconducting films can be realized on polycrystalline substrates. This is another reason why we chose polycrystalline Ag instead of expensive single crystal Ag as a substrate. The disadvantage of Ag's low strength may be overcome by using hardened Ag alloys, such as Ag-Ca alloy, or using Ag as a buffer layer between the high-T_c film and a Ni-alloy.

2.1.3 Deposition methods for Tl-1223 thick films

Previously, high-quality Tl-1223 films have been grown by several techniques, such as spray pyrolysis,[48, 49] sputtering,[50] electron beam evaporation,[51] metal organic chemical vapor deposition ,[52] and laser ablation.[53, 54] Z. F. Ren *et al.*[54] reported the fabrication of 1-μm-thick epitaxial Tl-1223 films on single-crystalline $LaAlO_3$ substrates with T_c = 106-111 K and J_c = 2×10^6 A/cm^2 at 77 K by laser ablation. They used a Tl-containing target to epitaxially deposit the Tl-1223 films in-situ. The major advantage of this technique is that a film with a dense oxide precursor, biaxial orientation, and very high J_c can be obtained. The major disadvantage is the Tl contamination of the vacuum chamber and the difficulty of making it into a scalable process. DeLuca *et al.*[47] have reported the depositions of 3-μm-thick Tl-1223 films on polycrystalline YSZ substrates with T_c = 104-107 K and J_c of 1.1×10^5 A/cm^2 at 77 K by two-zone processing. This technique involves the deposition of Tl-free precursor films by spray pyrolysis, followed by annealing in the two-zone Tl furnace where the sample and Tl-source are physically separated, and independent control of the Tl_2O_3 source temperature is used to control the vapor pressure above the sample. The advantages of this process are that it restricts the Tl contamination inside the two-zone Tl furnace and uses non-vacuum film-making system, which can reduce the cost and be easy to scale up.

However, for deposited conductor applications, all the techniques mentioned above are unable to produce thick deposits (e.g., thicker than 10 μm) in reasonable processing times. Figure 3, from J. E. Tkaczyk,[55] shows a rough comparison of deposition techniques by examining the J_c values versus the superconducting layer thickness and indicates the future target for the deposition of Tl-1223 films, i.e., thick coating films of over 10 μm with

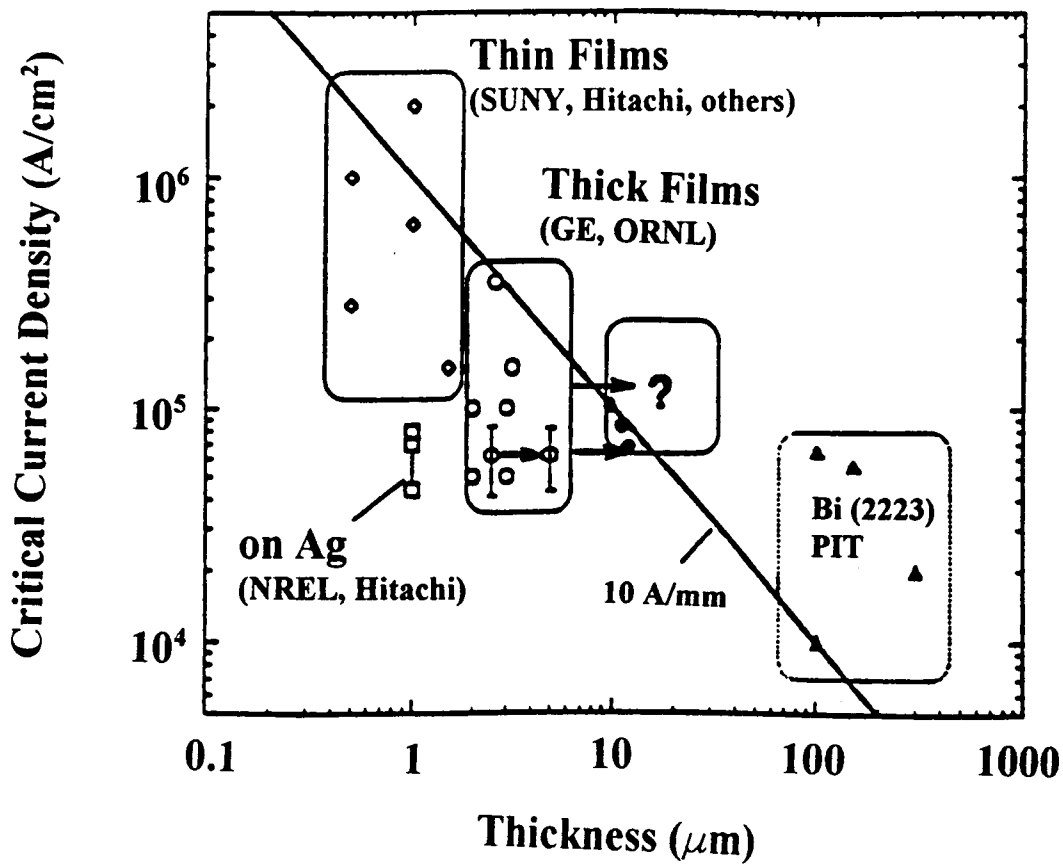


Figure 3 J_c values for different deposition techniques. The interesting area is the Tl-1223 thick film (>10 μm) with appropriate high J_c values.

moderate J_c values. As we know, the J_c values for the best polycrystalline films will not improve much above that already achieved (J_c value of about 10^5 A/cm^2) due to the random in-plane orientation of the Tl-1223 films on polycrystalline substrates. Therefore, progress toward an economical conductor will follow from the development of a deposition and processing technique to attain a layer thickness in the 10-50 μm range in order to increase the critical current I_c or J_e which is the engineering J_c.

To fabricate flexible high-J_c Tl-1223 thick films over 10μm thick, we have developed a new process, using a spin-coating technique, which can provide a simple, inexpensive, rapid means to deposit films with thickness above 10 μm over large areas. It can easily be developed into dip-coating techniques, which are scalable to continuous fabrication. The thick film process offers a potentially viable alternative to the popular powder-in-tube process for making long superconducting tapes.

2.2 Biaxially textured HTS films on metals

2.2.1 Weak link problems

Unlike conventional low-T_c superconductors where the grain boundaries act as pinning centers, grain boundaries in high-T_c superconductors are weak-links due to the extremely short coherence lengths in these materials. Dimos *et al.*[56, 57] have demonstrated the effect of the intrinsic anisotropy of the superconducting properties and the presence of structural disorder at grain boundaries on J_c by studying the grain boundaries of YBCO epitaxial films grown on bi-crystals of $SrTiO_3$. They studied three different grain boundary geometries: [001] tilt boundary, [100] tilt boundary, and [100] twist boundary. As shown in

the Figure 4, as the misorientation angle increases from 0° to 10°, the J_c values decrease somewhat. However, when the misorientation angle is greater than 10°, the J_c values of all three types of boundaries decrease rapidly, which implies a weak-link behavior resulting from the intrinsic structural disorder at the boundary. The Dimos-type experiment has also been extended to [001] tilt bicrystals in $Tl_2Ba_2Ca_1Cu_2O_8$,[58] $Tl_2Ba_2Ca_2Cu_3O_x$,[59] and $Tl_1Ba_2Ca_2Cu_3O_x$.[60] For each case, like YBCO, the grain boundary J_c value is strongly dependent on the grain boundary misorientation angle. A. Goyal *et al.* [61, 62] also have systematically studied the weak-link behaviors in the Tl-1223 films on YSZ polycrystalline substrates. All the grains colonies are uniaxially aligned with respect to their *c*-axis. Local texture was determined from XRD ϕ scans with different effective x-ray beam sizes. The intensity distribution obtained using the largest beam consists of several peaks superimposed on an average intensity, suggesting that basal plane orientations are largely random. A very different intensity distribution is obtained when a smaller beam is used. Such peaks in the ϕ scan indicate the presence of locally aligned regions or "colonies" of bi-axially aligned grains. The results show excellent correlation between regions of high-J_c and high in-plane texture. By microstructural grain-orientation mapping through electron backscattering patterns (EBSP), they have revealed the presence of local in-plane grain alignment extending over grain colonies of dimensions from 100 μm to 1 mm. Current transport occurs through a network of percolative paths across adjacent colony boundaries. These paths select the low-angle grain boundaries of the overlapping grain orientation distributions of neighboring colonies. From the discussion above, we can see that in order to increase the J_c value, higher populations of small angle boundaries which result in enhanced percolative options are

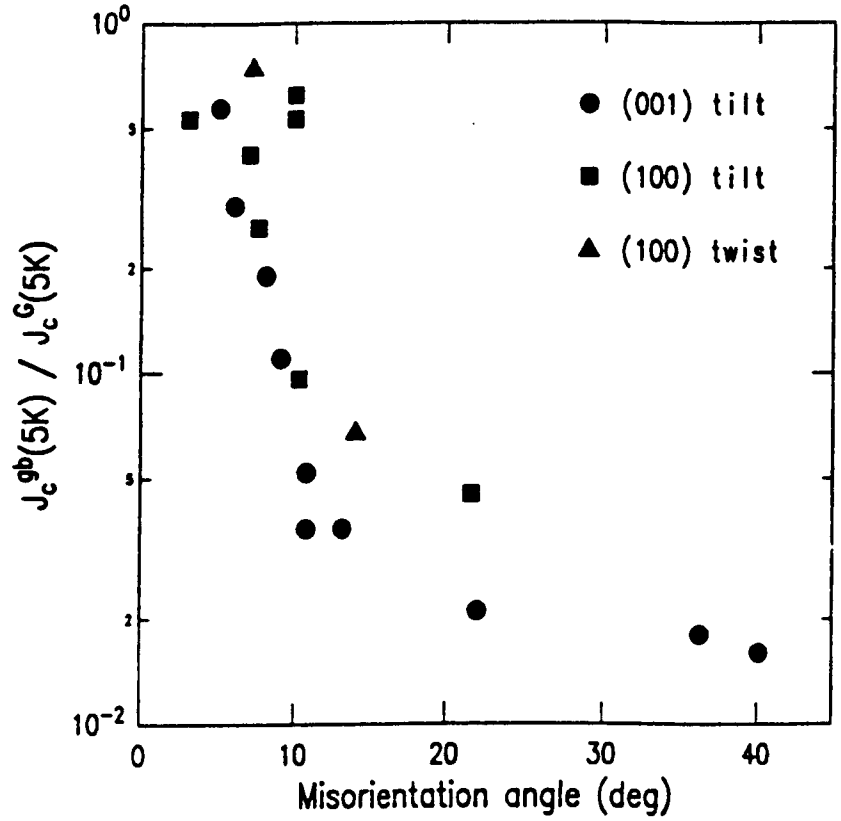


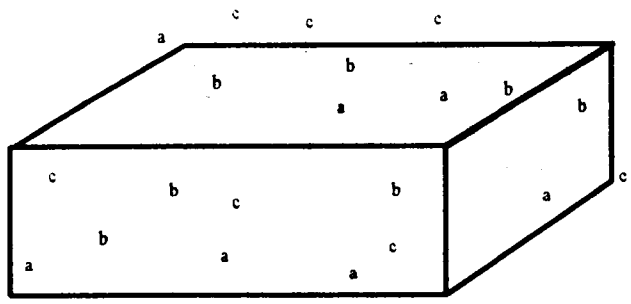
Figure 4 The J_c values across a grain boundary decrease rapidly as the misorientation angle is over 10° for three different grain boundary geometries: [001] tilt boundary, [100] tilt boundary, and [100] twist boundary.

required. Figure 5 roughly describes the relationship between the J_c value and the orientations in the HTS. If the HTS is polycrystalline with random orientation, such as bulk ceramic HTS materials, the J_c value is about 10^3 A/cm^2 at 77 K. As the HTS has *c*-axis orientation but random in-plane orientation, such as the Tl-1223 films on polycrystalline YSZ substrate, the J_c can be 10^4-10^5 A/cm^2 at 77 K. As the HTS materials have not only *c*-axis orientation but also good in-plane alignment (i.e., biaxial orientations), such as epitaxially single crystal YBCO films, the J_c value can be above 10^6 A/cm^2 at 77 K. Hence, making HTS materials with high degree of biaxial alignment over the entire length of the conductors may be the key to overcome the weak link problems thus obtaining a high transport J_c value in the flexible HTS wires.

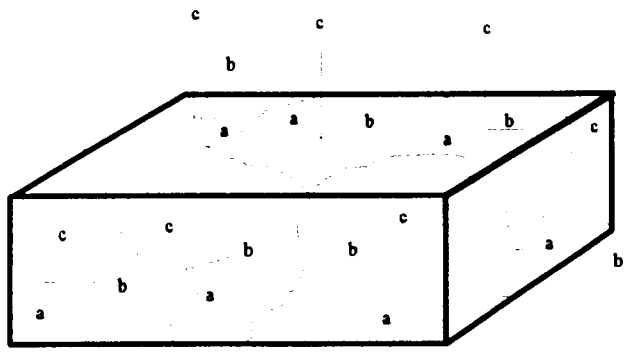
2.2.2 Previous efforts on biaxially textured HTS films on metals

HTS films with biaxially orientation have been grown on single crystal oxide substrates.[63, 64] But, it is not feasible to produce long lengths of these substrates with good flexibility. By powder-in-tube (PIT) technique,[65] flexible Bi-2223 tapes with high J_c value and a modest *c*-axis texture have been fabricated. However, the Bi-2223 phases in these tapes don't have in-plane orientation and high angle boundaries are expected. The J_c value decreases rapidly in the magnetic field due not only to the weak link problem, but also to the weak flux pinning due to the large anisotropy.

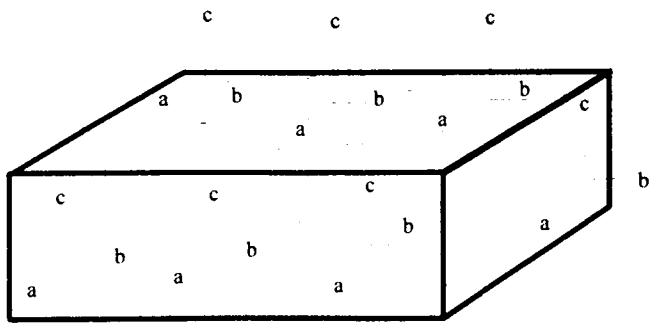
Ion beam-assisted deposition (IBAD) has been developed by X. D. Wu *et al.*,[66, 67] Iijima *et al.*,[68, 69] and Reade at al.,[70] which can achieve biaxially textured oxide buffer layers



HTS with random in-plane and out-of-plane orientations: $J_c \sim 10^3$ A/cm^2 at 77 K



HTS with c-axis texture but random in-plane orientation: $J_c \sim 10^4$ - 10^5 A/cm^2 at 77 K



HTS with both in-plane and out-of-plane orientations: $J_c \geq 10^6$ A/cm^2 at 77 K

Figure 5 Schematic relationship between the J_c value and the structural orientation in a HTS.

on flexible polycrystalline metal substrates for the subsequent epitaxial growth of YBCO. The J_c values are significantly increased in the range of 10^5 to 10^6 A/cm^2 at 77 K. However, IBAD techniques have limitations in the commercial production because of the requirements of complicated and expensive equipments, the low deposition rates for biaxially textured thick YSZ buffer layer, and the difficulties in consistently producing in-plane crystallographic alignment of less than 10°.

K. Hasegawa, *et al.* in Sumitomo Electric Industries Ltd.[71, 72] also developed a novel method of depositing in-plane aligned YBCO films on YSZ buffered Hastelloy polycrystalline substrates. The in-plane alignment of a YSZ buffer layer is obtained by inclining the substrate with respect to the direction of the plasma plume in PLD. The J_c value for the films is 1.5 × 10^5 A/cm^2 (77 K, 0 T) over the whole length of 1 meter. The best J_c value achieved was 4.3 × 10^5 A/cm^2 but the FWHM value of YBCO (103) poles was 12.8°. However, it may be difficult to further improve the biaxial orientations of the YBCO films by this technique.

2.2.3 New approach: RABiTS technique

Recently, a team of scientists at Oak Ridge National Laboratory have demonstrated a new technique, RABiTS (Rolling-Assisted Biaxially Textured Substrate),[73, 74, 75,76, 77] by which biaxially textured high-J_c HTS can be obtained for over long lengths. The principle for RABiTS, as shown in Figure 6, is simple. The RABiTS composite consists of three parts. The substrate is sharply biaxially-textured metal which can be produced over long lengths by thermo-mechanical processing techniques. Biaxially textured buffer layers are deposited on the textured metal substrates, followed by the epitaxial growth of HTS films on top of the

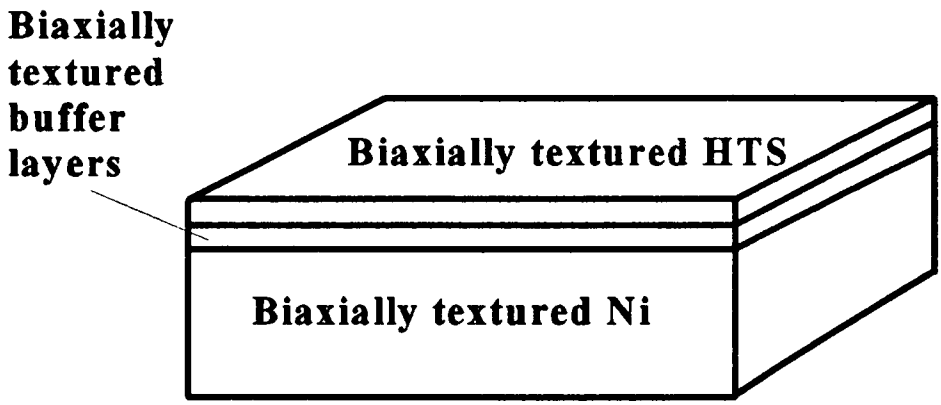


Figure 6 Components of the RABiTS structure: sharply biaxially-textured flexible metal substrate, biaxially textured buffer layers, and epitaxial HTS film with high J_c value.

buffer layers. A path envisioned path toward this desired result is through the development of biaxially-aligned, continuous metallic tapes that can act as epitaxial templates for biaxially aligned HTS deposits. Thus, long flexible HTS tapes with high J_c value are expected to be made using the RABiTS concept. Different from the Sumitomo technique mentioned above, the RABiTS method can get much better biaxial orientations in the HTS films. The RABiTS technique can also overcome the limitations that IBAD techniques have faced, such as the relatively low deposition rates associated with the IBAD buffer layers as well as difficulties in consistently producing in-plane crystallographic alignment of less than 10°. Unlike IBAD, film depositions by RABiTS are not restricted in an expensive vacuum system.

Besides the applications of HTS, many other electronic applications involving ferroelectric, ferromagnetic, and semiconductor devices also rely on the formation of biaxially textured films. Traditionally, most of these devices are formed using epitaxial growth on single crystal semiconductor or metal oxide substrates. Right now, the general concept of RABiTS may open the way for biaxially textured films to be economically grown on textured metal substrates which can be fabricated over long lengths or large areas.

2.2.4 Requirements for metallic substrates

The criteria used to select the candidate metallic substrates are source material and production costs, melting temperature T_m, mechanical flexibility and strength, chemical compatibility, and biaxial crystalline orientation and epitaxial relationships with HTS. Ni is a candidate metallic substrate material because it is inexpensive, possesses good mechanical properties, and has a high melting temperature (1455°C). As a high purity fcc metal, it can

be biaxially cube textured by thermo-mechanical processing. The disadvantage of the Ni tape is that Ni is ferro-magnetic, which may affect the energy losses in some applications. Some nonmagnetic metallic substrates are being studied.

2.2.5 Requirements for buffer layers

Since direct epitaxy of HTS materials on Ni substrates is exacerbated by chemical reaction and oxidation of Ni at high processing temperatures, and by the large crystalline lattice mismatch with all HTS materials, a buffer layer must be employed. The buffer layers play an important role in the RABiTS technique because they not only protect the HTS film from Ni contamination, but also transfer the biaxially oriented structure from Ni to the top HTS film. The candidate buffer layers should have both structural and chemical compatibility with both the underlying Ni and the final HTS layer. Therefore, the buffer layers should have high melting point and good lattice match with both Ni and YBCO. In addition, the thermal expansion coefficient for buffer layers should be similar with both Ni and YBCO. Table 4 shows the lattice constants, thermal expansion coefficient, melting point, and the lattice mismatch with Ni and YBCO for some candidate buffer layers. For example, CeO_2 is a desired buffer layer because of the high melting temperature (2600°C), low lattice mismatch with YBCO (~0.26%), and similar thermal expansion coefficient with YBCO. The final criterion is feasibility of growth of the biaxially textured buffer layers on the Ni substrate and the growth of epitaxial YBCO films on the buffer layers without Ni contamination.

Table 4. The lattice constants, thermal expansion coefficient, melting point, and the lattice mismatches with Ni and YBCO for some candidate buffer layers. The lattice mismatches are calculated according to the formulas in appendix 3.

Materials	**Structure**	**Lattice constants (Å)**	**Thermal expansion β (× 10^{-6} /°C)**	**melting point (°C)**	**Mis-match with Ni**	**Mis-match with YBCO**
YBCO	Ortho.	a = 3.836 b = 3.883 c = 11.68	$\alpha_a = 14$ $\alpha_b = 9$ $\alpha_c = 19$	-	8.86	0
$SrTiO_3$	Cubic	3.905	10.4	2353	10.8	0.56
$LaAlO_3$	Rhomb.	3.789	11	2453	7.53	1.22
MgO	Cubic	4.2114	10.5	2852	15.49	8.46
YSZ	Cubic	5.139	8.8	2715	3.12	5.27
CeO_2	Cubic	5.411	8.9	2600	8.58	0.26
$YAlO_3$	Hexagon.	a = 3.678 c = 10.52	5-10	-	4.38	4.12
Ni	Cubic	3.5238	13	1455	0	8.14
Pd	Cubic	3.8898	-	1554	10.39	0.17
Pt	Cubic	3.9231	9	1772	11.33	0.10
Ag	Cubic	4.0862	19	962	15.96	5.23
Cu	Cubic	3.615	16.6	1082	2.59	5.76
Fe	Cubic	2.8664	12	1538	18.66	4.39

Materials	Structure	Lattice constants (Å)	Thermal expansion β (× 10^{-6} /°C)	melting point (°C)	Mis-match with Ni	Mis-match with YBCO
Ta	Cubic	3.3058	6.5	2996	6.19	13.8
Si	Cubic	5.4301	3	1410	8.96	0.1
NaCl	Cubic	5.6402	-	801	13.18	2.71
$KTaO_3$	Cubic	3.989	6.8	>1630	13.2	2.73
$SrRuO_3$	Cubic	3.94	-	-	11.8	1.47
Sr_2RuO_4	Tetra.	3.87	-	-	9.82	0.33
$LaNiO_3$	Rhomb.	3.861	8.2	>1120	9.57	0.65
$CaTiO_3$	Ortho.	5.4405	-	-	9.17	0.29
$Sr(Al_{1/2}Ta_{1/2})O_3$	Cubic	3.8952	9.7	1900	10.5	0.31
$Sr(Al_{1/2}Nb_{1/2})O_3$	Cubic	3.8995	8.8	1790	10.7	0.42
$NdGaO_3$	Ortho.	5.431	8	1873	8.98	0.11
$BaZrO_3$	Cubic	4.193	-	2500	18.99	7.98
NiO	Cubic	4.1769	-	1984	18.53	7.67

3. EXPERIMENTAL

3.1 Spin-coating method for Tl-1223 thick films on Ag

3.1.1 Precursor film depositions

Precursor films were deposited by a spin coating technique on smooth polycrystalline Ag substrates of dimensions of $12\times8\times0.25$ mm^3. The Tl-free precursor slurry used for the spin coating technique consisted of fine powder with the nominal composition $Ca_2Ba_2Cu_3Ag_{0.37}O_y$, suspended in the commercial organic binder Butvar B-76, with solvents of 4-methyl-2-pentanone and xylene. Several kinds of precursor powders were used, one of which was aerosol flow reacted powder having uniform composition and fine particle size less than 1 μm.[78] This slurry was dispersed ultrasonically for 1 hour immediately before the spin coating deposition. The substrate was placed on the photo-resist spinner and a few drops of the slurry were deposited onto the surface. The substrate was spun in the range of 1-4 k RPM. The coated substrates were heated at 600°C for 6 hours in flowing air to burn out the organic material and cooled down slowly. Another heat treatment at 850°C for 1 min in flowing oxygen was performed before thallination. The thallium-free precursor on the Ag substrate was pressed or rolled to increase the density of the precursor deposit through compression. The pressure applied to the powder precursor was above 1000 kg/cm^2. Pressure about 5000 kg/cm^2 or higher is preferred.

3.1.2 Thallination

As shown in Figure 7, the densified precursor films were processed in the two-zone thallium furnace. The partial pressure of Tl vapor in the furnace was determined by the temperature of the Tl source in a low temperature zone (or Tl source zone) while the temperature of the sample was independently controlled in the high temperature zone (or sample zone). The precursor samples were mounted on the Ni tape which could move from side to side passing through the slot of one end of a big ceramic tube. An oxygen flow of approximately 20 sccm (standard cubic centimeters per minute) was blown into the small ceramic tube to carry the Tl oxide vapor to the high temperature zone. There, the Tl vapor could react with the $Ba_2Ca_2Cu_3O_y$ precursor films to form Tl-1223 phase. The pull-through apparatus was specially designed for the fabrication of flexible high-J_c Tl-1223 tapes with long length. The reaction time of the precursor film at high temperature was controlled by the moving speed of the Ni tape. The sample and source zones were respectively heated from 400°C to about 860°C and from 400°C to 600°C, in 40 min. Subsequently, the Tl source was ramped from 600°C to 690°C in 24 min; then from 690°C to about 740°C in 10 min. The Tl source was soaked at about 740°C for 1-4 hours and then furnace cooled.

3.1.3 Property measurements of the Tl-1223 films

The samples were patterned with a bridge structure 4 mm long and 2 mm wide. After being patterned, they were annealed in flowing oxygen at 600°C for 10 hours. The thickness was determined by a surface profilometer. The film thickness can be controlled in the range of 10 to 50 μm by varying the rotary speed of the spinner and the viscosity of the slurry. The

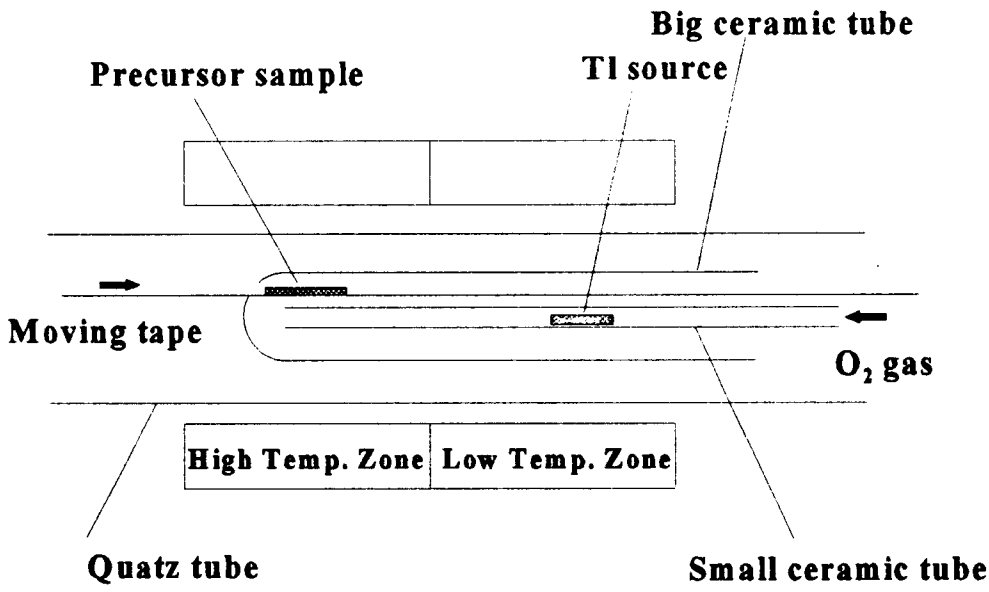


Figure 7 Diagram illustrating the essential features of the two-zone Tl-reaction furnace designed for the fabrication of long flexible high J_c Tl-1223 tapes.

amount of Tl content X in $Tl_xBa_2Ca_2Cu_3O_{7.5+1.5x}$ thick films were measured by the weight gain before and after Tl-treatment on the assumption that all the precursor material has been reacted with Tl uniformly. The orientations and morphology of the deposited films were characterized using x-ray θ-2θ scans, ω-scans, ϕ-scans, and a JEOL JSM-840 for SEM. Silver pad electrodes were attached with silver-paint. To enlarge the voltage signal, zero resistance transition temperature $T_{c,zero}$ was measured by using a current of 0.5 A. Resistance and transport J_c values were measured by using the standard four point method over 4 mm voltage gauge length. A criterion of $1\mu V/cm$ was used for the determinations of J_c. For the Tl-1223/Ag samples, the J_c values reflect net current densities carried only by the superconductor.

3.2 RABiTS technique

3.2.1 Preparation of biaxially textured Ni substrates

Biaxially textured smooth Ni base-metal substrates with thickness about 125 μm were formed by the progressive rolling deformation of polycrystalline, randomly oriented high purity nickel (99.99%) bars at room temperature (RT) to a total deformation greater than 90%. By controlling the surface condition of the work rolls, it was possible to obtain substrates with surfaces as smooth as those obtained by mechanical and chemical polishing. Atomic force microscopy (AFM) scanning of an as-rolled substrate indicated an rms (root-mean-square) roughness of ~ 10nm. Subsequently, to form a sharp {100}<100> cube texture, a primary recrystallization anneal was carried out in a vacuum or in hydrogen gas mixture at

a temperature in the range of about 200°C to 1200°C, preferably in the range of about 600°C to 900°C, for 1-4 hours. During the anneal, possible NiO and various impurities such as sulfur and carbon can be removed from the Ni substrate surfaces. The Ni substrate cleaning with detergents, organic solvents, and/or etchants is optional. Reverse sputtering was sometimes employed to further clean the Ni surface. This yields smooth, sharply biaxially textured surfaces with typical in-plane and out-of-plane alignments of ~7° FWHM (i.e., Full Width at Half Maximum).

3.2.2 Depositions of buffer layers on Ni by sputtering

Sputtering is a coating process which involves the vapor transport of almost any materials from a target to a substrate of almost any other material. The ejection of the source material is accomplished by the bombardment of the surface of the target with gas ions accelerated by a high voltage. Particles of an atomic dimension from the target are ejected as a result of momentum transfer between incident ions and the target. The target-ejected particles traverse the vacuum chamber and are subsequently deposited on a substrate as a thin film. There are some widely recognized advantages in the sputtering technique: 1. Improved adhesion: the kinetic energy of sputtered atoms or molecules are orders of magnitude greater than that of other evaporative deposition processes. 2. Improved stroichiometry: the ease of depositing compounds and maintaining composition. 3. Improved coverage of steps: because sputtered atoms have high kinetic energy, and in practical systems arrive at various angles of incidence, the films produced more easily cover step geometries which must be included in many substrates. 4. Flexibility: the nature of the process lends itself to adaption for complex

research application as well as high volume production uses.

Film depositions described herein were conducted in a dual-target magnetron sputtering system, employing either d.c. or r.f. power supplies. The target diameter, the target-to-substrate distance and the base pressure were respectively 9.5 cm, 7.5 cm and 1×10^{-7} Torr . The target was presputtered for about 10 min prior to film deposition. The substrates were mounted centrally above the target, in an on-axis geometry. The intermediate metal buffer layer of Pd was first deposited on the Ni substrates in an Ar pressure of 6 mTorr at a temperature between 25 and 550°C and the thickness of the Pd film was between 50 and 200 nm. Subsequently, a variety of epitaxial metallic and/or ceramic buffer layers were deposited on the Pd buffered Ni substrates. Ag films were deposited on the Pd-coated Ni substrates using the second target in the chamber with substrate temperature of 25-350°C, deposition rate of 0.1-5 nm/s, and thickness of 0.5-50 μm. Using r.f. sputtering, the CeO_2 films were grown on the Pd-buffered Ni substrates at a temperature between 25-500°C in 6 mTorr of Ar/O_2 ($10\%O_2$) to a thickness between 20-500 nm.

In a different approach, CeO_2 films were deposited directly on Ni, using a two-step process whereby an initial 10-30 nm thick layer was first deposited by r.f. sputtering in forming gas, followed by deposition in a $90\%Ar/10\%O_2$ ambient.

The $LaNiO_3$ film deposition was carried out at a temperature between 100°C and 700°C by r.f. magnetron sputtering. The $LaNiO_3$ target was made by lightly packing $LaNiO_3$ powder into a copper tray. The film deposition chamber preferably has a background base pressure of less than 10^{-6} Torr. The forming gas ($4\%H_2$ + 96%Ar) or pure Ar gas was used

as a sputtering gas in the pressure of 2×10^{-4} to 2×10^{-1} Torr. The deposition rate was between 0.1-10Å/sec. The total thickness of the $LaNiO_3$ film is at least 500Å.

The YSZ films can then be deposited on CeO_2/Pd/Ni, CeO_2/Ni or $LaNiO_3$/Ni substrates at 780°C under either forming gas or Ar/10%O_2 ambient.

3.2.3 Depositions of YBCO films on buffered Ni substrates

By pulsed laser deposition (PLD) using a KrF excimer laser, thick (>0.5 μm) YBCO superconductor films were then deposited on the buffered Ni substrates typically at temperature of 740°C - 780°C in an oxygen pressure of 185 mTorr. After deposition, the films were cooled at 10°C/min, with the oxygen pressure increased to 700 Torr at 400°C.

3.2.4 Property measurements of the films

The phase structure and out-of-plane mosaic distribution were measured by x-ray θ-2θ scans and ω-scans, while the in-plane orientation of the films and substrates was determined by x-ray ϕ-scans. Measurements were made by using Cu Kα x-rays and Huber four-circle diffractometer. The morphology of the deposited films was characterized by using a JEOL JSM-840 SEM. The T_c and J_c values were measured by four-terminal electrical transport standard methods. Prior to measurement, the films were patterned into a bridge about 175 μm wide and 3 mm long by photolithography. The samples with voltage and current Ag contacts were annealed at 550°C in O_2 for ½ hour and cooled slowly. The film thickness was determined by a Dektak profile after patterning. The measurements of J_c (H) were made in magnetic fields aligned both perpendicular and parallel to the film plane.

RESULTS AND DISCUSSION

4.1 Tl-1223 films on Ag by spin-coating

4.1.1 Effects of T_{source}, T_{sample}, and the reaction time

Figures 8 and 9 show the effects of Tl source temperature T_{source} and reaction time on the Tl content X in the spin-coated $Tl_xBa_2Ca_2Cu_3O_{7.5+1.5x}$ thick films on Ag. From Fig. 8, it is found that the X value is directly proportional to source temperature T_{source}, which may be explained by the consideration of kinetic and thermodynamic factors.[79] In the Tl source zone, there is a reaction:

$$Tl_2O_3(solid) \rightleftharpoons Tl_2O(gas) + O_2(gas)$$

The equilibrium constant K_1 of the equation can be calculated by the formula

$$\log_{10}K_1(atm^2) = (17.65 \pm 0.2) - (20.62 \pm 0.19) \times 10^3 / T$$

which means the equilibrium constant K_1 increases as temperature goes up. The constant K_1 is defined by

$$K_1(atm^2) = P_{Tl2O} P_{O2}$$

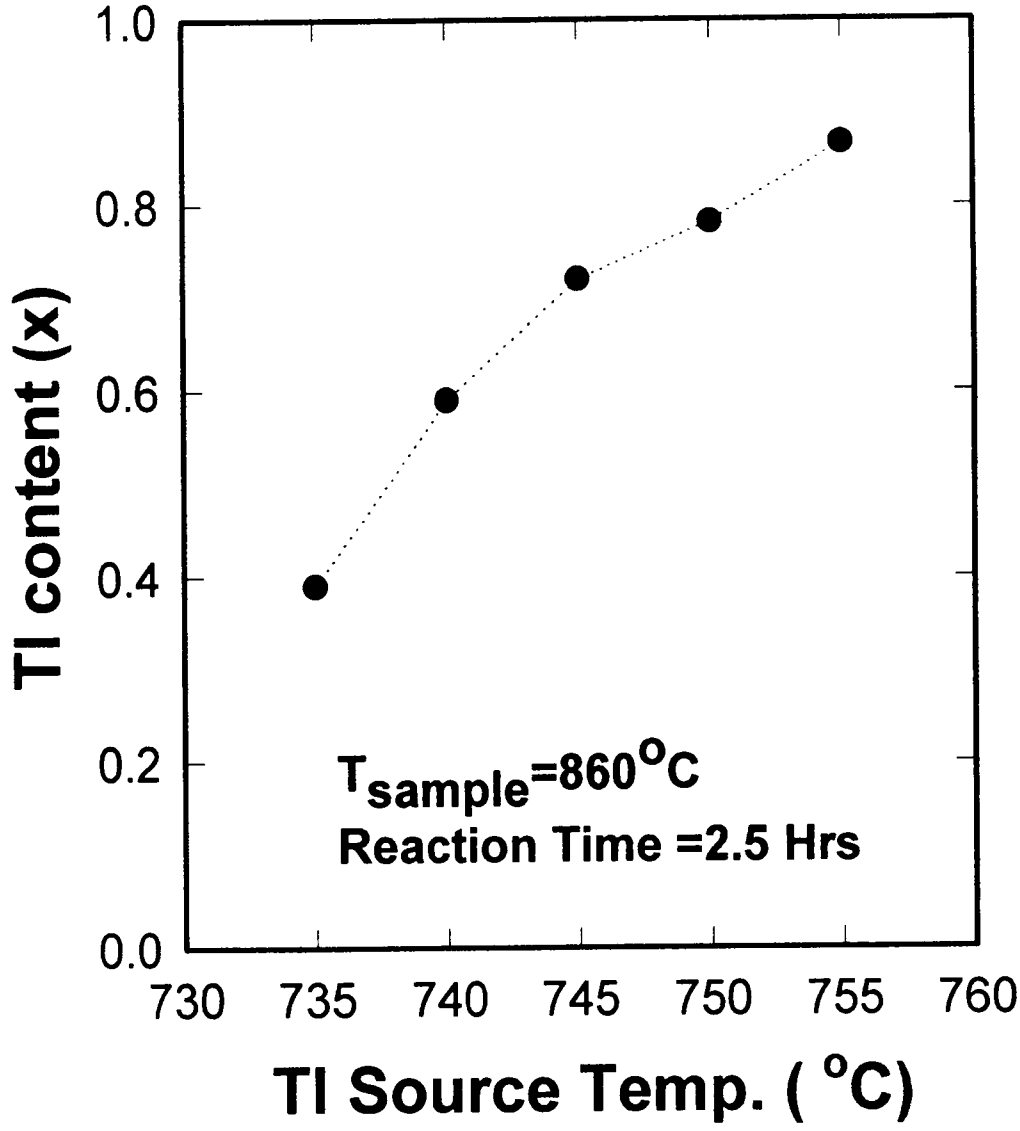


Figure 8 Tl source temperature T_{source} dependence of Tl content X in $Tl_xBa_2Ca_2Cu_3O_{7.5+1.5x}$ spin-coated thick film on Ag substrate at T_{sample} of 860°C and 2.5 hours reaction time.

where P_{Tl2O} and P_{O2} indicate the partial vapor pressures of Tl_2O and O_2, respectively. The constant K_1 is numerically equivalent to P_{Tl2O} as the oxygen pressure P_{O2} is kept at 1 atmosphere. Therefore, the higher the T_{source}, the higher the P_{Tl2O} will be. The reaction in the sample zone can be expressed in the following equation

$$2(Tl_1Ba_2Ca_2Cu_3O_9) = Tl_2O(gas) + O_2(gas) + 2(Ba_2Ca_2Cu_3O_{7.5})$$

It is easy to see that the increased Tl vapor pressure P_{Tl2O} and therefore increases the formation of Tl-1223 phase. The Tl content X also increases directly with reaction time, as shown in Figure 9, which can be qualitatively explained by diffusive Tl mass-transport from the surface into the thick film, until the Tl content X saturates to a stable value. From Figures 8 and 9, it is found that by controlling the T_{source} and reaction time, we can obtain the desired Tl content X value of the thick films. From experience, the best J_c values were achieved at lower X values in the range of 0.5 to 0.7 instead of 1. Higher X value may result in the appearance of Tl-2223 phase. In fact, the deduced value of X from weight gain is probably an lower bound, because of some weight loss from the Ag additions and Ag substrate, due to the substantial vapor pressure of Ag at the processing temperature ~860°C. In contrast with the condition for spray pyrolyzed 3 μm thick film, the optimum T_{source} and reaction time for the spin-coated thick film are 740°C and 2.5 hours rather than 730°C and 0.5 hours for the spray pyrolyzed films, partially because the spin-coated films are thicker than the spray pyrolyzed films.

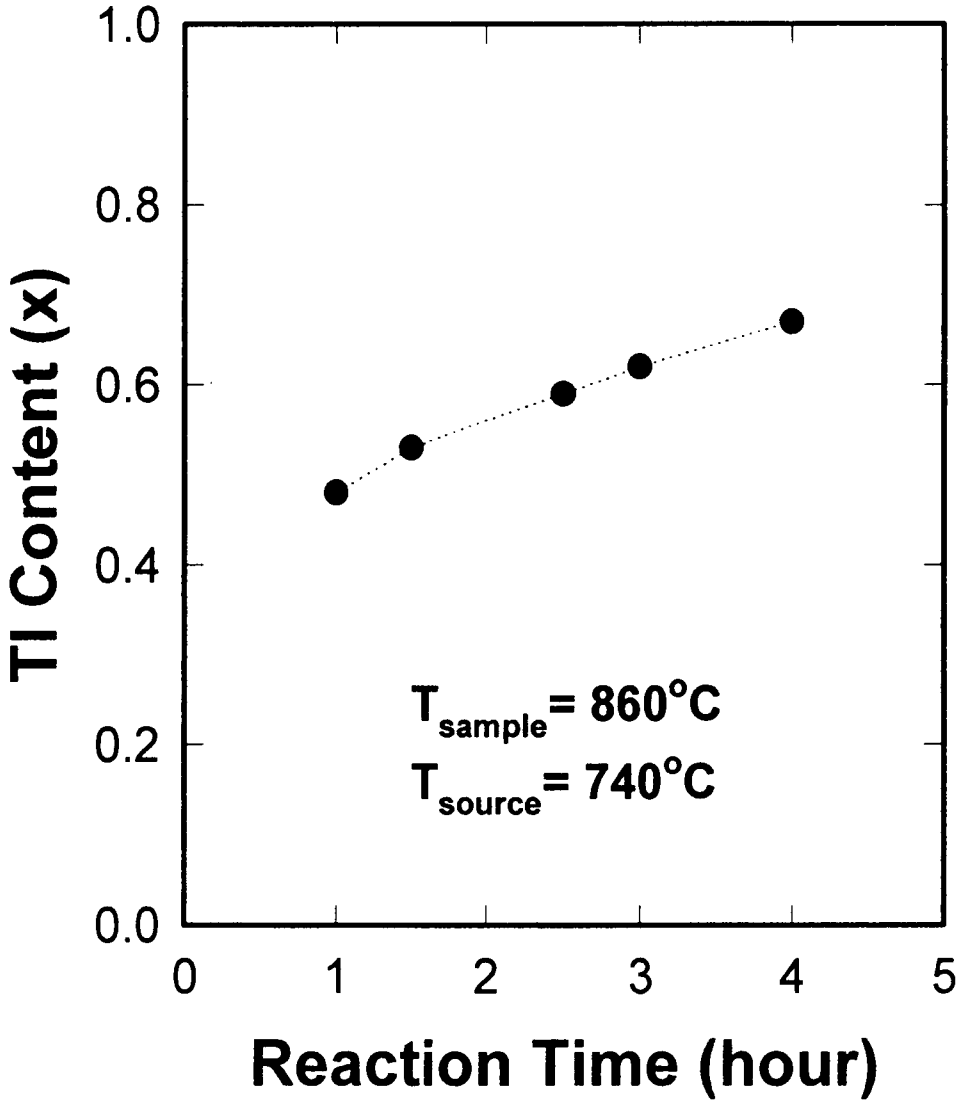


Figure 9 Reaction time dependence of Tl content X in $Tl_xBa_2Ca_2Cu_3O_{7.5+1.5x}$ spin-coated films on Ag substrate at T_{sample} of 860°C and T_{source} of 740°C.

In Figure 10, it is found that the Tl content X value is not very sensitive to the sample temperature T_{sample}. The X value deviated little from the value 0.6 over a wide temperature range from 850 to 870°C. However, T_{sample} crucially affects the phase morphology, and consequently strongly influences the superconducting transport properties. Both low and high T_{sample} may result in inferior samples. When T_{sample} is too high at 866°C, the films "over react" and form large grains with both *c*-axis and *a*-axis orientations and with high-angle grain boundaries, as shown in Fig. 11(a). X-ray diffraction also showed poor *c*-axis alignment for the sample. The J_c value for the sample was only about 5.5×10^3 A/cm^2 at 77 K. But low T_{sample} may lead to under-reaction, as shown in Fig. 11(b), the SEM microstructure from a sample Tl-treated at 851°C. It is observed that there are many unreacted precursor particles around the plate-like grains. The J_c value for the sample was only about 1×10^4 A/cm^2 at 77 K. SEM micrographs of the spin-coated Tl-1223 films which were treated at 860°C are shown in Figures 12 (a) and (b). It is revealed that the microstructure consists of a desired overlapping, plate-like, dense, layered structure (Fig. 12 (a)) and a small amount of fan-like structure (Fig. 12 (b)). The plate-like layered structure is *c*-axis oriented grains which are grown parallel to the substrate surface, while the fan-like structure is *a*-axis oriented grains which are grown perpendicular to the substrate surface. The fan-like structure should be avoided if possible, since it degrades the J_c value. Figure 13 shows the effect of T_{sample} on J_c for the thick films. We see that the samples with higher J_c values of 4.7×10^4 A/cm^2 at 77 K were achieved around 857°C.

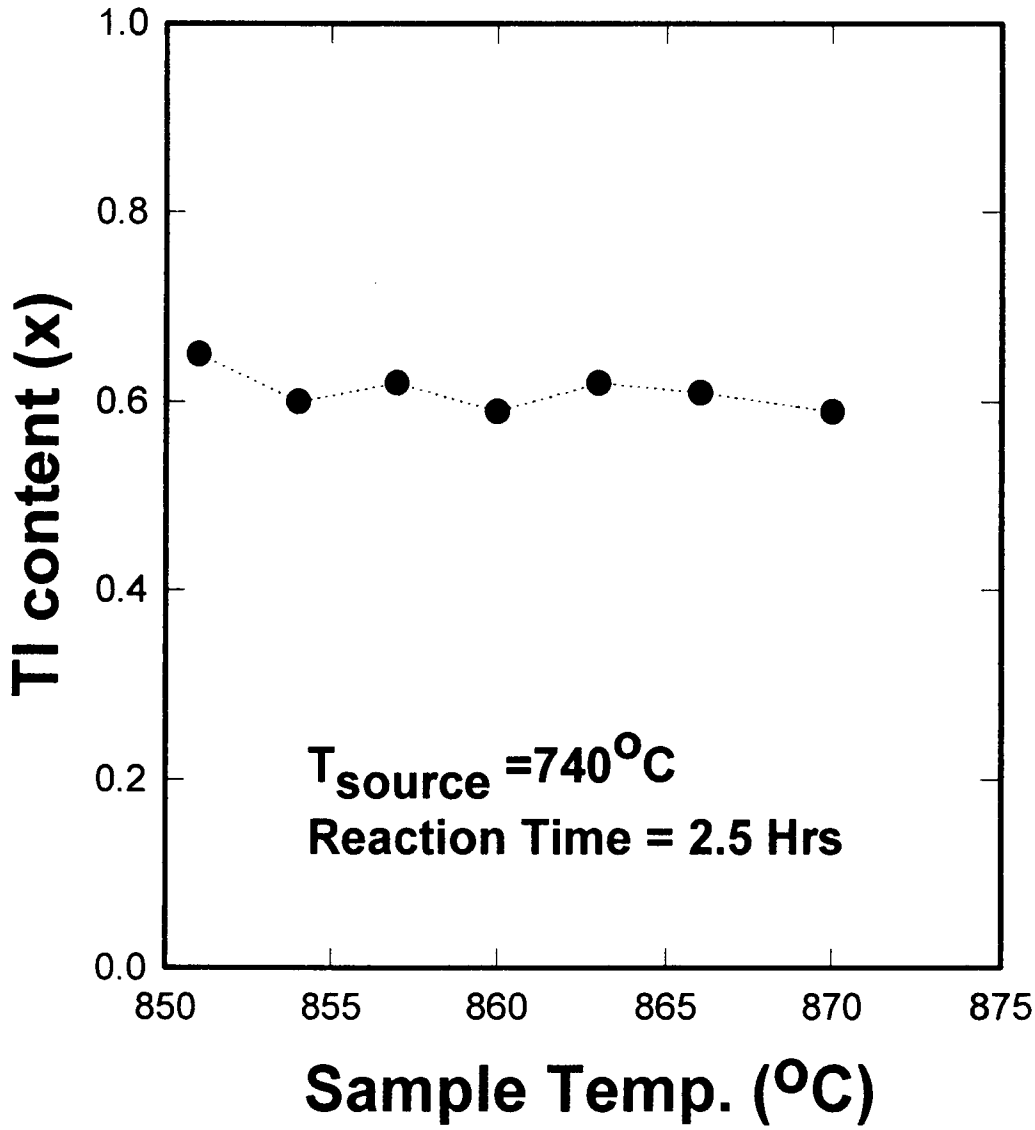
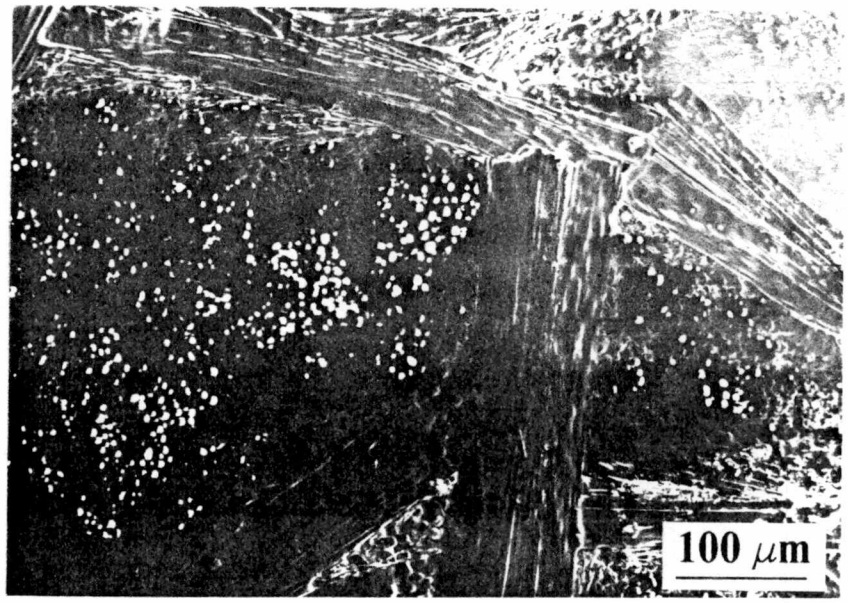


Figure 10 Sample temperature T_{sample} dependence on Tl content X in $Tl_xBa_2Ca_2Cu_3O_{7.5+1.5x}$ spin-coated thick film on Ag substrate, at T_{source} of 740°C and 2.5 hour reaction time.

(a)



(b)

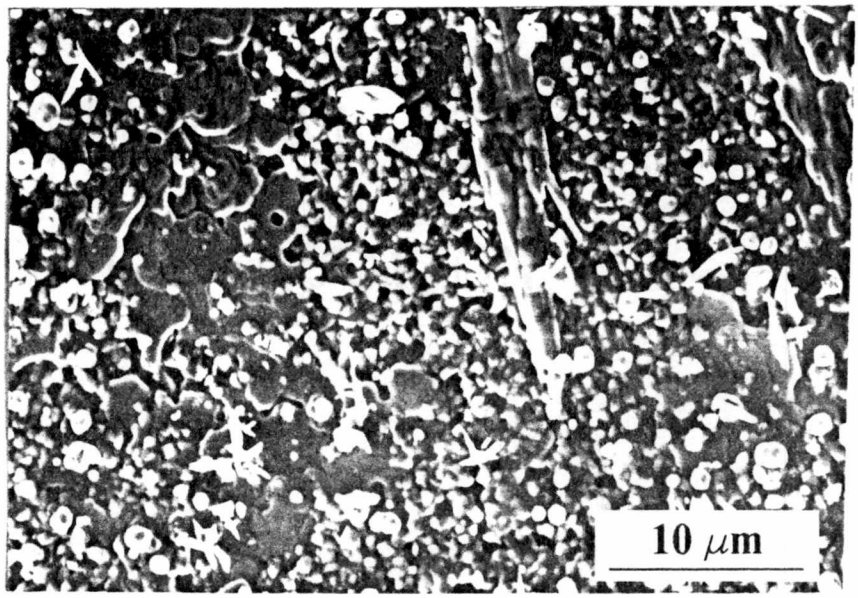


Figure 11 (a). SEM micrograph showing the surface morphology of Tl-1223 thick film on Ag, after treatment at T_{sample} of 866°C; (b). SEM micrograph showing the surface morphology of Tl-1223 thick film on Ag, after treatment at T_{sample} of 851°C.

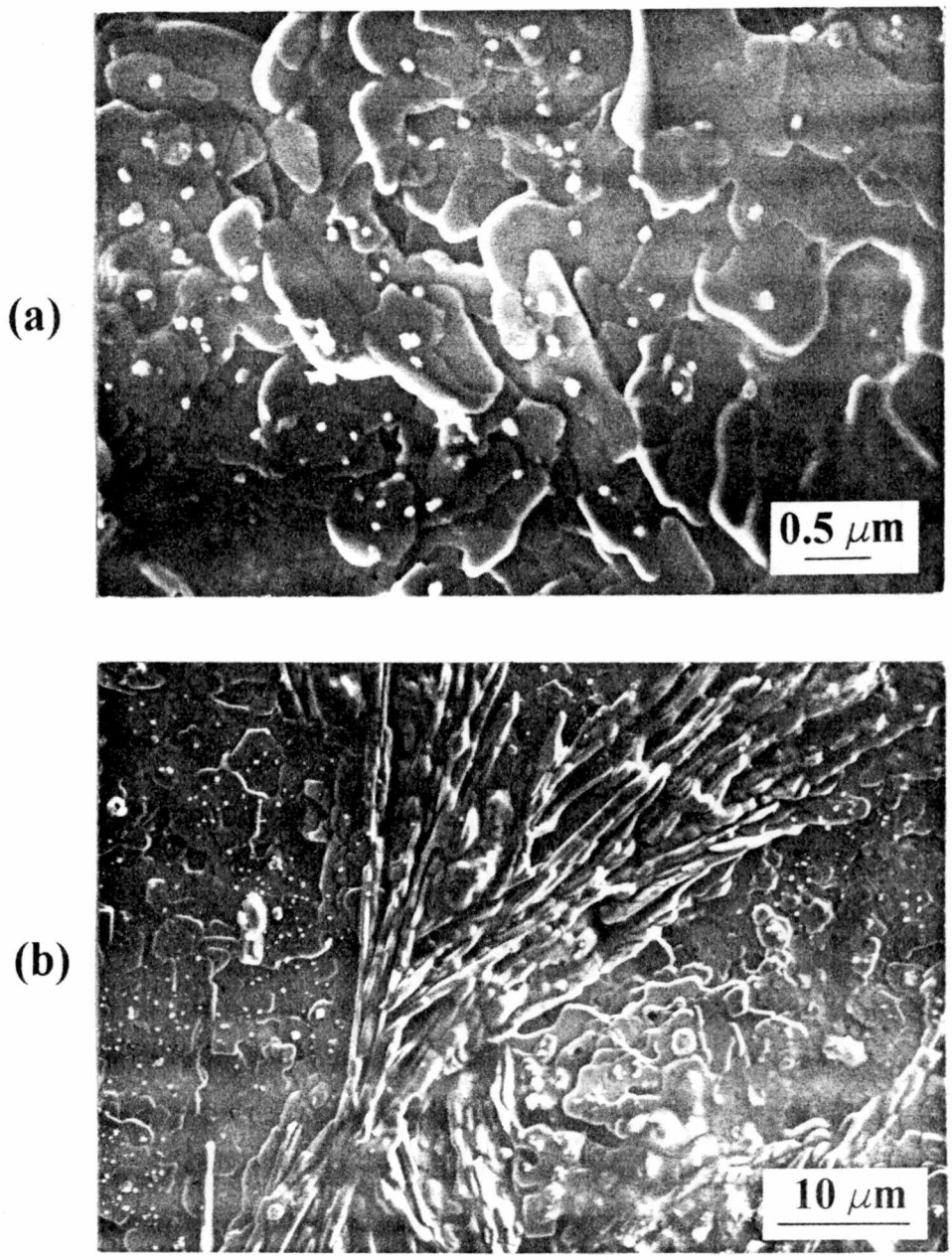


Figure 12 (a). SEM micrograph of the surface morphology of spin-coated Tl-1223 thick films on Ag, after annealing at T_{sample} of 860°C; (b). SEM micrograph of a different view of the same sample. Notice a small amount of fan-like structure.

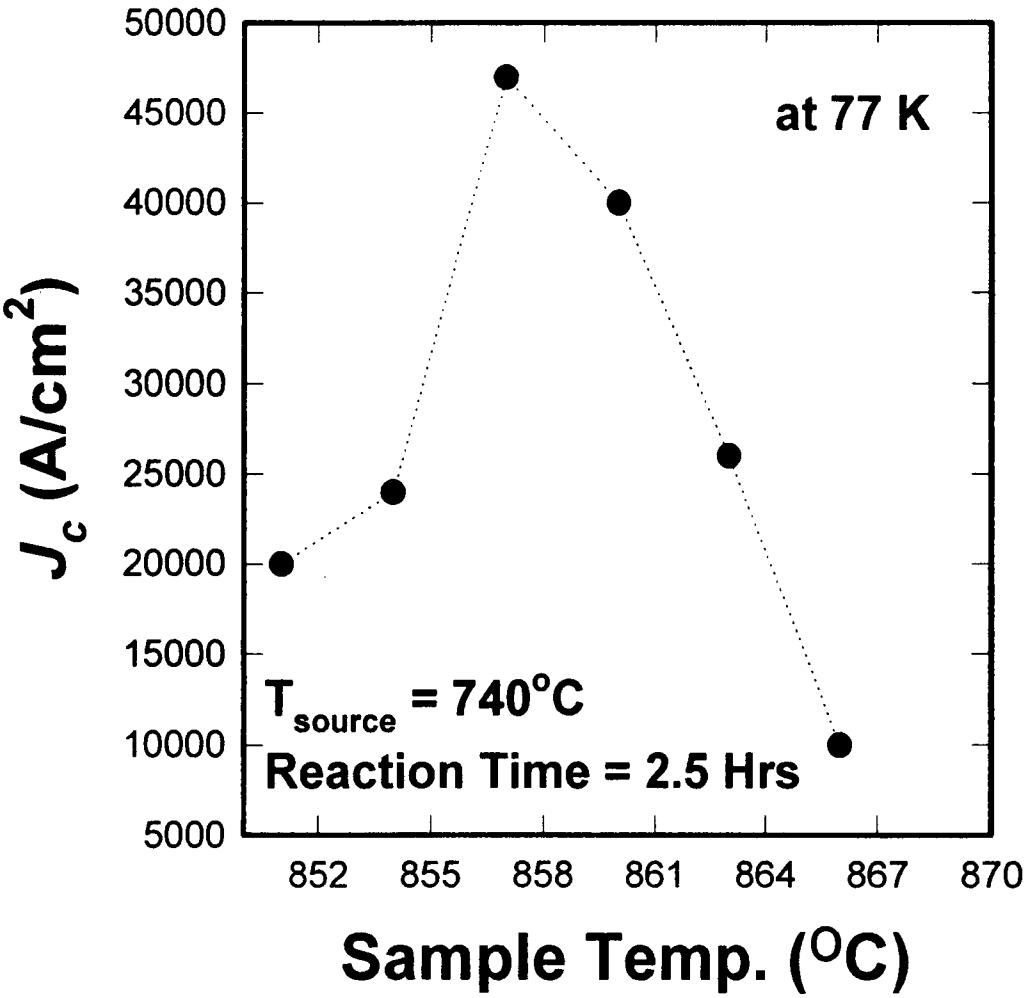


Figure 13 Transport J_c value at 77 K as a function of T_{sample} for a spin-coated Tl-1223 thick film on Ag. T_{source} was maintained at 740°C and the reaction time was about 2.5 hours. The highest J_c value is obtained at around 857°C.

4.1.2 Effect of the pressing process

In the spin-coating method for Tl-1223 films on Ag, the pressing process plays an important role in improving the texture and the J_c value of Tl-1223 thick films on Ag substrates. Figure 14 is the x-ray diffraction pattern from a spin-coated Tl-1223 thick film on Ag without the pressing process, showing a random orientation. The transport J_c is only about 1000 A/cm^2 at 77 K. The rough surface morphology for the unpressed spin-coated Tl-1223 thick film on Ag is shown in Figure 15 (a). However, the surface morphology for the pressed spin-coated Tl-1223 film on Ag is very smooth, as shown in Figure 15 (b). The surface profile curves for the samples with and without pressing, shown in Figure 16, also reveal that the pressing process can improve the surface smoothness. The unpressed precursor films are also very loose due to the burn-out of the organic materials in the film. On the contrary, the pressed deposits possess dense, homogeneous, overlapping plate-like structure, and well-connected parallel grain morphology, as shown in Figure 17 (a) which indicates the SEM micrographs of a cross-section morphology from the pressed Tl-1223 thick film on Ag. Some small impurity phases and Ag-rich nodules are also found in the thick film, possibly contributing to increase flux pinning. With higher magnification shown in Figure 17 (b), it is found that the film/substrate interface is very clean, with no evidence of interface reaction or interdiffusion. The major advantage of the pressing process is to density the precursor film, which leads to improved *c*-axis orientation. A high degree of *c*-axis texture is indicated in the x-ray diffraction pattern of Figure 18 by the presence of only (00*l*) peaks for the Tl-1223 phase. The (006) rocking curve shows a FWHM of 3.8°. The appearance of the plate-like structure is also consistent with the high degree of *c*-axis orientation. The J_c value for the

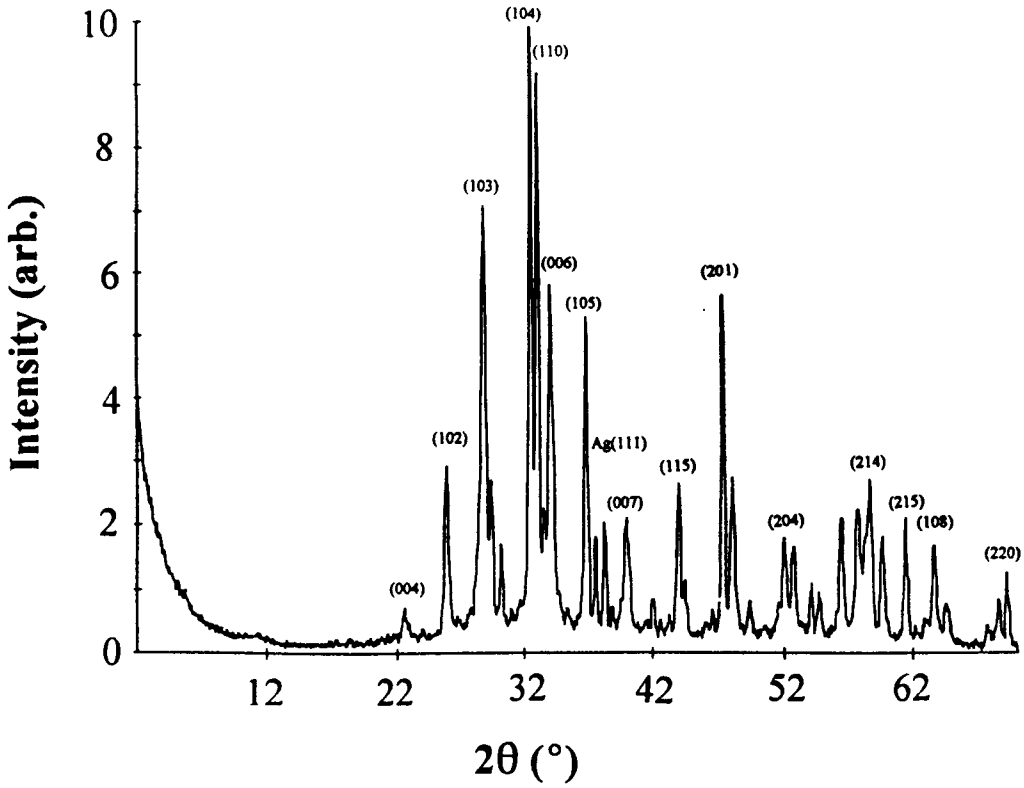


Figure 14 X-ray diffraction pattern from a spin-coated Tl-1223 thick film on Ag without pressing process, showing the Tl-1223 phase with random orientation.

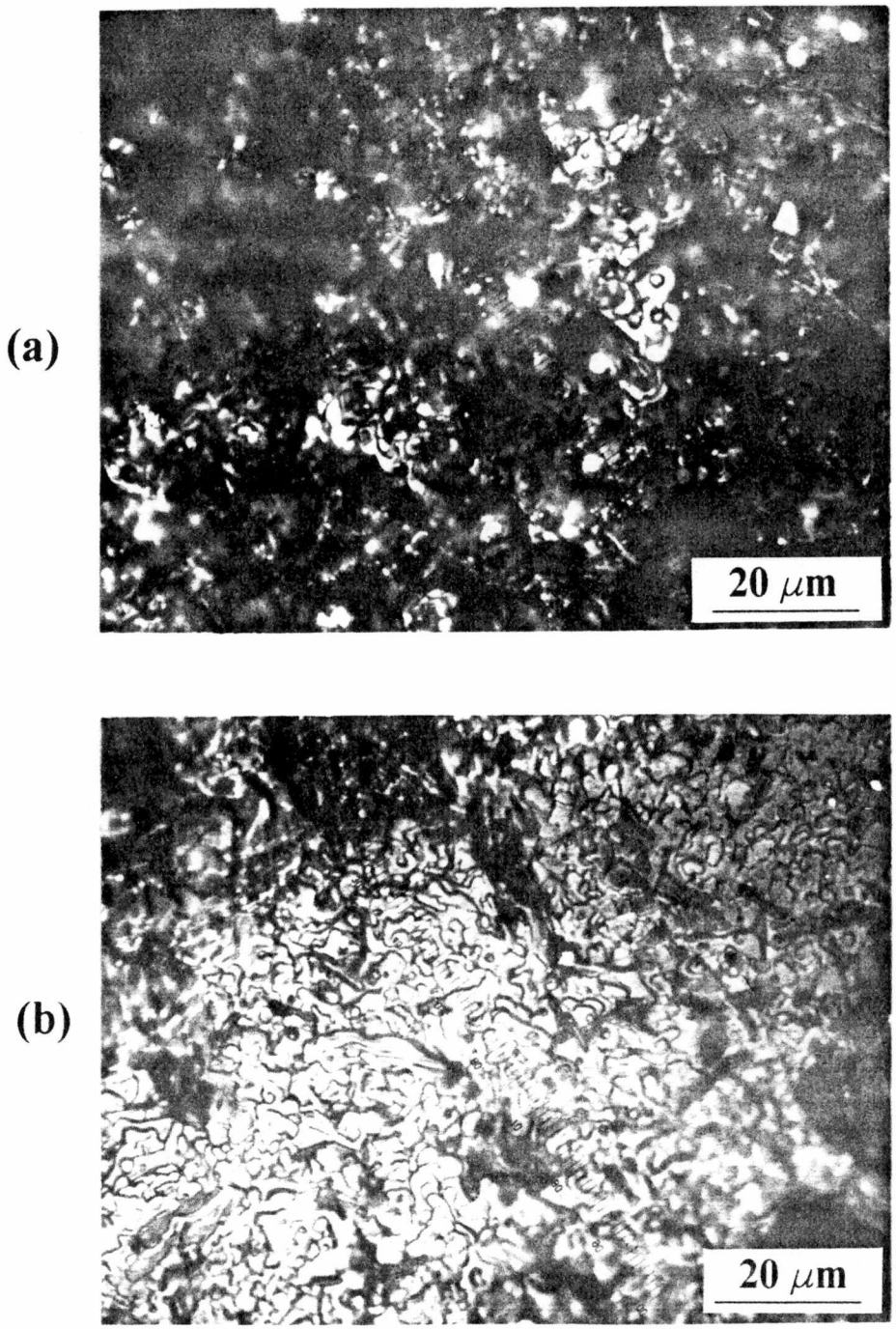


Figure 15 (a). Surface morphology of spin-coated Tl-1223 thick film on Ag without pressing process, showing rough surface; (b). Morphology of the spin-coated Tl-1223 thick film on Ag with pressing process, showing smooth surface.

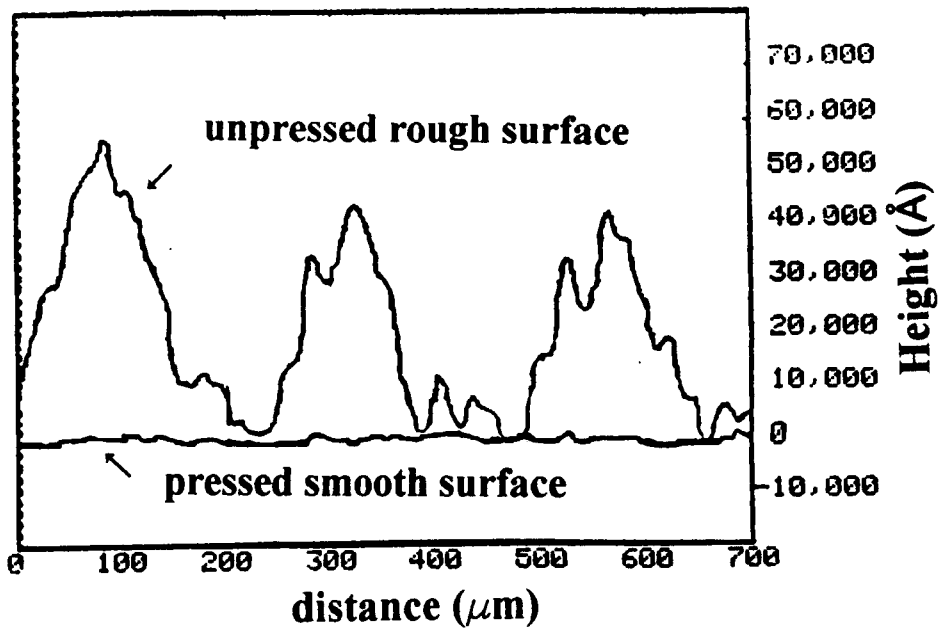


Figure 16 Surface profiles of spin-coated Tl-1223 thick films on Ag: upper curve shows the rough surface of a spin-coated thick film without pressing process, lower surface profile curve illustrates a flat surface of a spin-coated Tl-1223 thick films with pressing process.

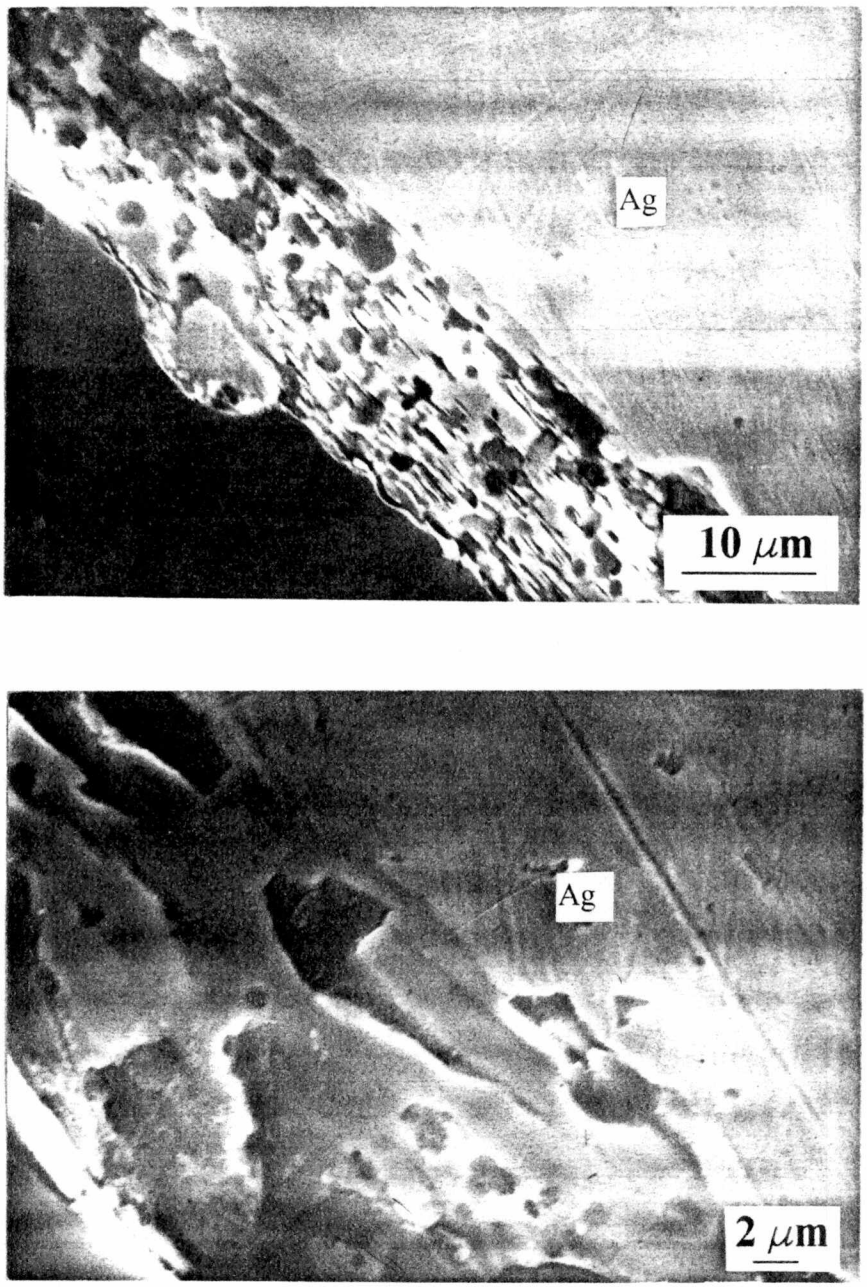


Figure 17 (a). SEM micrograph of a cross-section of spin-coated Tl-1223 thick film on Ag substrate, after annealing at 860°C. (b). SEM micrograph of the same cross-section at higher magnification.

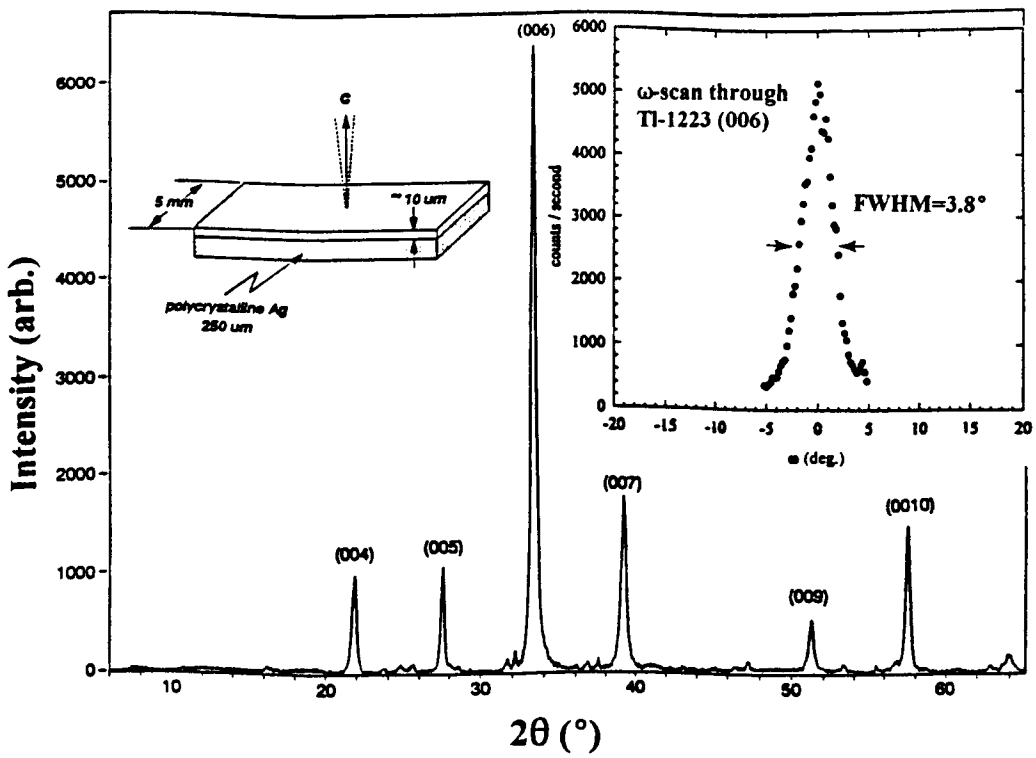


Figure 18 X-ray diffraction pattern of spin-coated and pressed Tl-1223 thick film on Ag. A high degree of *c*-axis texture is indicated by the presence of only the (00*l*) peaks for the Tl-1223 phase. The rocking curve shows the FWHM for the (006) refection is 3.8°.

pressed sample is in the range of 2 - 5×10^4 A/cm^2 at 77 K, which is 20-50 times higher than that of the unpressed sample. These large differences in J_c seem directly related to the improved *c*-axis orientation. To evaluate the degree of in-plane texture, XRD ϕ scans were used, with x-ray beam size of 0.5×0.5 mm^2. For this sampling area, the basal-plane orientation is nearly random overall, but exhibits some areas of strong in-plane alignment, indicative of a colony microstructure, as shown in Figure 19. Within a colony, most grain boundaries have small misorientations, and current flow should not be weak-linked. Two possible modes for non-weak-linked inter-colony current flow may be envisioned.[80, 81] First is a percolative path of small angle tilt boundaries at colony boundaries. Second is the current flow between overlapping grains at colony intersections through *c*-axis twist boundaries.

4.1.3 Superconducting properties of the Tl thick film

Figure 20 shows the temperature dependence of the J_c value for the spin-coated Tl-1223 thick films. The J_c value rises nearly linearly with decreasing temperature. Electrical transport measurements on eight different deposits gave zero resistance T_c values of 103 K to 109 K, and J_c (77 K) values in the range of 2 to 5×10^4 A/cm^2. Typical J_c values were measured in the 4-mm voltage contact distance. But, when using 1 mm voltage contact distance, the J_c value in one sample has reached 8×10^4 A/cm^2 at 77 K. This is consistent with the XRD observation of some small areas which have good in-plane texture, which corresponds to higher J_c values. It is in consistent with the XRD analysis above. In Figure 21, we compare results of the J_c (77 K) vs. H (H//c-axis) for the present spin-coated Tl-1223 deposits on Ag with other Tl-1223 materials: an excellent and a typical spray-pyrolyzed

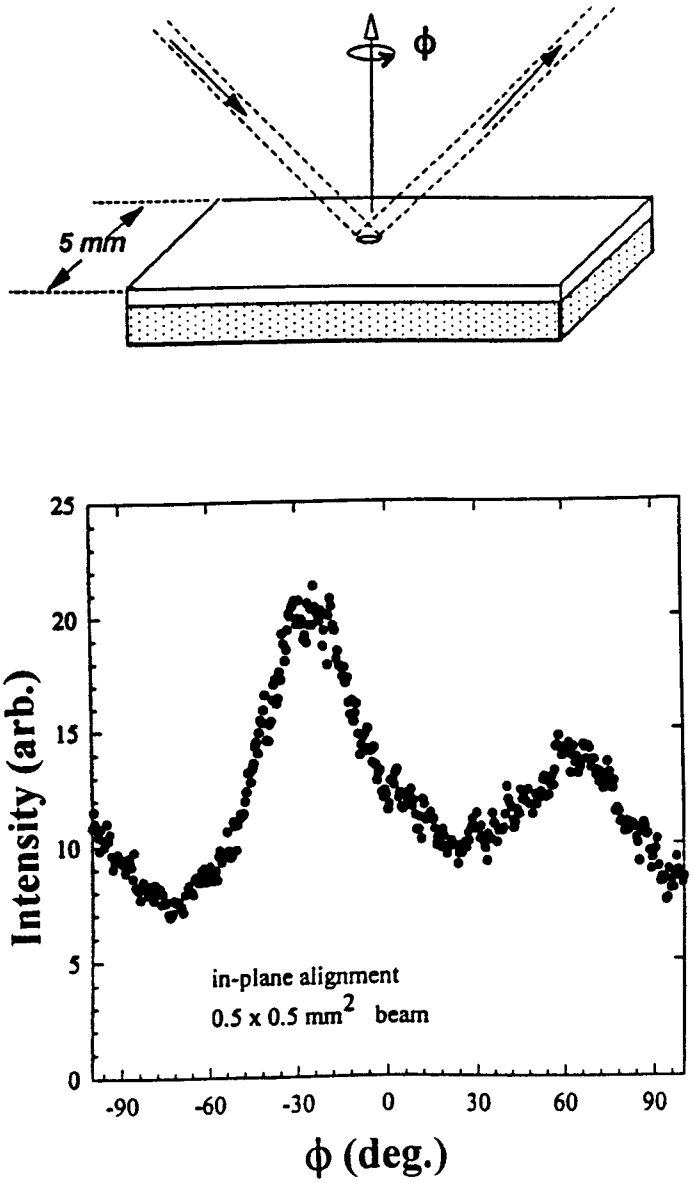


Figure 19 X-ray ϕ-scan from spin-coated Tl-1223 film on Ag substrate. Strong local in-plane texture is observed using a beam size of 0.5×0.5 mm^2.

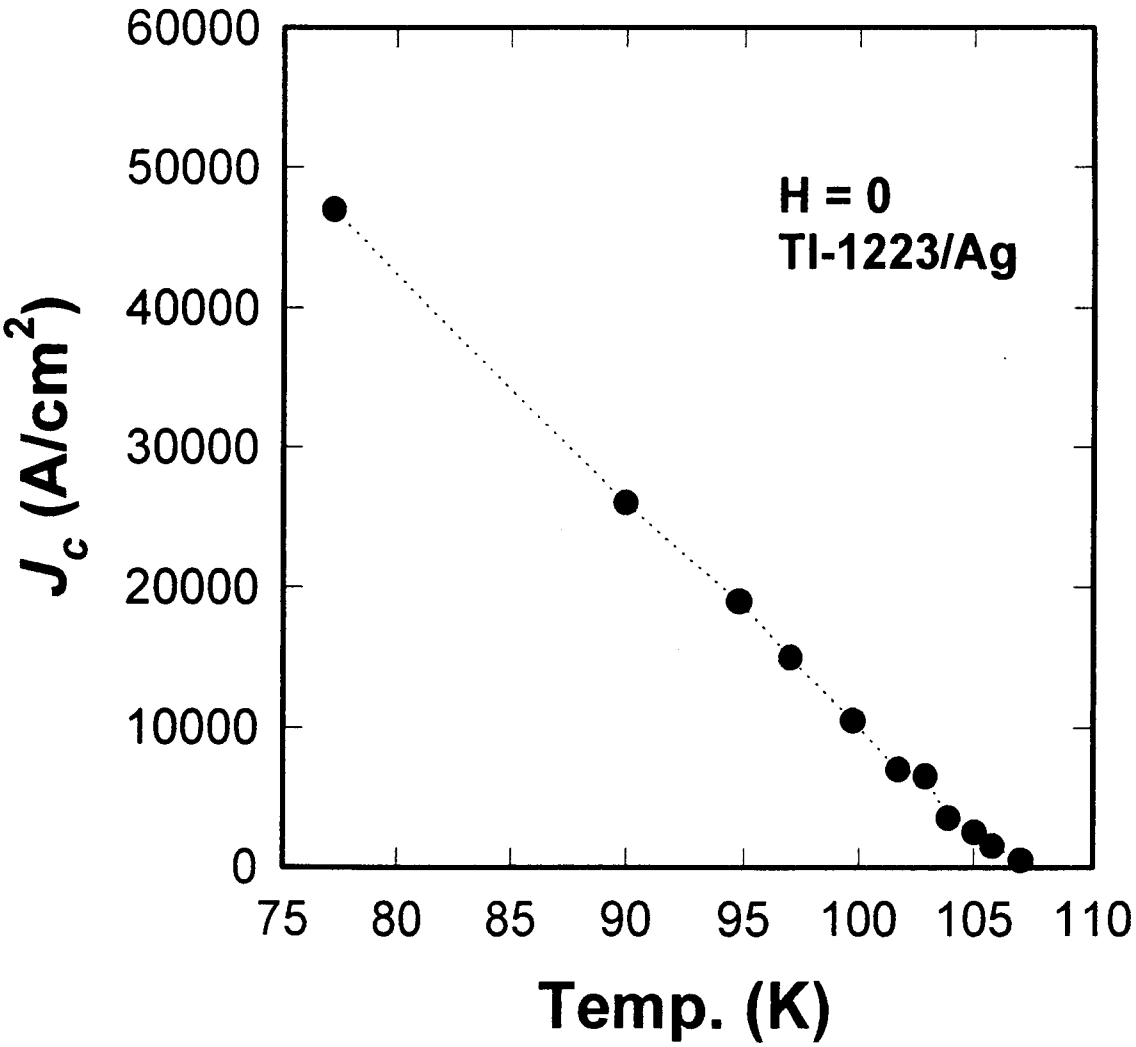


Figure 20 Temperature dependence of the transport J_c value from spin-coated Tl-1223 thick films on Ag substrates.

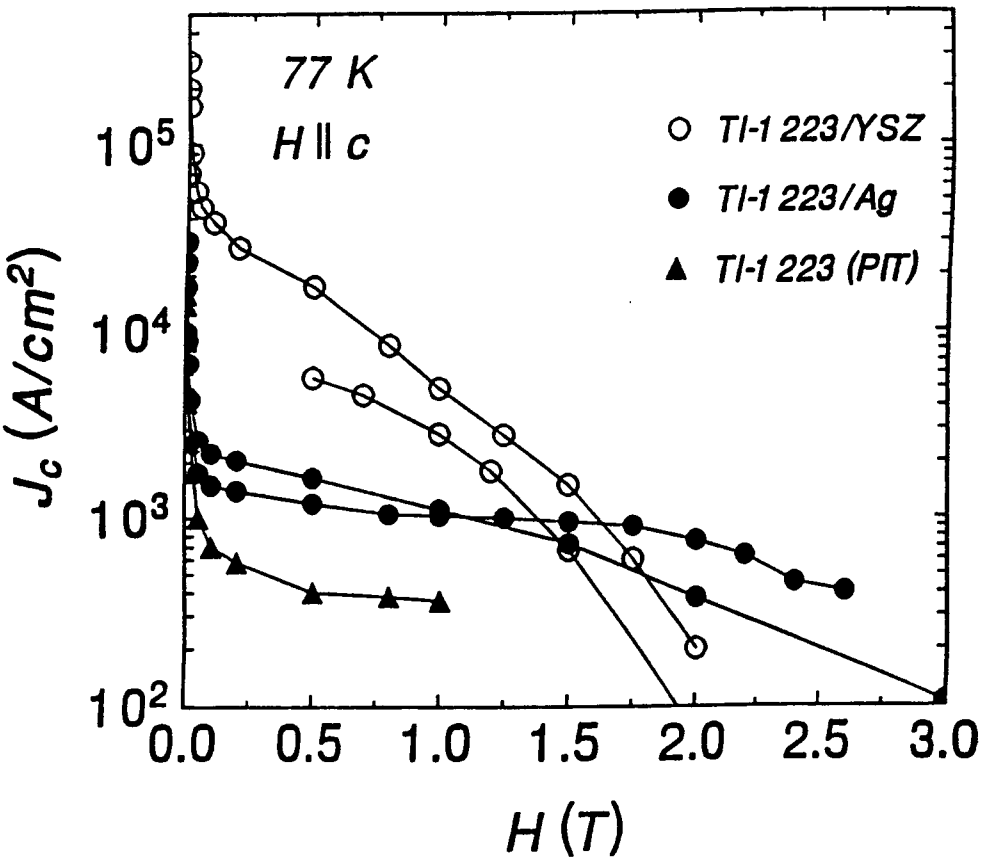


Figure 21 Magnetic field, H, dependence of transport J_c values at 77 K with H parallel to the nominal *c*-axis for spin-coated Tl-1223 thick film on Ag (Tl-1223), spray-pyrolyzed Tl-1223 thick film on YSZ (Tl-1223/YSZ), and powder-in-tube Tl-1223 tape (Tl-1223-PIT).

Tl-1223 film on YSZ, and a typical powder-in-tube Tl-1223 tape. At low field, the J_c values for spray-pyrolyzed Tl-1223 on YSZ are highest; above about 1.5 Tesla, however, the spin-coated Tl-1223 films on silver provide a systematically higher J_c value. This result may indicate a stronger flux-pinning microstructure in the spin-coated deposits since both types of materials exhibit evidence for strongly linked, percolative current paths. From the microstructure analyses, we see that the spin-coated Tl-1223 thick films have poorer out-of-plane orientation with FWHM of 4-12°, less defined local in-plane texture and larger amount of impurity particles than the spray-pyrolyzed films whose FWHM is about 2.0°. Therefore, the presence of *c*-axis misaligned grains may cause the weak link problem, and the large amount of impurity may contribute to the strong pinning. The more highly developed colony microstructure of the spray-pyrolyzed film accounts for its larger J_c values in low fields, while the relatively poor performance of the Tl-1223 powder-in-tubes tapes is ascribed to a smaller fraction of well-connected current paths, which are limited by the random grain orientations.

Figure 22 shows the field dependence of J_c values at 40 K for spin-coated Tl-1223 thick film, spray-pyrolyzed Tl-1223 film on YSZ, powder-in-tube Bi-2223 tape, and powder-in-tube Tl-1223 tape. At fields from 1 to 5 Tesla, the Tl-1223 conductors have a nearly constant J_c, with order-of-magnitude improvements over powder-in-tube Bi-2223 tape. These results are indicative of the higher irreversibility field in Tl-1223 due to its less anisotropic material and electronic properties.[82] Comparisons near 40 K are particularly useful, since that temperature seems to mark a break point for inexpensive, single-stage cryogenic closed-cycle coolers. From Figures 21 and 22, we see that the field dependence of J_c values for spin coated Tl-1223 thick film on Ag at 40 K and 77 K are superior to that for powder-in-tube Tl-1223

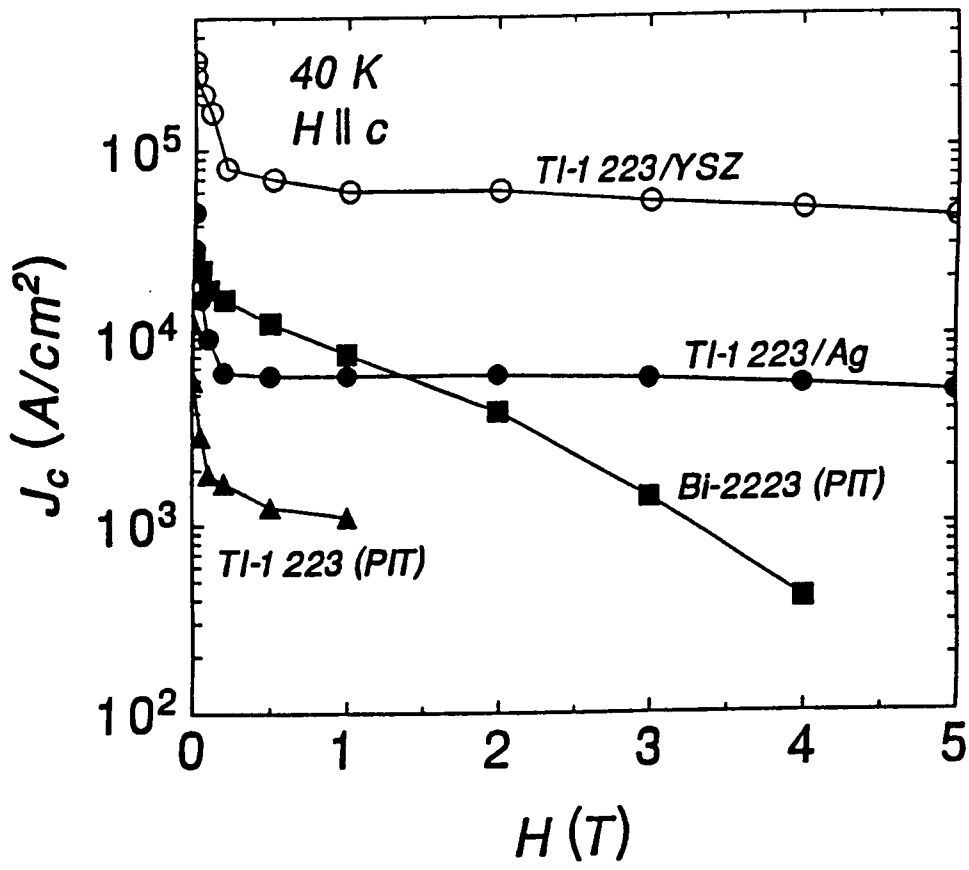


Figure 22 Transport J_c values at 40 K as a function of applied magnetic field H parallel to *c*-axis for the spin-coated Tl-1223 thick film on Ag, spray-pyrolyzed Tl-1223 thick film on YSZ (Tl-1223/YSZ), powder-in-tube Bi-2223 tape (Bi-2223-PIT), and powder-in-tube Tl-1223 tape (Tl-1223-PIT).

tape, again indicating that the Tl-1223 thick films on Ag are far less weak-linked than powder-in-tube Tl-1223 tape. These results indicate the enormous potential of the Tl-1223 thick films on Ag for high temperature and high field applications.

From the data above, we see that uniaxial orientation improves the grain boundary connectivity and the transport J_c in comparison with the random oriented HTS. However, the weak link behavior still remains. Overall, the transport J_c of HTS with uniaxial orientation is less than 10% of that achieved in epitaxial films of the same materials. To overcome the weak link problem, we should achieve the biaxial crystal orientation (both c-axis and in-plane texture).

4.2 RABiTS Technique

4.2.1 Noble metal buffer layers on Ni tapes

We are interested in noble buffer layers, especially Ag, due to their chemical and structural compatibility with HTS[83] and the successful growth of epitaxial YBCO films on single crystal Ag substrates.[84] It is difficult to grow biaxially textured Ag film on Ni directly. Hence, we thought about using an intermediate layer of Pd between the Ag layer and Ni substrate. Biaxially oriented intermediate Pd films with a thickness of 500-2000 Å were successfully deposited on the textured Ni at temperatures between 300-550°C. Ag films were then deposited on the Pd-buffered Ni substrates at a temperature of 250-350°C. Figure 23 is a typical x-ray θ-2θ spectrum for a Ag/Pd/Ni buffer layer, which indicates the presence of only (00*l*) peaks of Ag, Pd, and Ni, so that only cube axes are oriented perpendicular to the substrate surface. In Figure 24, the ϕ-scans for Ni, Pd, and Ag show clear fourfold symmetry,

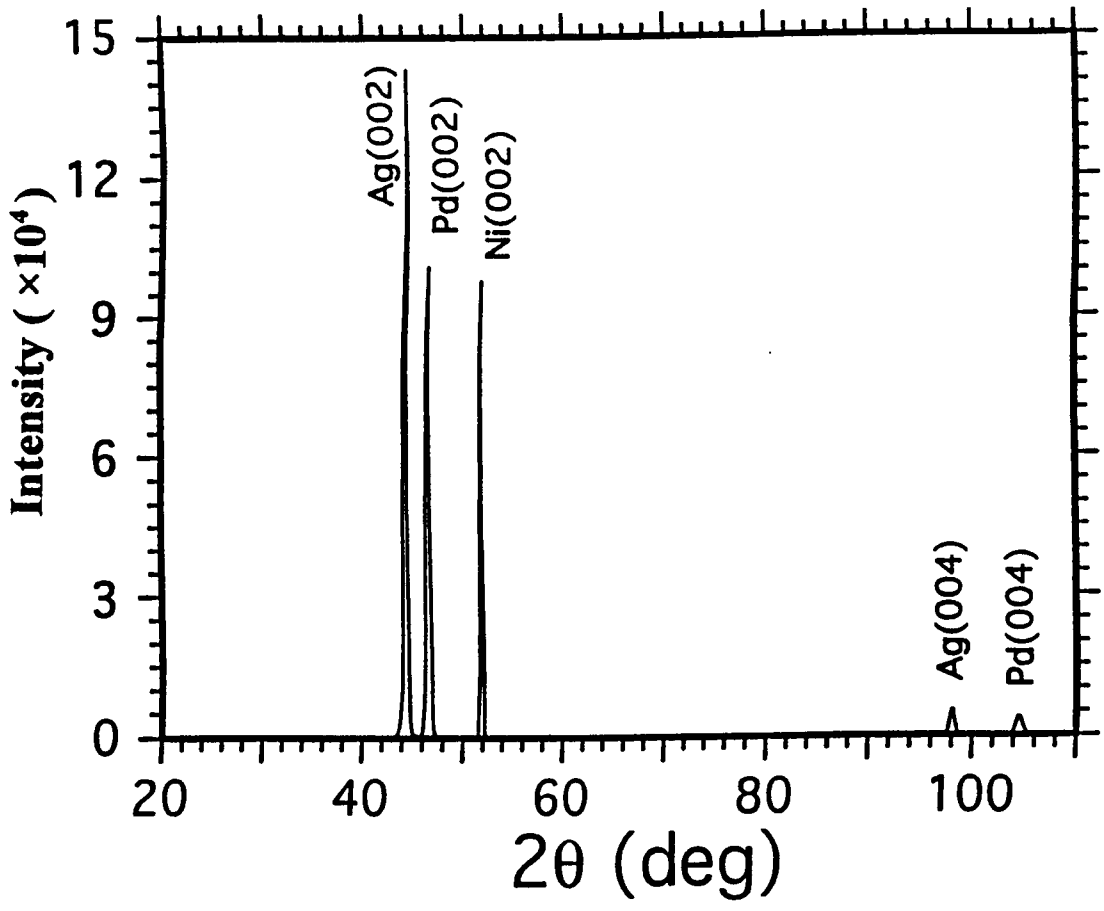


Figure 23 X-ray θ-2θ scan for the Ag/Pd/Ni laminates, indicating the presence of only (00*l*) peaks. The Pd was deposited at 500°C followed by Ag deposition at 300°C.

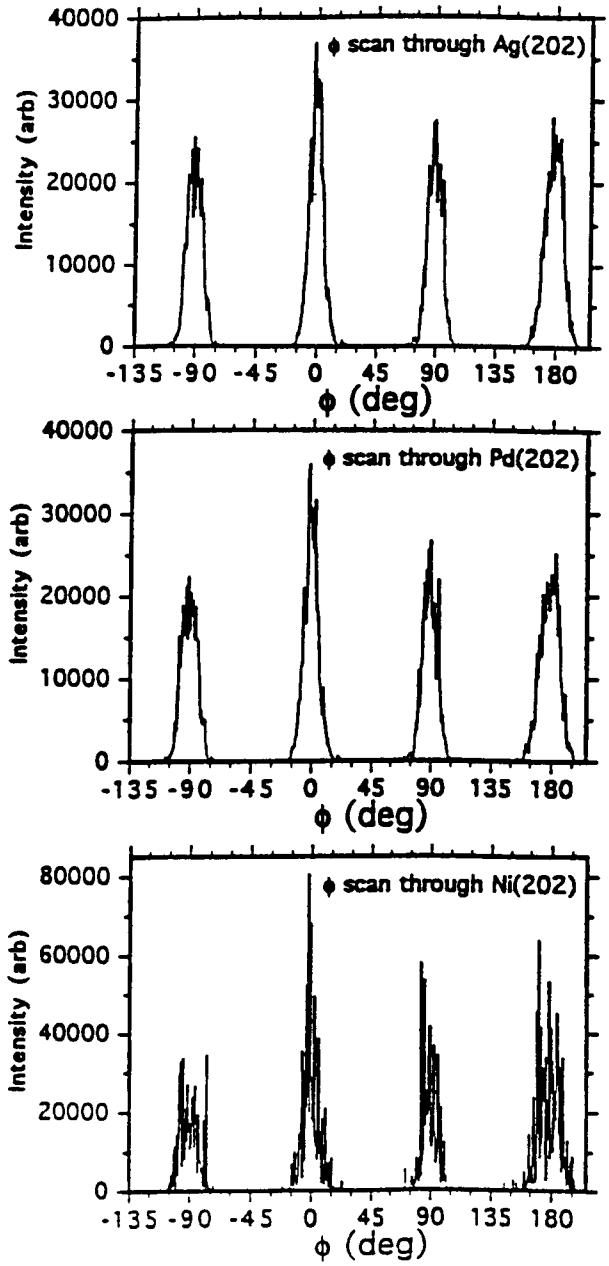


Figure 24 X-ray ϕ-scans for Ag (202), Pd (202), and Ni (202) in the Ag/Pd/Ni laminates, revealing clear fourfold symmetry for each layer.

exhibiting good in-plane alignment for each layer with similar $\Delta\phi$ FWHM of about 6°-8°. Figure 25 shows the (002) rocking curves for Ni , Pd and Ag, with FWHM of ~7°, 1.75° and 1.3°, respectively, indicating progressive improvement of out-of-plane orientation in subsequent layers. Due to the coarse-grained nature of the rolled-textured substrate, the rocking curve for the Ni seems very rough. The reason for the improvement of the out-of-plane orientation may be due to alignment with the smooth surface rather than direct out-of-plane epitaxy. Another noble metal buffer layer Pt has also been epitaxially deposited on the textured Ni at temperature of 500°C, as shown in Figure 26. The FWHM values for ω-scan and ϕ-scan are 7° and 10°, respectively.

A two-step process has been developed to grow biaxially oriented Pd films on the Ni tapes, i.e., depositing the Pd films at room temperature (RT), followed by post-annealing in a vacuum at about 500°C for 10-30 min. While epitaxy is established at RT, the post-annealing treatment improved both the out-of-plane and in-plane orientation, as evidenced in Figures 27 and 28 by FWHM values of ω- and ϕ-scans that have been reduced from 2.9° and 10° in the as-deposited Pd film to 1.9° and 6°, respectively, in the post-annealed one. This result may be explained by dislocation theory. As the Pd film is deposited onto a clean nickel surface at RT, small Pd islands are generated early in deposition growth and are strained to match the nickel substrate. Larger islands are separated from the substrate by misfit dislocations. The dislocations are in edge orientation, have Burgers vectors in the interface, and are arranged in a square net. Besides the line defects, there are also many point defects, grain boundaries and stacking faults generated in the films during the deposition at low temperature. Point defects include vacancies, interstitials, and impurity atoms. Therefore,

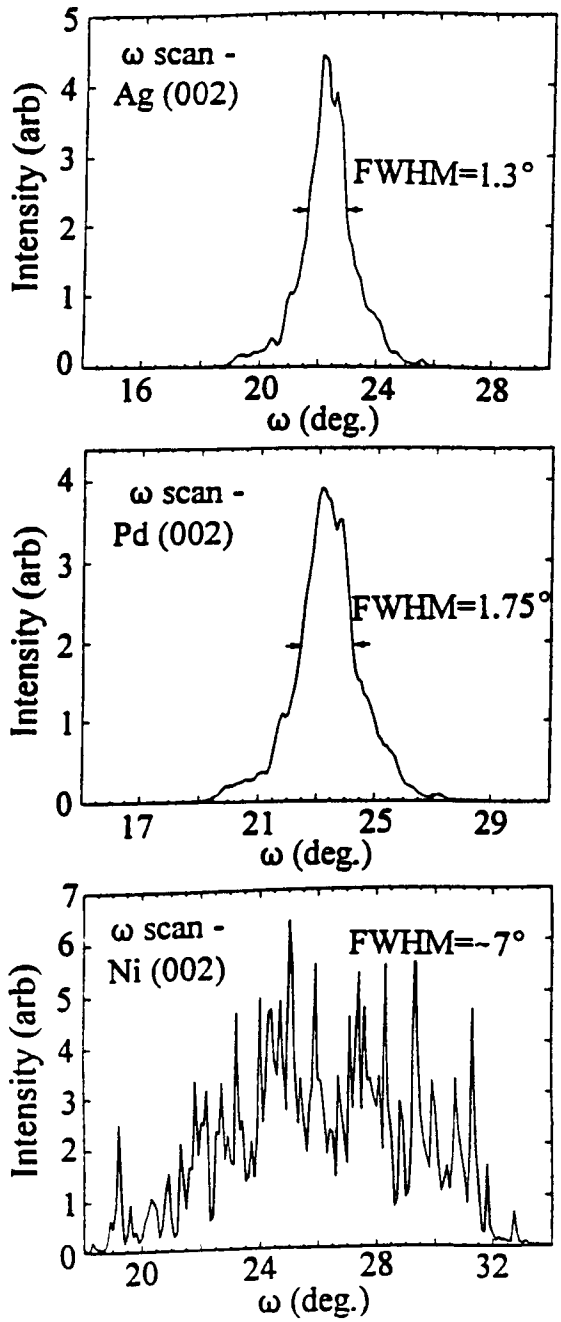


Figure 25 X-ray ω-scans for the Ag/Pd/Ni laminates, showing the progressive improvement of out-of-plane orientation in subsequent layers.

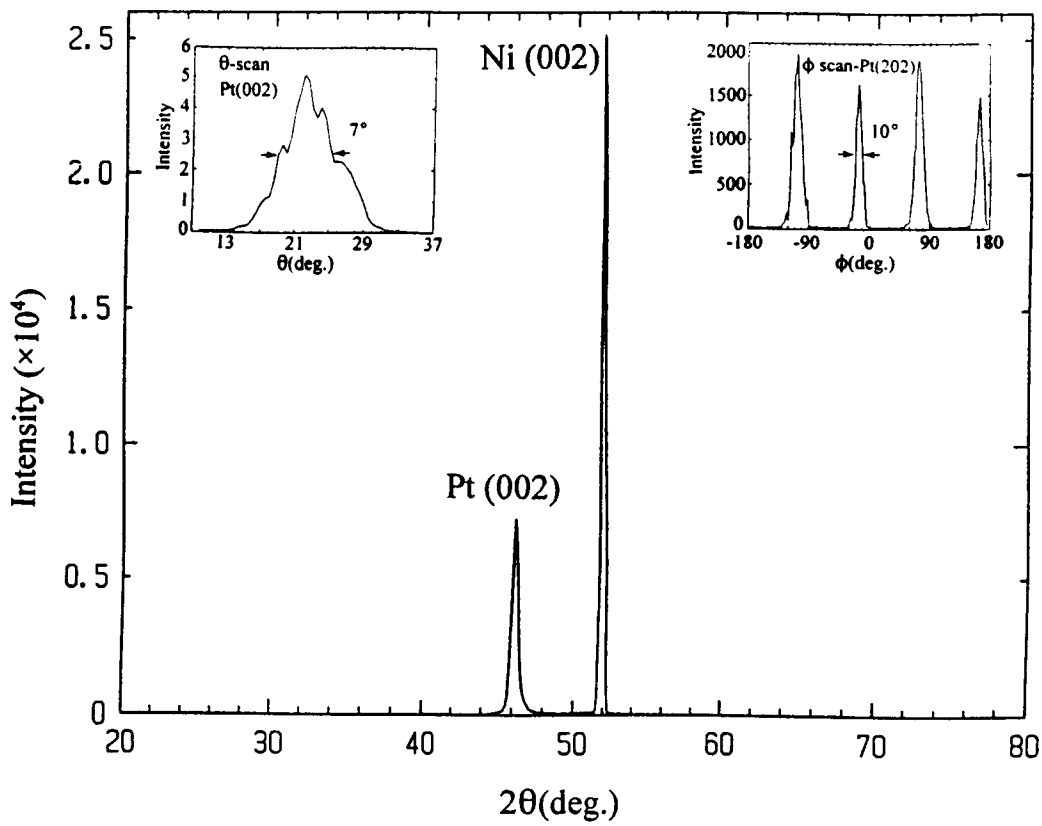


Figure 26 X-ray θ-2θ scan, ω-scan, and ϕ-scan for the Pt/Ni laminates, revealing that the Pt film has good out-of-plane and in-plane orientations.

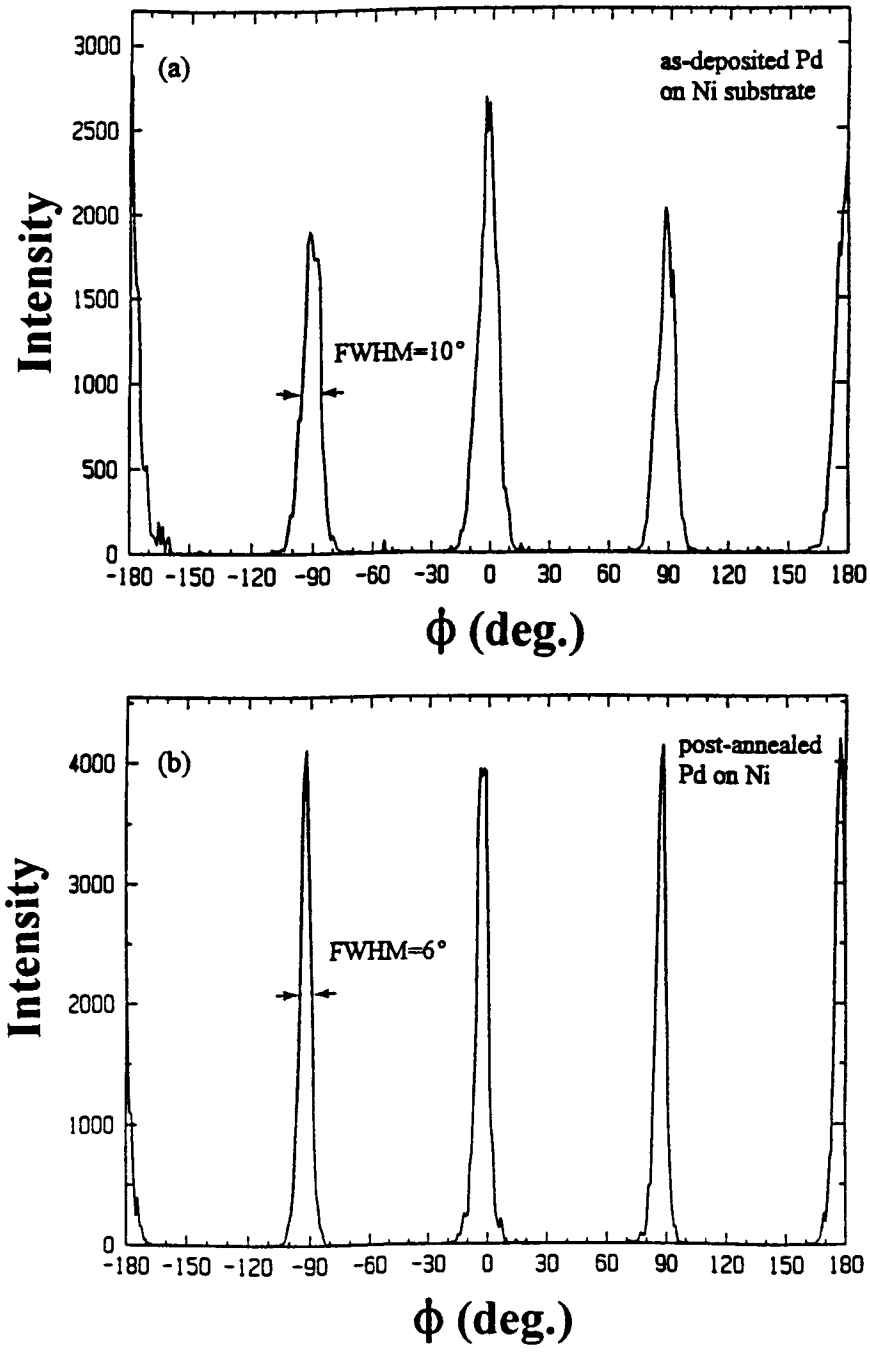


Figure 27 X-ray ϕ-scans through Pd (202) for the as-deposited Pd film and for the post-annealed Pd film.

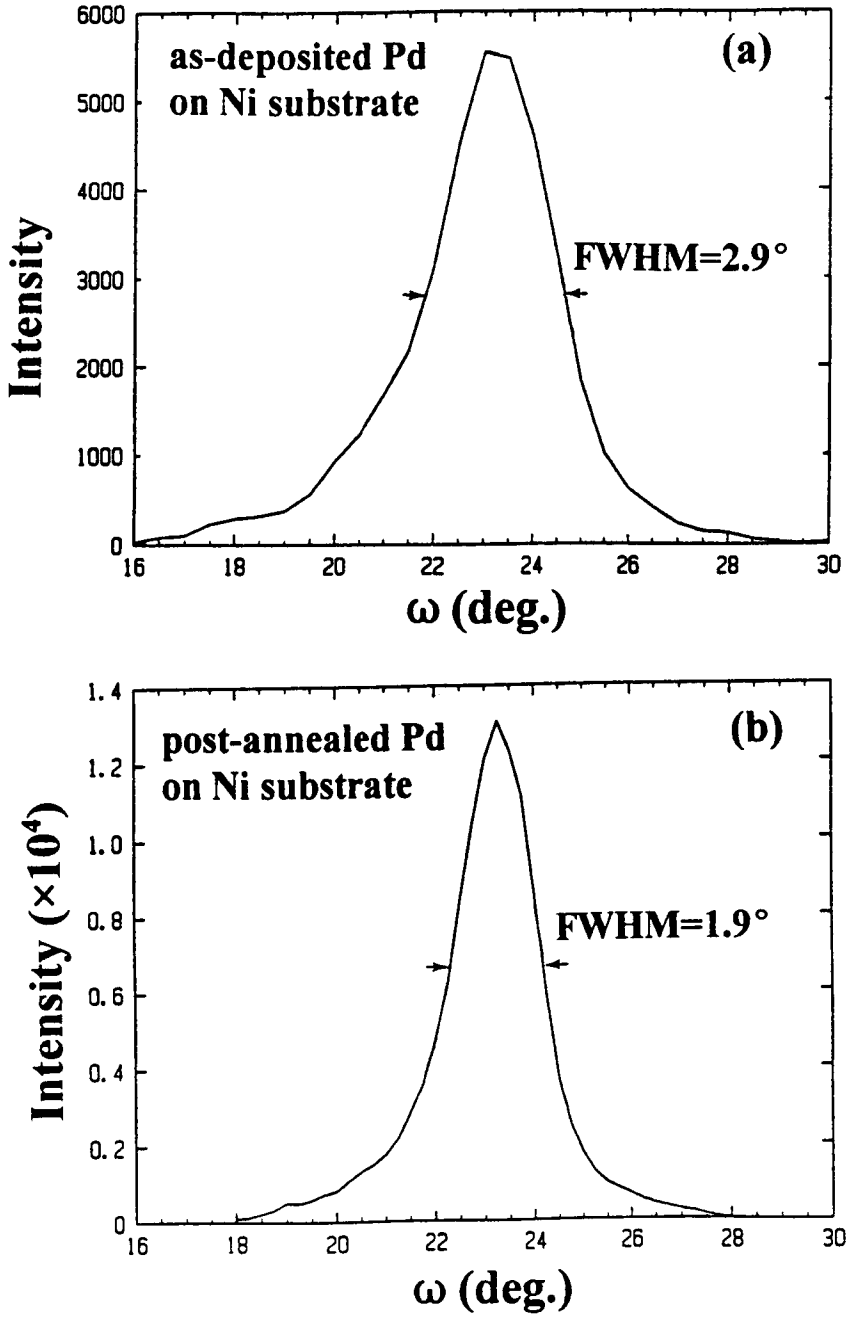


Figure 28 X-ray ω-scans through Pd (002) for the as-deposited Pd film and the post-annealed Pd film on the Ni. Post-annealing improves the out-of-plane orientation of the Pd film.

the structure of the Pd films is imperfect with poorer out-of-plane and in-plane orientations. During post-annealing, however, some of the dislocations become mobile. If the dislocations are in edge orientation and have Burgers vectors parallel to the interface plane, then the motion is by climb. If their Burgers vectors are inclined to this plane, then the motion is a mixture of climb and glide. In either case, the dislocation density can be reduced. The annihilation among the point defects also occurs during annealing. Therefore, the out-of-plane and in-plane orientations of the film can get better due to the reduced defect density and the improved crystallization. The two-step process may be important in reducing the costs of large-scale fabrication. The post-annealing step can be omitted if additional layers need to be deposited on the Pd film at high temperature.

The surface condition of a substrate can greatly affect epitaxy and integrity of buffer layers and hence the J_c value of the superconducting films. This effect was demonstrated by preparation of a rolled Ni substrate, mechanically polished on one half, while the other half remained unpolished (nominal, as-rolled rough surface). After the texture anneal at 400°C in vacuum and the deposition of Pd over the entire surface, the sample was subjected to ϕ-scans and ω-scans on both the polished and unpolished halves. While the in-plane orientation in this case is about the same for each region (FWHM is about 10°), the FWHM values for out-of-plane ω-scans were 1.56° and 0.85° on the unpolished and polished surfaces, respectively, as shown in Figure 29, indicating that the improvement in out-of-plane alignment in subsequent overlayers appears directly related to the smoothness of the base-metal substrate surface. However, we have found that mechanical polishing of the base metal is not necessary, provided sufficiently well-polished rolls are utilized in the rolling deformation process, since

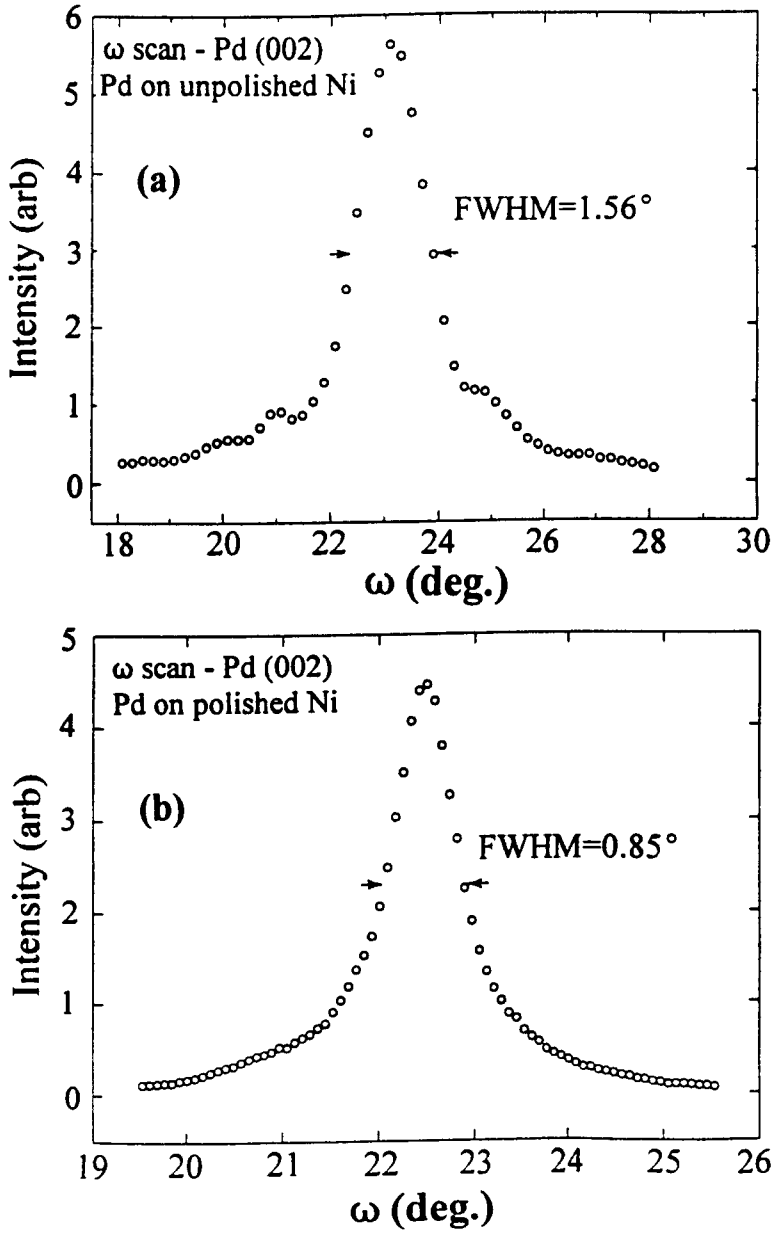


Figure 29 X-ray ω-scans through the Pd (002) reflection for the Pd films on polished and unpolished Ni substrate, showing that polishing the Ni can improve the out-of-plane alignment of the Pd film.

it is important for scale-up to long lengths to obtain substrates with surfaces adequate for film growth without the need for a cumbersome polishing step.

4.2.2 CeO_2 buffer layer on Pd-buffered Ni tapes

CeO_2 is a desired buffer layer due to the high melting temperature and lower lattice mismatch with YBCO. Traditionally, deposition of oxide films occurs at high temperatures and in an oxidizing ambient. For example, (001) oriented, biaxially textured CeO_2 films were grown at 750°C.[85] Continuous film deposition on long Ni tape at such high temperature not only requires elaborate substrate heating systems but also easily cause oxidation of the Ni substrate surface and interdiffusion, which are detrimental to epitaxial growth. After failing to grow biaxially textured CeO_2 films on the Pd-buffered Ni tapes at high temperature of 750°C, quite by chance we found that biaxially textured CeO_2 films can also be grown on the Pd-buffered Ni tapes at room temperature, and that the post-annealing can improve the biaxial orientations. Figures 30 (a) and (b) show the x-ray θ-2θ scans for the room-temperature-deposited CeO_2 on Pd-buffered Ni tape and for the same sample which has been post-annealed at 750°C. We see that *c*-axis oriented CeO_2 film can be grown on the Pd-buffered Ni at room temperature and that after post-annealing the Pd (00*l*) peaks have disappeared due to the interdiffusion of Pd film and Ni substrate, while the oxide overlayer remains intact. Figures 31 (a) and (b) indicate that as-deposited CeO_2 film possesses out-of-plane and in-plane orientations with FWHM values of the ω- and ϕ-scans about 10° and 15.6°, respectively. After post-annealing, the FWHM values of the ω- and ϕ-scans have been decreased to 8° and 11.5°, respectively.

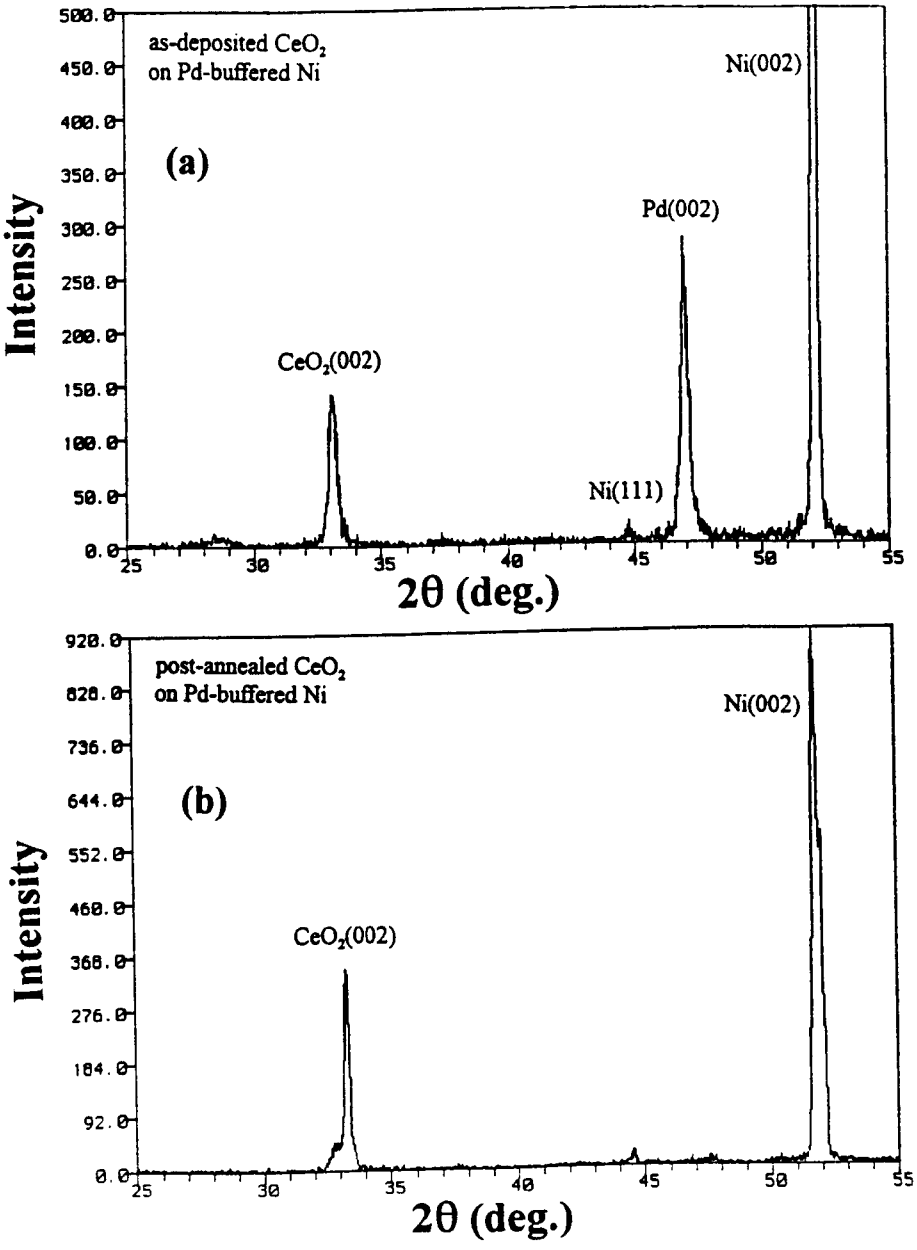


Figure 30 (a). X-ray θ-2θ scans for the room-temperature-deposited CeO_2 on Pd-buffered Ni substrate; (b). X-ray θ-2θ scan for the same sample that has been annealed at 700°C after deposition.

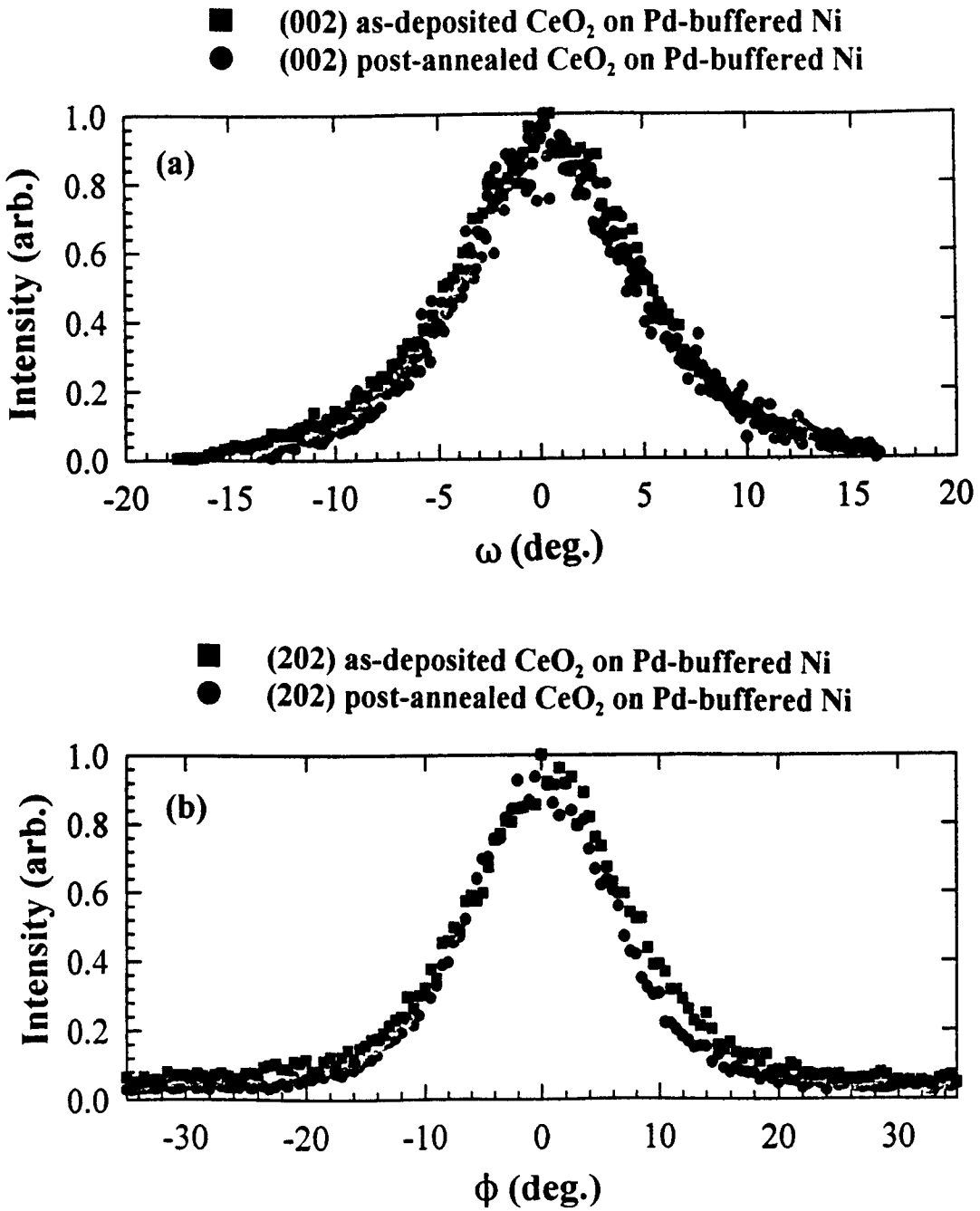


Figure 31 (a). ω-scans through CeO_2 (002) for as-deposited CeO_2 on Pd-buffered Ni with FWHM of 10° and for post-annealed sample with FWHM of 8°. (b). ϕ-scans through CeO_2 (202) for as-deposited CeO_2 on Pd-buffered Ni with FWHM of 15.6° and for post-annealed sample with FWHM of 11.5°.

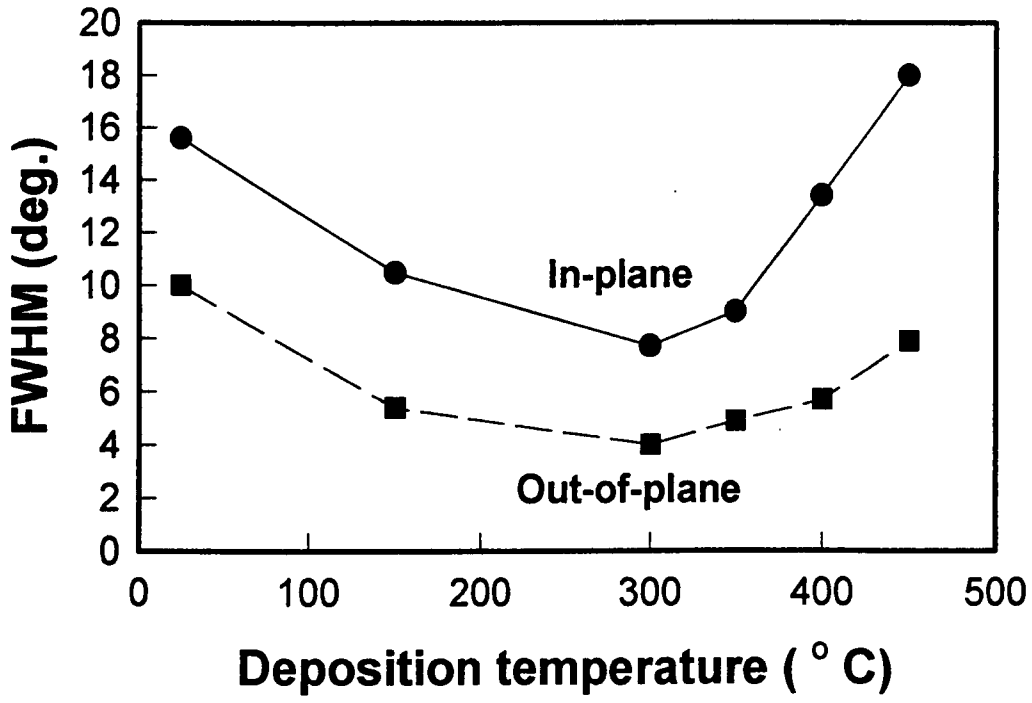


Figure 32 Dependence on deposition temperature of the FWHM values of x-ray ω-scans through CeO_2 (002) and ϕ-scans through CeO_2 (202) for the CeO_2 films deposited on Pd-buffered Ni tape.

The deposition temperature dependence of the biaxial orientations for the CeO_2 films grown on the Pd buffered Ni tapes was also investigated, shown in Figure 32. The CeO_2 films were deposited on pieces cut from the same Pd-buffered Ni tape. The curve shows that both the out-of-plane and in-plane orientations improve as the deposition temperature increases from 25°C to about 300°C, but degrade at higher temperature. The sharpest alignment is obtained at 300°C, with ω- and ϕ-scan FWHM of 4° and 7.7°, respectively. A probable explanation for this behavior stems from competing thermal effects. Atomic order in a stable oxide film such as CeO_2 generally improves with increasing deposition temperature. In the present case, however, the Pd noble metal layer undergoes thermally enhanced interdiffusion with the base Ni substrate. We have observed that this interdiffusion is accompanied by a general roughening of the exposed metal surface, although its overall crystalline texture is not lost. Thus, the optimum deposition temperature of about 300°C likely results from a competition between thermal ordering during CeO_2 growth, opposed by a degradation from increased surface roughness. The sample deposited at 300°C was also post-annealed at 750°C for 3 hours in 1 mTorr of oxygen. Different from the RT-deposited sample whose biaxial orientations have been improved after post-annealing, for the sample deposited at 300°C, the post-annealing causes the FWHM to increase from $\Delta\omega=4°$ and $\Delta\phi=7.7°$ to $\Delta\omega=4.5°$ and $\Delta\phi=10°$, respectively. The similar final alignments of the two starting samples likely result from the same competing effects cited above.

SEM studies of a CeO_2/Pd/Ni sample deposited at 300°C reveal uniform, smooth, and crack-free CeO_2 surfaces. However, while the sample still exhibits a smooth surface after post-annealing at 750°C, a few fine cracks have appeared, as shown in Figure 33. Such an

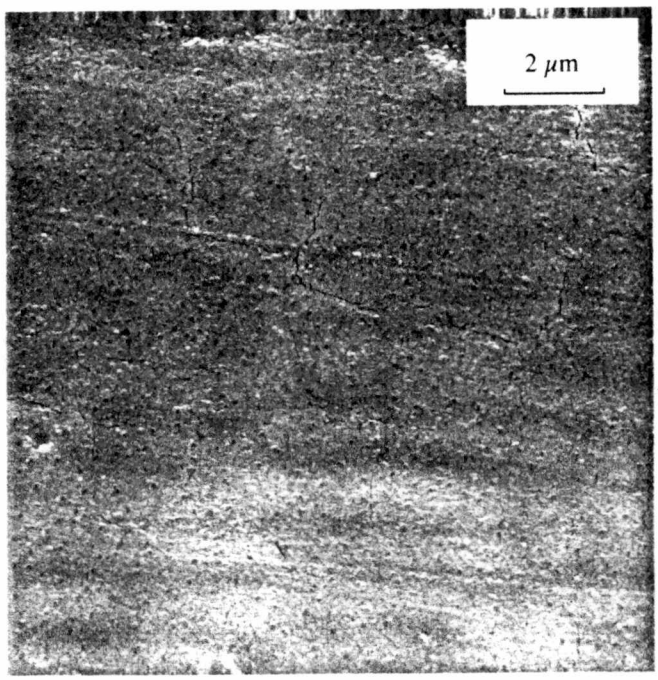


Figure 33 SEM micrograph showing the surface morphology of CeO_2 film on Pd-buffered Ni substrate, annealed at 750°C for 3 hours under 1 m Torr oxygen pressure. The film surface is smooth, but shows some cracks after the high-temperature treatment.

anneal at 750°C in low oxygen pressure is a simulation of the approximate conditions during the actual deposition of YBCO films. The appearance of the fine cracks is of concern, since they could lead to Ni contamination of the YBCO films. The cracks probably arise from differential thermal expansion between the Ni metal substrate and the CeO_2 ceramic film, which would result in a 0.15-0.3% compression of the CeO_2 without (partial) strain relief by crack formation. To avoid the cracks, a two-step deposition technique was used, where an initial thin layer of CeO_2 was deposited at low temperature, followed by subsequent CeO_2 deposition at temperatures 650-750°C. The high temperature deposition seems to repair the cracks, since SEM observation in Figure 34 shows much smaller and fewer cracks.

4.2.3 CeO_2 buffer layer grown directly on Ni using forming gas

Typically, the epitaxial growth of the oxide films requires high growth temperature and an oxidizing ambient which, however, may result in the formation of NiO layer. To grow the biaxially oriented oxide buffer layers directly on the Ni substrate, the crucial point is to avoid the formation of NiO on the Ni surface, which is detrimental to epitaxial growth. Here, a new process has been developed to deposit CeO_2 films directly on Ni tapes by using forming gas (Ar+4%H_2) as the sputtering ambient. Figure 35 shows the x-ray θ-2θ scan for a CeO_2 film grown on the Ni tape at 400°C by using forming gas. The presence of only (00*l*) reflections for CeO_2 indicate good *c*-axis orientation. Typically, x-ray ω-scans and ϕ-scans for such CeO_2 layers have FWHM values of 6°-8° as shown in the inset picture in Figure 35, and reveal that the CeO_2 films replicate the in-plane alignment of the Ni tape. In this process, forming gas is crucial for the deposition of CeO_2 on Ni, where the H_2 partial pressure ensures

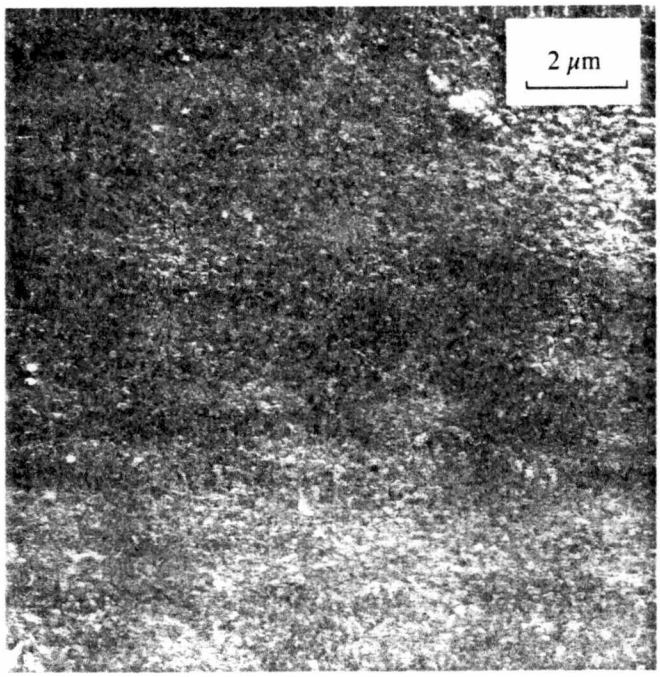


Figure 34 SEM micrograph of the surface morphology from the CeO_2 film on Pd-buffered Ni substrate. The initial layer of CeO_2 film was grown at low temperature followed by the high temperature (750°C) deposition. Only small amounts of crack remained on the CeO_2 film.

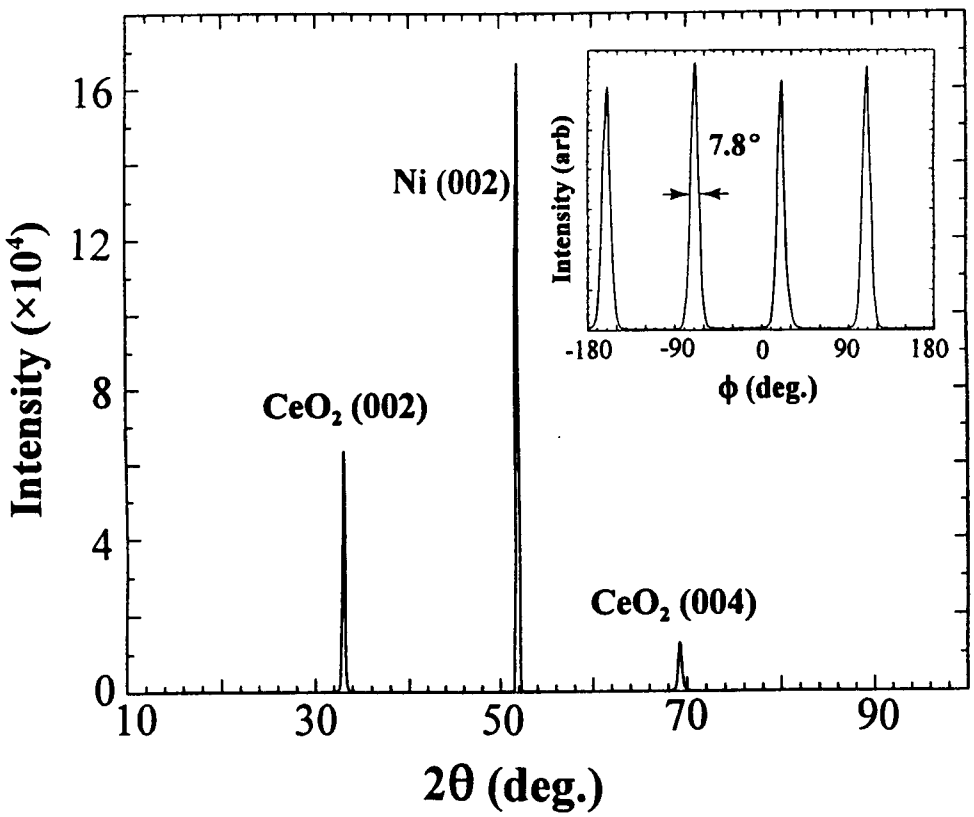


Figure 35 X-ray θ-2θ scan for the CeO_2 film directly deposited on the Ni substrate by using forming gas as a sputtering gas. The inset shows an x-ray ϕ-scan through the CeO_2 (202) reflection with FWHM of 7.8°.

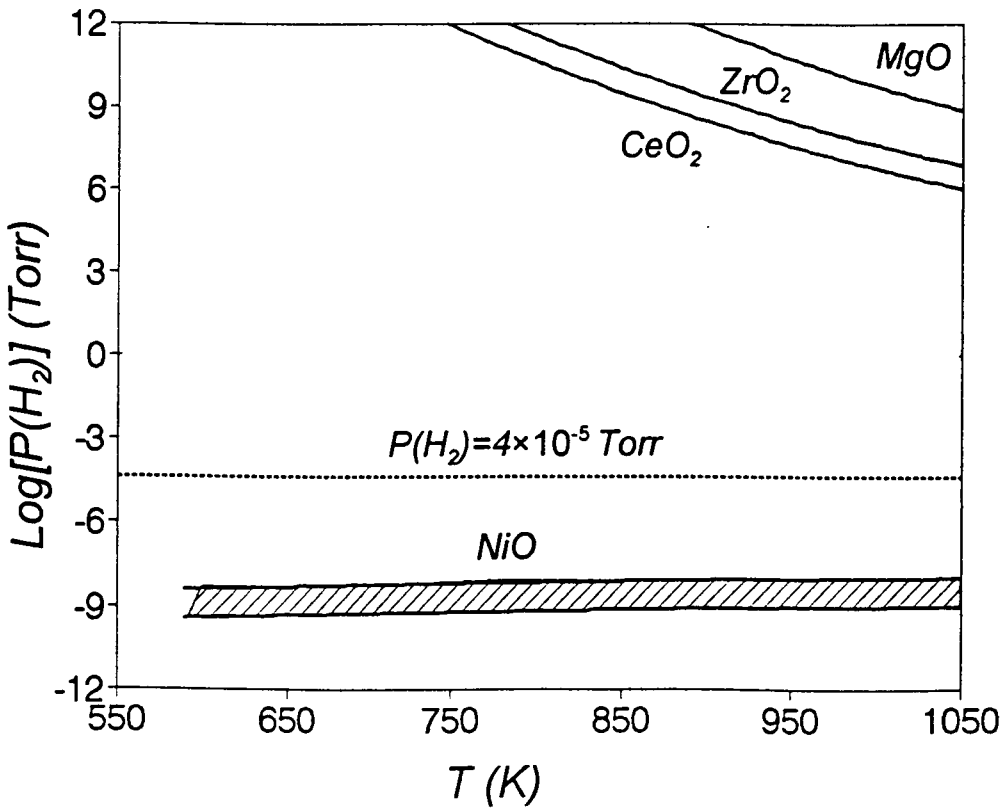


Figure 36 Stability of several metal oxides as a function of temperature and hydrogen partial pressure $P(H_2)$.

instability of NiO formation, but is insufficient to decompose CeO_2. In general, the deposition of stable oxides onto reactive metal surfaces may be facilitated by this process, provided the relative stabilities of the deposited and metal oxides are sufficiently diverse. In Figure 36, we have plotted the stability lines for some pertinent oxides, for a range of temperatures and hydrogen partial pressures of interest. These curves are calculated based on published free energies, [86] and the assumption of a background partial pressure of water vapor that is characteristic of the sputtering-system base pressure, i.e., $P(H_2O) \approx 10^{-7}$ - 10^{-6} Torr. For the sputtering/forming gas pressure used (1 mTorr), the H_2 partial pressure is 4×10^{-5} Torr, as illustrated in Figure 36. Over the entire deposition temperature range, this pressure assures stability of the sputtered oxides, e.g., CeO_2, ZrO_2, or MgO, while it lies several orders of magnitude above the minimum $P(H_2)$ values that would decompose, or prevent the formation of, NiO.

To study the effects of the deposition temperature and the sputtering ambient on the orientation of the CeO_2 film, epitaxial CeO_2 films have been deposited on the single crystal YSZ (001) substrates at various temperatures (500°C, 600°C, 700°C, and 800°C) and in two different sputtering ambient of Ar+10%O_2 and Ar+4%H_2. The deposition time, power, gas pressure, and growth rate for all the films were 1 hour, 66 W, 1×10^{-2} mbar, and ~0.2 Å/sec, respectively. X-ray θ-2θ diffraction shows every CeO_2 film possesses *c*-axis orientation. Figure 37 indicates that the FWHM value of the CeO_2 (002) rocking curve depends on the deposition temperature for both ambients. As the temperature increases for both sputtering ambients, the orientation of the CeO_2 film improves. This may be explained by structure zone model proposed by Movechan *et al.*[87] and J. A. Thornton.[88] The film structure depends

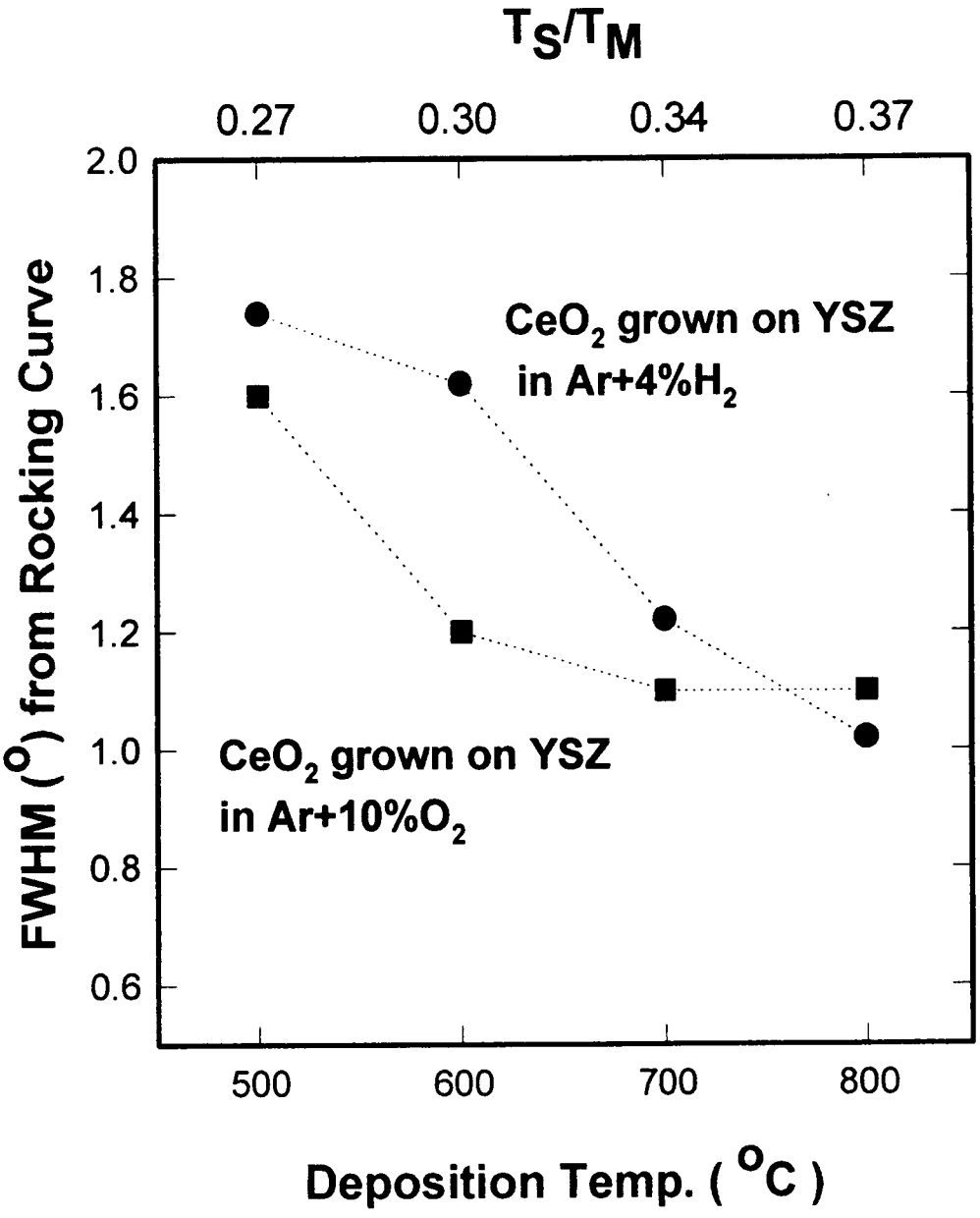


Figure 37 Deposition temperature dependance of the FWHM from CeO_2 (002) rocking curve for the CeO_2 films deposited on YSZ (001) single crystals in Ar+4%H_2 and in Ar+10%O_2, respectively.

strongly on the homologous temperature T_S/T_M, a ratio of the substrate temperature and the melting temperature. If $T_S/T_M < 0.3$ (zone 1), there is no significant diffusion during deposition. Within the range $0.3 < T_S/T_M < 0.5$ (zone 2), surface diffusion occurs during deposition. As $T_S/T_M > 0.5$ (zone 3), bulk diffusion occurs during deposition. From the Figure 37, we found that as the T_S/T_M value is above 0.3, the FWHM value decreases greatly. The improvement of the structural orientation may be related with the surface diffusion in the zone 2, where the atoms on the surface are mobile during the deposition. Therefore, a high substrate temperature enhances the epitaxial process by allowing sufficient surface diffusion of adatomes into equilibrium sites. Comparing the two curves, it is also found that better oriented CeO_2 films deposited in the Ar+10%O_2 ambient can be obtained at lower temperature than those in the Ar + 4%H_2 ambient. From the Rutherford Backscattering Spectrometry (RBS) analysis for each film, it is also found that the films grown in oxygen ambient are thicker than those grown in forming gas ambient, which means that the growth rate in the oxygen ambient is slightly higher than that in forming gas ambient. From the RBS analysis, it is also found that the CeO_2 films deposited in Ar-O_2 ambient have good channeling, indicating better crystallization, which is related to narrower rocking curve.

4.2.4 Conductive $LaNiO_3$ buffer layers

In contrast to the insulated buffer layer such as CeO_2, $SrTiO_3$, and YSZ, $LaNiO_3$ is a conductive buffer layer with electrical resistivity less than 1×10^{-3} Ωcm at room temperature, which is comparable to that of YBCO at room temperature and it has positive temperature dependence of resistivity.[89] Its pseudocubic lattice parameter "a" is 3.861Å which also

matches well with the lattice parameter of YBCO. It is very important to use a conductive buffer layer since it can electrically stabilize the conductor during transient loss of superconductivity.

Figure 38 shows the θ-2θ x-ray diffraction scan for the $LaNiO_3$ film on Ni substrates, which was grown at 400°C in forming gas. The only (00*l*) reflections for the $LaNiO_3$ indicate an excellent *c*-axis orientation. The inset shows a ω-scan through $LaNiO_3$ (200), revealing out-of-plane orientation of 5° FWHM. Figure 39 (a) shows the x-ray diffraction ϕ-scan through the $LaNiO_3$ (202) reflection with an FWHM value of 9.4°. Both the in-plane and out-of-plane alignments of the $LaNiO_3$ film are comparable to those of the (001) textured Ni tape.

To demonstrate the thermal stability of the $LaNiO_3$ at high temperature, the as-deposited $LaNiO_3$/Ni samples were post-annealed at 750°C and even at 850°C in 100 mTorr oxygen partial pressure for 1 hour. X-ray analyses show that the $LaNiO_3$ phase didn't decompose. In Figures 39 (a), (b), and (c), we found that the FWHM values of all the three samples are about 9-10°, which means that the high temperature annealing has little effect on the in-plane orientation of the $LaNiO_3$ film. Since the decomposition temperature for $LaNiO_3$ is 1120°C, where the $LaNiO_3$ will be decomposed into La_2NiO_4, NiO and O_2,[90] the $LaNiO_3$ phase is stable enough at the temperature of 750°C and 850°C. The chemical stability of $LaNiO_3$ film as a buffer layer is very important since it can ensure the growth of the YBCO films which are grown at 750°C in low oxygen atmosphere. The SEM observations indicate that the $LaNiO_3$ film is a very smooth and crack-free film, even after post-annealing at 850°C in oxygen, as shown in Figure 40. Unlike other buffer layers such as CeO_2 on Ni substrates, which are cracked during high temperature annealing, the $LaNiO_3$ is a crack-free buffer layer

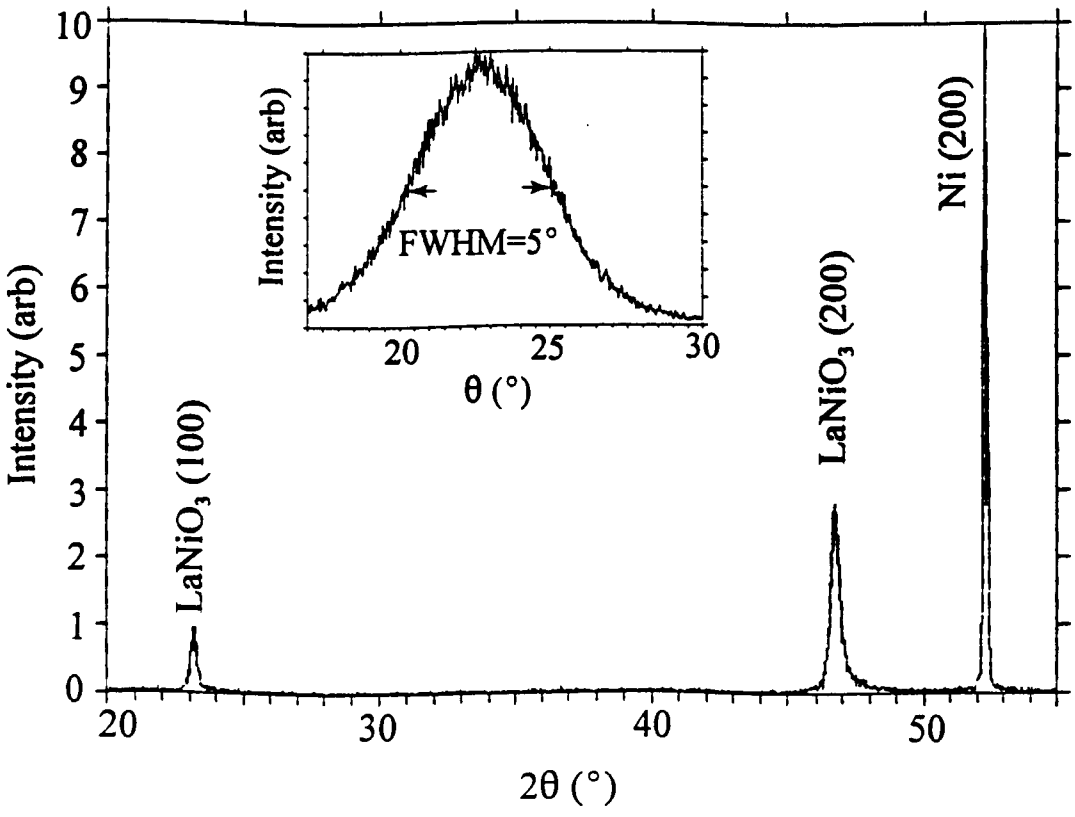


Figure 38 X-ray θ-2θ scan of $LaNiO_3$ laminate, indicating the presence of only (00*l*) peaks. The inset shows ω-scan through $LaNiO_3$ (200), revealing good out-of-plane orientation of 5° FWHM.

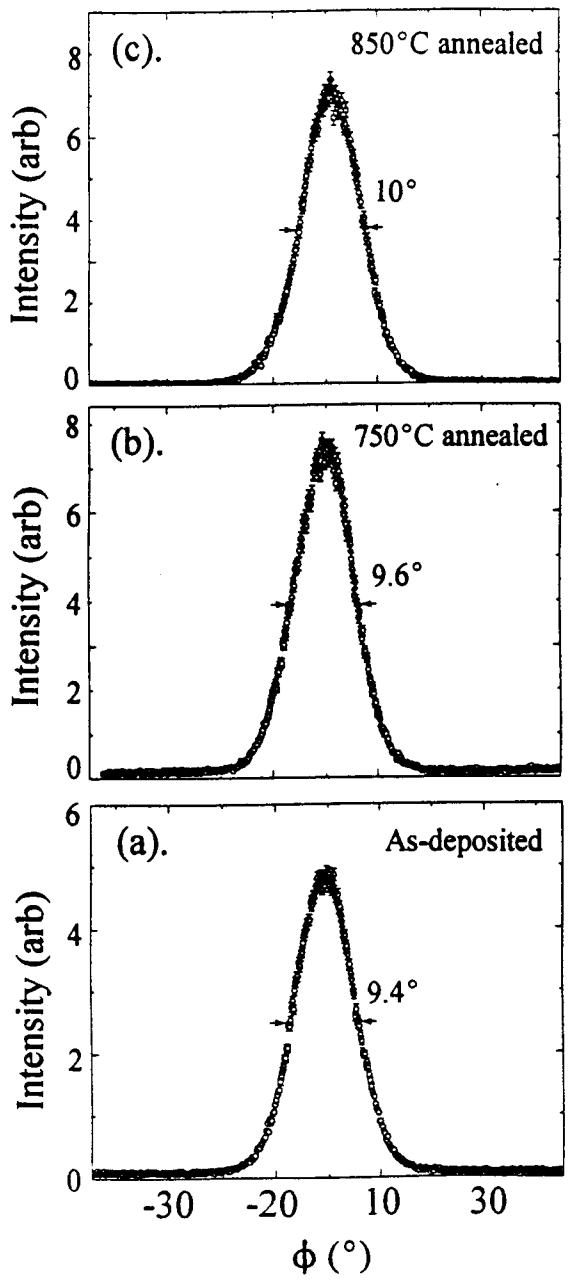


Figure 39 X-ray ϕ-scans through $LaNiO_3$ (202) for: (a). as-deposited $LaNiO_3$ film; (b). $LaNiO_3$/Ni sample post-annealed at 750°C in 100 m Torr oxygen pressure for 1 hour; and (c). $LaNiO_3$ sample post-annealed at 850°C in 100 m Torr oxygen pressure for 1 hour.

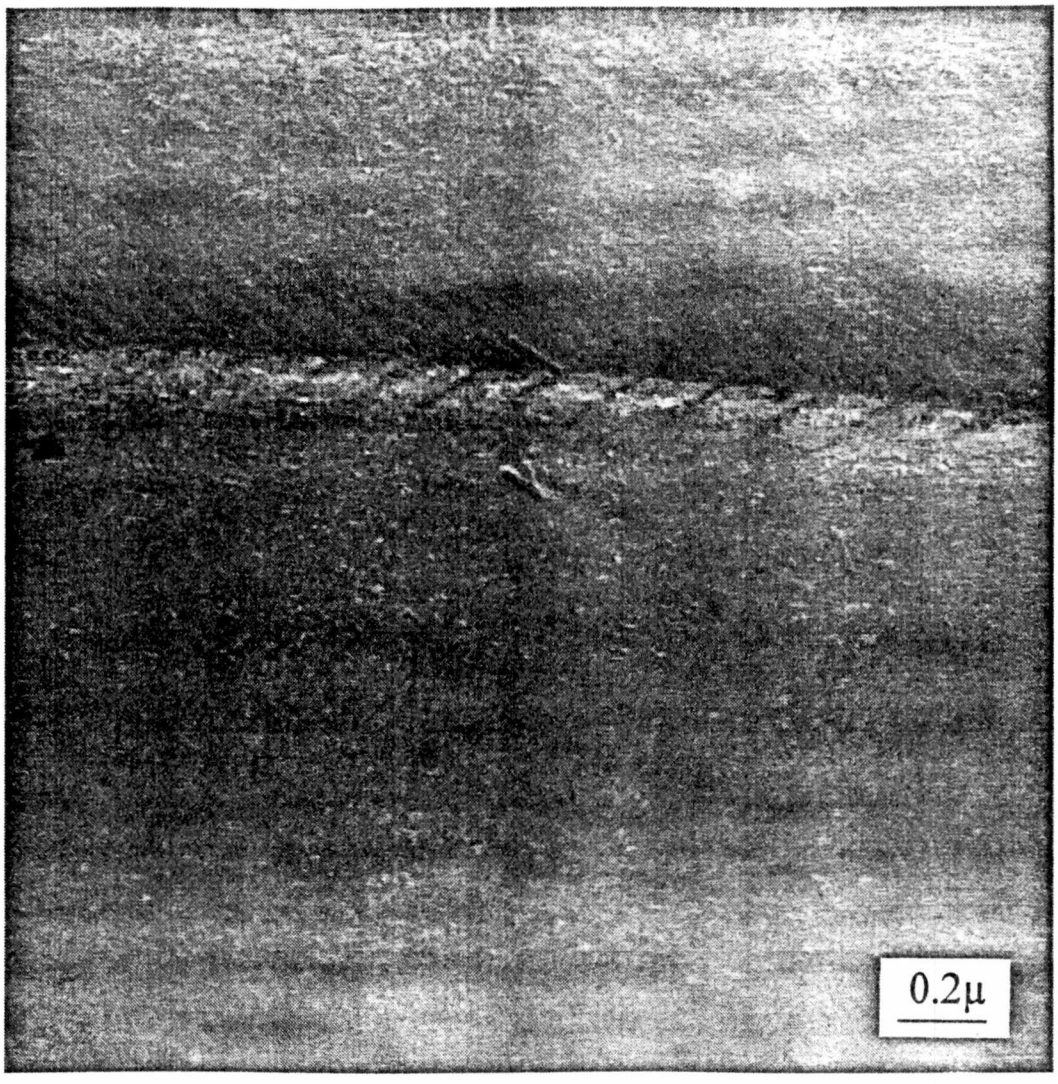


Figure 40 SEM micrograph of $LaNiO_3$ sample annealed at 850°C in 100 m Torr oxygen pressure for 1 hour, revealing smooth and crack-free surface.

when annealed at high temperature. The crack-free property for the film on the Ni substrate comes from the small difference of thermal expansion between $LaNiO_3$ and Ni. The average linear expansion coefficient β for $LaNiO_3$ and Ni are 12.5×10^{-6} $°C^{-1}$ and 13.3×10^{-6} $°C^{-1}$, respectively. The crack-free property for the buffer layer on the Ni substrate is crucial to prevent YBCO film from Ni contamination.

To study the property of the electrical resistivity, the (001) $LaNiO_3$ film was epitaxially deposited on a $SrTiO_3$ (001) single crystal substrate at about 400°C in pure Ar. Standard four probe technique was used to measure the resistance as a function of temperature (i.e., R-T curve). The as-deposited $LaNiO_3$ film on $SrTiO_3$ (001) was examined by XRD which shows both out-of-plane and in-plane orientations. The results of resistance vs. temperature for as-grown $LaNiO_3$ film and for the same film which was oxygen-annealed at 400°C, 500°C, 600°C, and 700°C, are shown in Figure 41. For the as-grown film, the resistance is high and the temperature coefficient of resistivity is negative, which indicates semi-conducting behavior. The high resistivity of the film may come from the concentration of impurities, such as Ar gas, which were trapped in the film during sputtering deposition. When the as-grown film was annealed in 1 atm oxygen at temperatures from 400°C to 700°C, the resistance goes down as the annealing temperature increases due to the decrease of the concentration of the impurities. It is also found that the temperature coefficient of resistivity is reversed from negative value for the as-grown film to positive value (i.e., metallic behavior) for the film annealed at 700°C in oxygen. Figure 42 shows the temperature dependence of the resistance for the as-grown $LaNiO_3$ film and the same film which was annealed at 400°C in different oxygen partial pressure, such as 35×10^{-6} atm, 0.02 atm, and

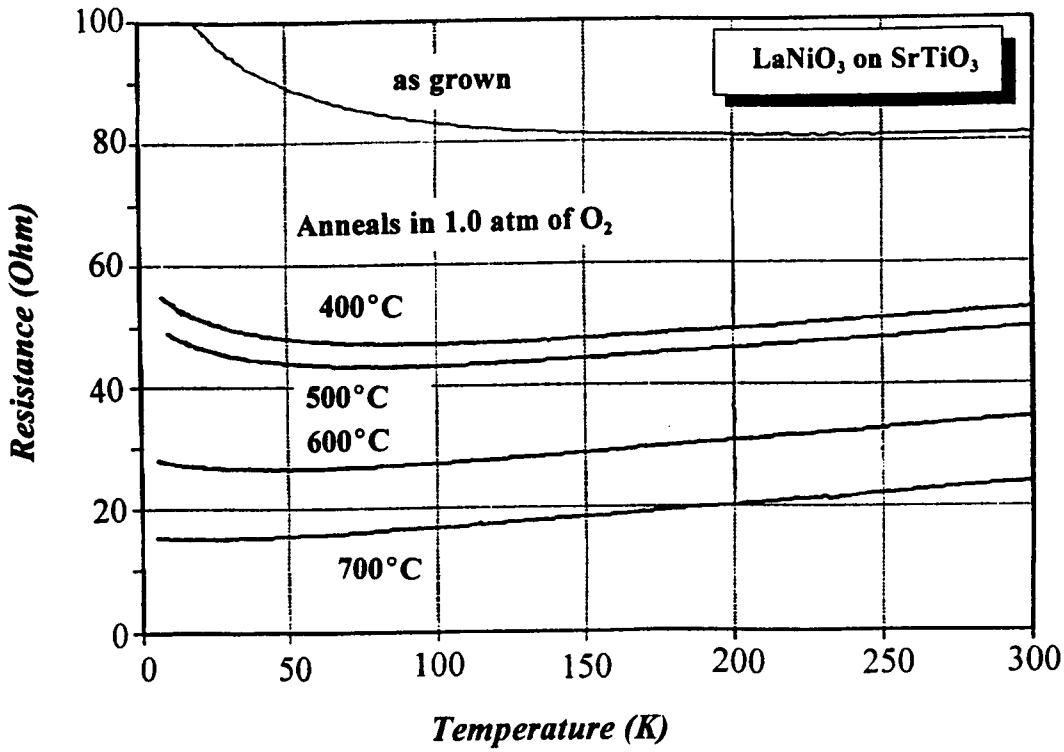


Figure 41 Temperature dependence of the resistance of $LaNiO_3$ (100) on $SrTiO_3$ single crystal substrate which was annealed at different temperature in 1 atm oxygen.

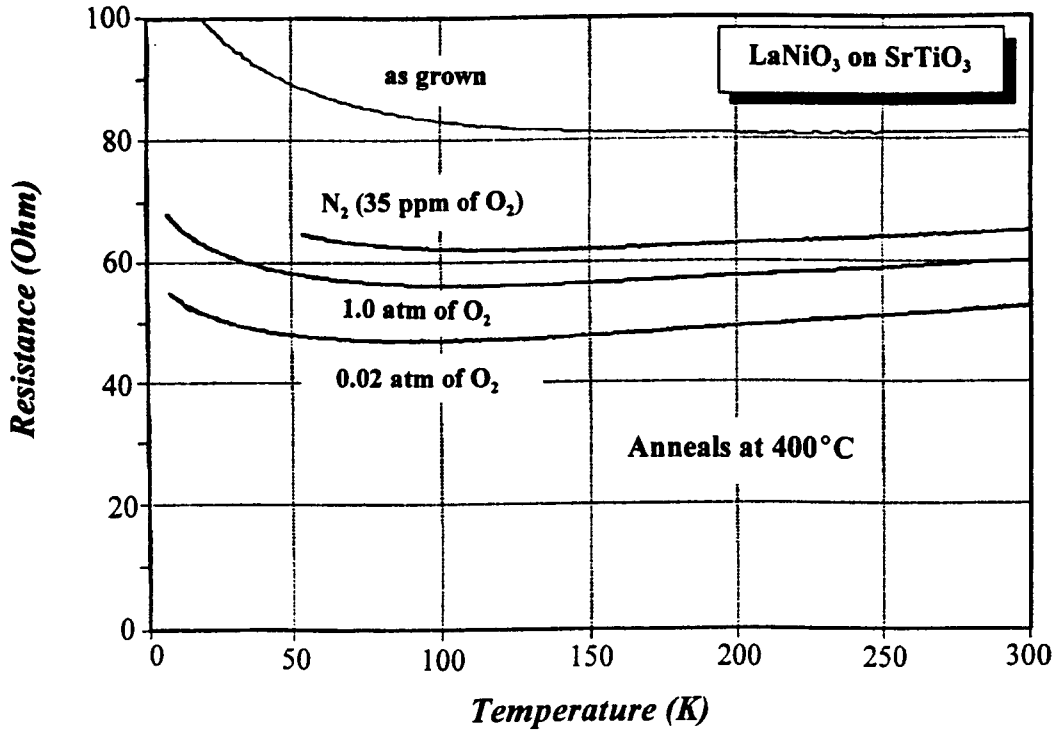


Figure 42 The temperature dependance of the resistance of $LaNiO_3$ (100) on $SrTiO_3$ single crystal substrate which was annealed at 400°C with different oxygen partial pressure.

1 atm. We can see that the resistance goes down as the film was annealed in oxygen ambient, and that the lowest resistance was gotten when annealed in 0.02 atm of O_2. From Figures 41 and 42, we found that the electrical resistance of the $LaNiO_3$ film mainly depends on its oxygen content and the impurity concentration. Because of the oxygen deficiency and high impurity concentration, the as-grown $LaNiO_3$ film, which were deposited in pure Ar, has high resistance with semiconducting behavior. The oxygen-annealing at high temperature for the $LaNiO_3$ film can reduce the electrical resistance greatly and can even change the temperature coefficient of resistivity from negative value (semiconducting behavior) to positive value (metallic behavior). Therefore, to get a conductive buffer layer with low resistivity, we have to anneal the $LaNiO_3$ films at high temperature in oxygen ambient.

4.2.5 YSZ buffer layer on the buffered Ni tapes

The appearance of the cracks on the CeO_2 films is of concern, since they could lead to Ni contamination of the YBCO films. Although two-step deposition technique for CeO_2 films seems to repair the cracks, a small amount of fine cracks can be still observed by SEM. To totally eliminate the cracks, an additional layer of YSZ has to be deposited on top of CeO_2/Pd buffered or CeO_2 buffered Ni tapes. By using forming gas as the sputtering ambient, the CeO_2 films were deposited directly on Ni tape at 400°C, followed by the deposition of a YSZ film at 780°C. X-ray θ-2θ scan of YSZ/CeO_2/Ni laminate is shown in Figure 43. All the strong reflections are indexed as (00*l*) reflections for both CeO_2 and YSZ, indicating strongly *c*-axis orientation. X-ray ω-scans and ϕ-scans for the YSZ films also exhibit good in-plane and out-of-plane orientations with FWHM values of 6°-9° similar to those of the CeO_2 films.

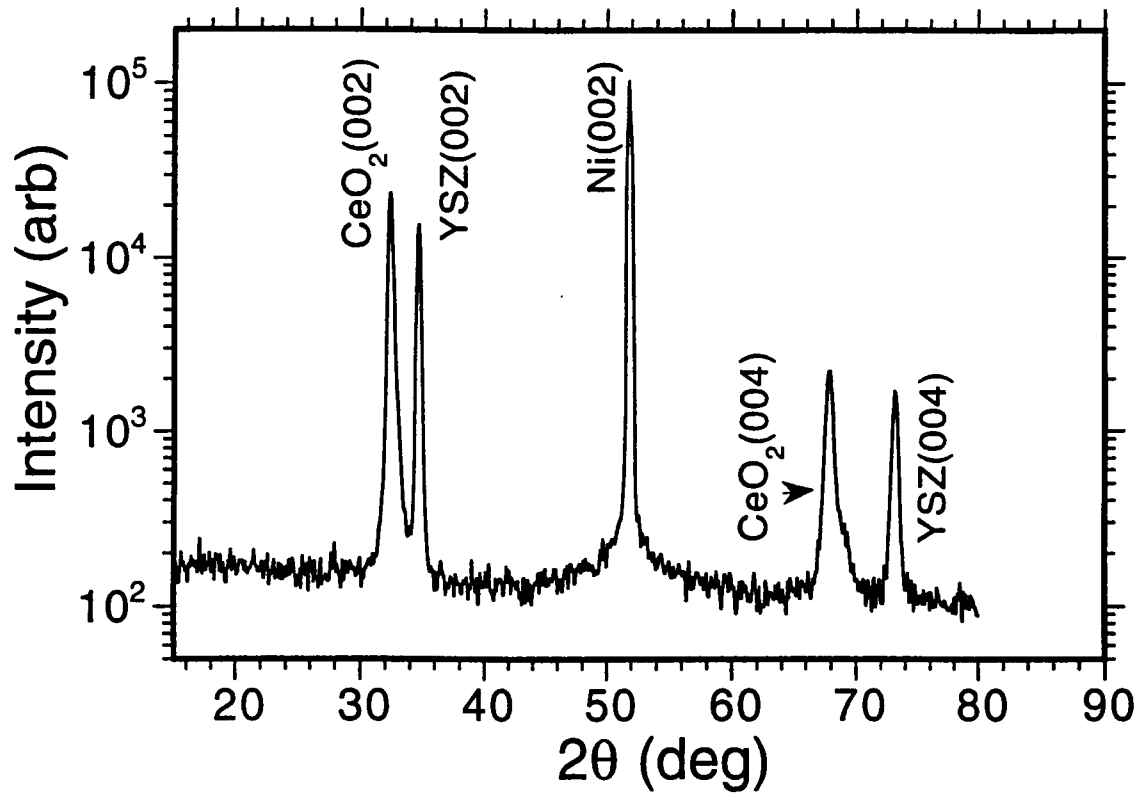


Figure 43 X-ray θ-2θ scan for the YSZ/CeO_2/Ni laminates, indicating the presence of only (00*l*) reflections for the CeO_2 and YSZ films. The YSZ was deposited at 780°C.

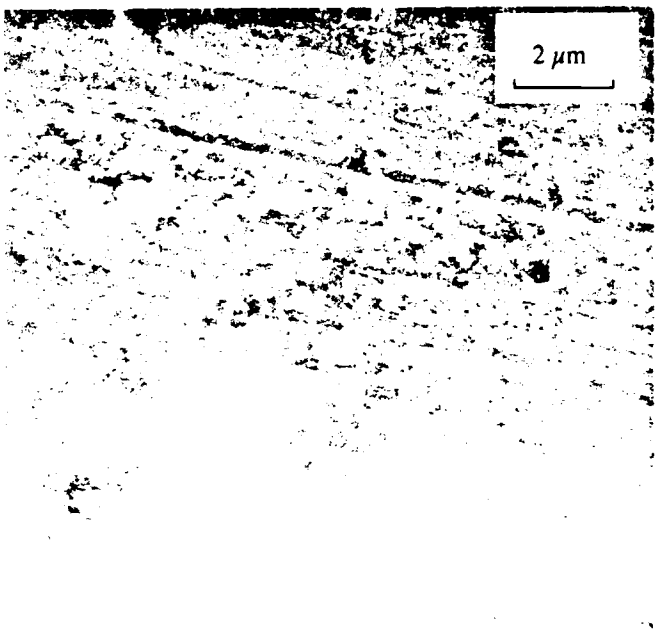


Figure 44 SEM micrograph showing the surface morphology of YSZ film on CeO_2/Pd-buffered Ni substrate, annealed at 750°C in O_2 partial pressure, revealing no cracks on the YSZ surface.

After oxygen-annealing at 750°C for one hour, the YSZ/CeO_2/Ni was observed by SEM. The observation reveals that there is no visible cracking on the YSZ surface, as shown in Figure 44, which means the deposition of YSZ is very effective to essentially eliminate the cracks of the buffer layers.

As an optional layer, an in-plane *c*-axis oriented YSZ layer can also be further deposited on $LaNiO_3$ buffered Ni tapes at 750°C in forming gas using r.f. sputtering. The x-ray diffraction spectra for the YSZ/$LaNiO_3$/Ni sample shown in Figure 45 indicate the YSZ film has good *c*-axis orientation. The FWHM value for the ω-scan is about 5°. The x-ray diffraction ϕ-scan through the YSZ (202) reflection in the inset picture reveals the in-plane orientation with FWHM value of 16° for the YSZ film.

4.2.6 The YBCO films on the buffered Ni tapes

The final objective of the RABiTS technique is to grow biaxially textured HTS films on the buffered Ni tapes. In initial studies, a pulsed laser ablation (PLD) technique was employed by D. P. Norton *et al.*[91] to grow the YBCO films on these buffered Ni substrates, such as Ag/Pd/Ni, CeO_2/Ag/Pd/Ni, YSZ/CeO_2/Pd/Ni, and YSZ/CeO_2/Ni. Figure 46 shows ϕ-scans for each layer of the YBCO films on some RABiTS substrates, which indicates the transference of texture from the biaxially textured Ni to the YBCO films. In the Figure 46 (a), the YBCO layer has been grown epitaxially on the Ag/Pd buffered Ni substrate. The *a*- and *b*- axes of YBCO are aligned in-plane with Ag⟨100⟩ and Ag⟨110⟩. This result is consistent with the previous work on the YBCO film grown on Ag single crystals.[92] The T_c value of the film is 84 K. The J_c value is only about 10^3 A/cm^2 at 77 K due to the presence of two epitaxial

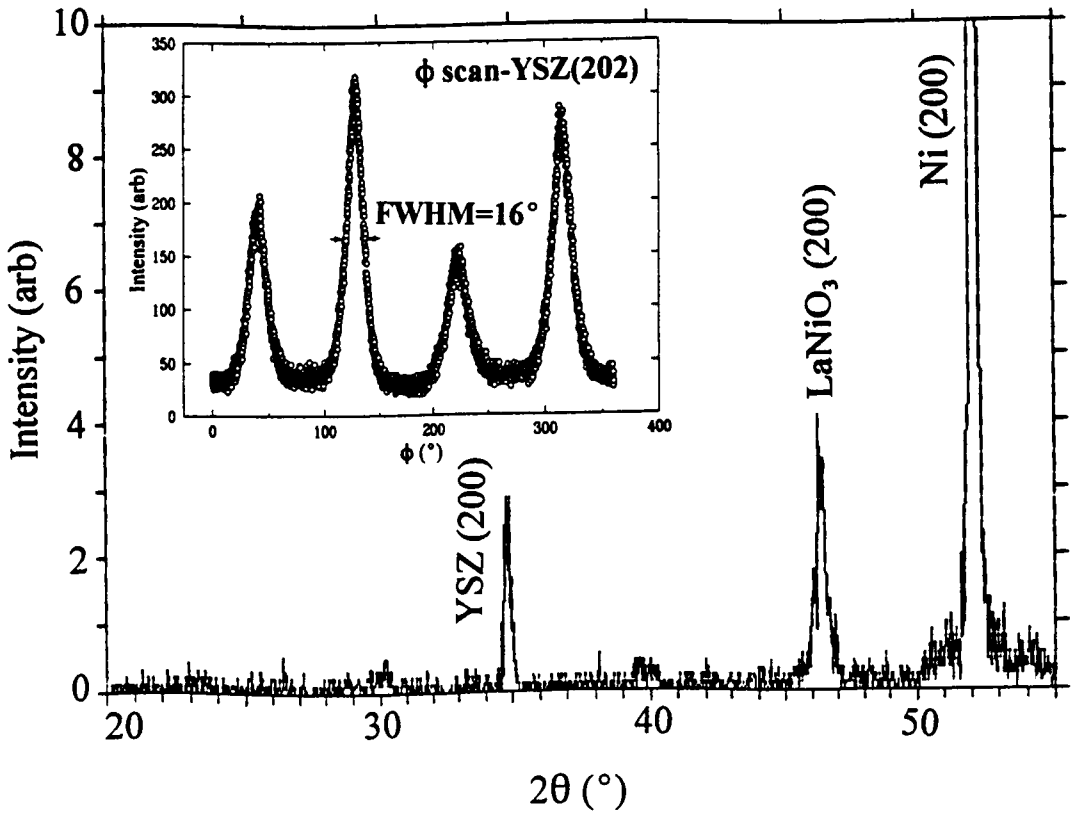


Figure 45 X-ray θ-2θ scan for YSZ/$LaNiO_3$/Ni laminate, showing *c*-axis orientation for each layer. The FWHM for the φ-scan through YSZ (202) is 16°.

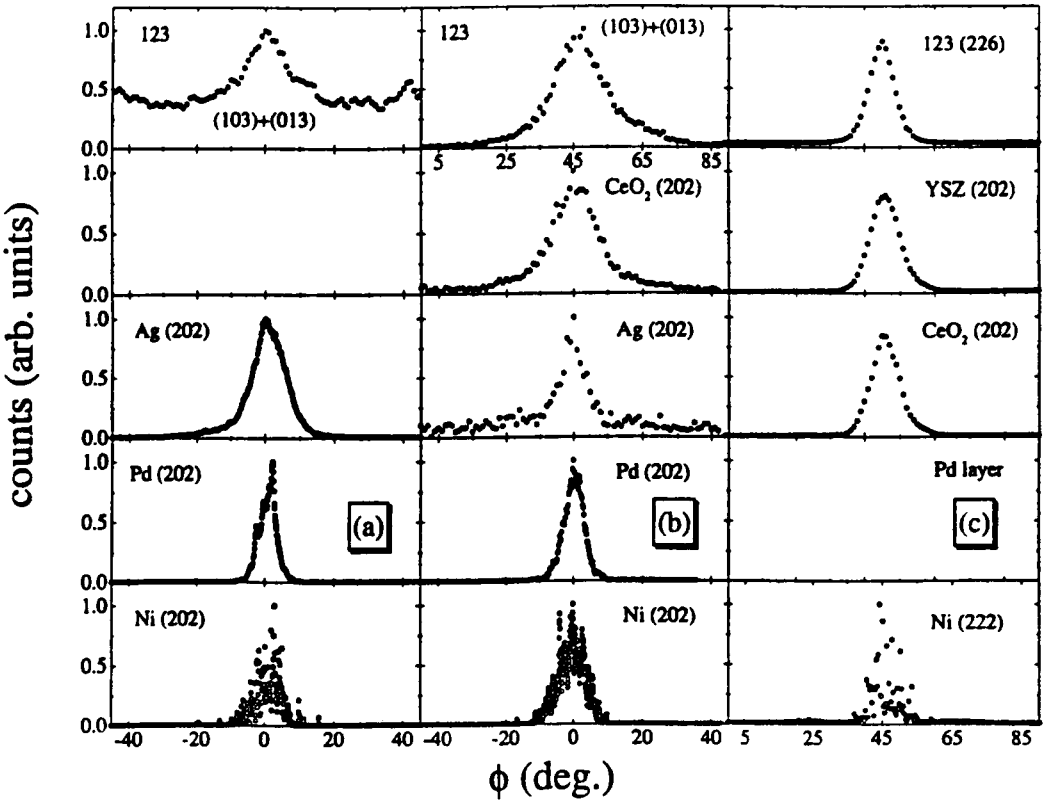


Figure 46 X-ray ϕ-scans showing the transference of texture through the various multilayer of RABiTS substrates: (a). YBCO/Ag/Pd/Ni; (b). YBCO/CeO_2/Ag/Pd/Ni; and (c). YBCO/YSZ/CeO_2/Pd/Ni.

orientations and some high angle boundaries in the YBCO films. Figure 46 (b) shows ϕ-scans of each layer for YBCO/CeO_2/Ag/Pd/Ni multilayer structure. Single epitaxial orientation of YBCO has been realized on the CeO_2 buffer layer. However, due to the high evaporation pressure of the Ag, some bubbles were formed on the surface of the YBCO films. The T_c is 87.5 K, but the J_c value is only 8×10^4 A/cm^2 at 77 K. Figure 46 (c) represents ϕ-scans of each layer for YBCO/YSZ/CeO_2/Pd/Ni multilayer structure. The epitaxial orientation of the YBCO is better than the first two laminates. The J_c value is up to 3×10^5 A/cm^2 at 77 K.

The best YBCO films were grown on the YSZ/CeO_2/Ni RABiTS substrates. Figure 47 shows a θ-2θ x-ray diffraction scan of the YBCO/YSZ/CeO_2/Ni laminate, indicating that each layer is (001)-oriented relative to the surface normal. In Figure 48 (a), the rocking curves for the Ni, CeO_2, YSZ, and YBCO layers indicate an out-of-plane FWHM of 6.3°, 5.5°, 5°, and 1°, respectively. A significant narrowing in the out-of-plane texture was observed for the YBCO. This improvement in the out-of-plane alignment relative to the underlying Ni results from the low (001) surface energy and the anisotropic film growth nature commonly observed for YBCO.[93] This high degree of out-of-plane texture is important in realizing a high J_c value, as it virtually eliminates the [100] tilt boundary contribution to the total misorientation angle of the grain boundaries. The in-plane crystallographic alignment of the epitaxial YBCO/YSZ/CeO_2/Ni structure, as determined by XRD ϕ-scans through the YBCO (226), YSZ (202), CeO_2 (202), and Ni (222), is also shown in Figure 48 (b). The in-plane FWHM for all of the layers is in the range of 5-7°, indicating excellent epitaxy of the oxide layers with the biaxially textured metal. The in-plane CeO_2 (100) and YSZ principal crystallographic axes are rotated 45° relative to the in-plane Ni (100) axis, whereas the *a*- and

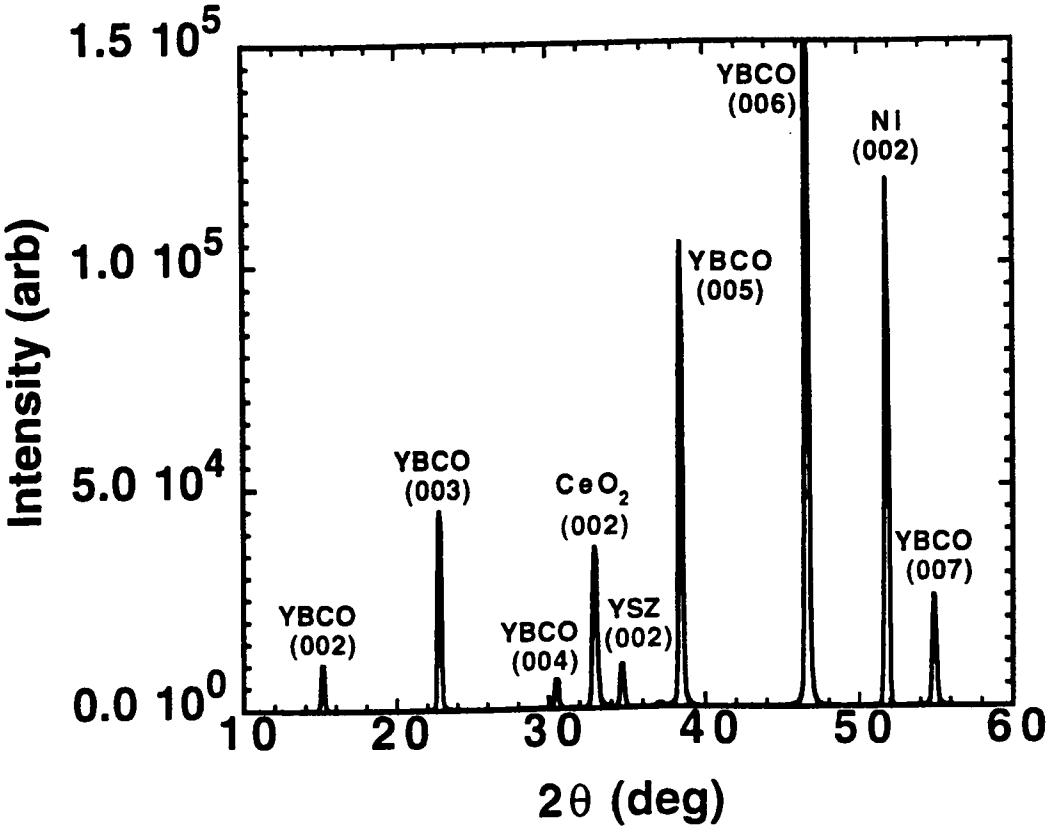


Figure 47 An x-ray θ-2θ scan for a YBCO/YSZ/CeO_2/Ni multilayer structure, showing good *c*-axis orientation for each layer.

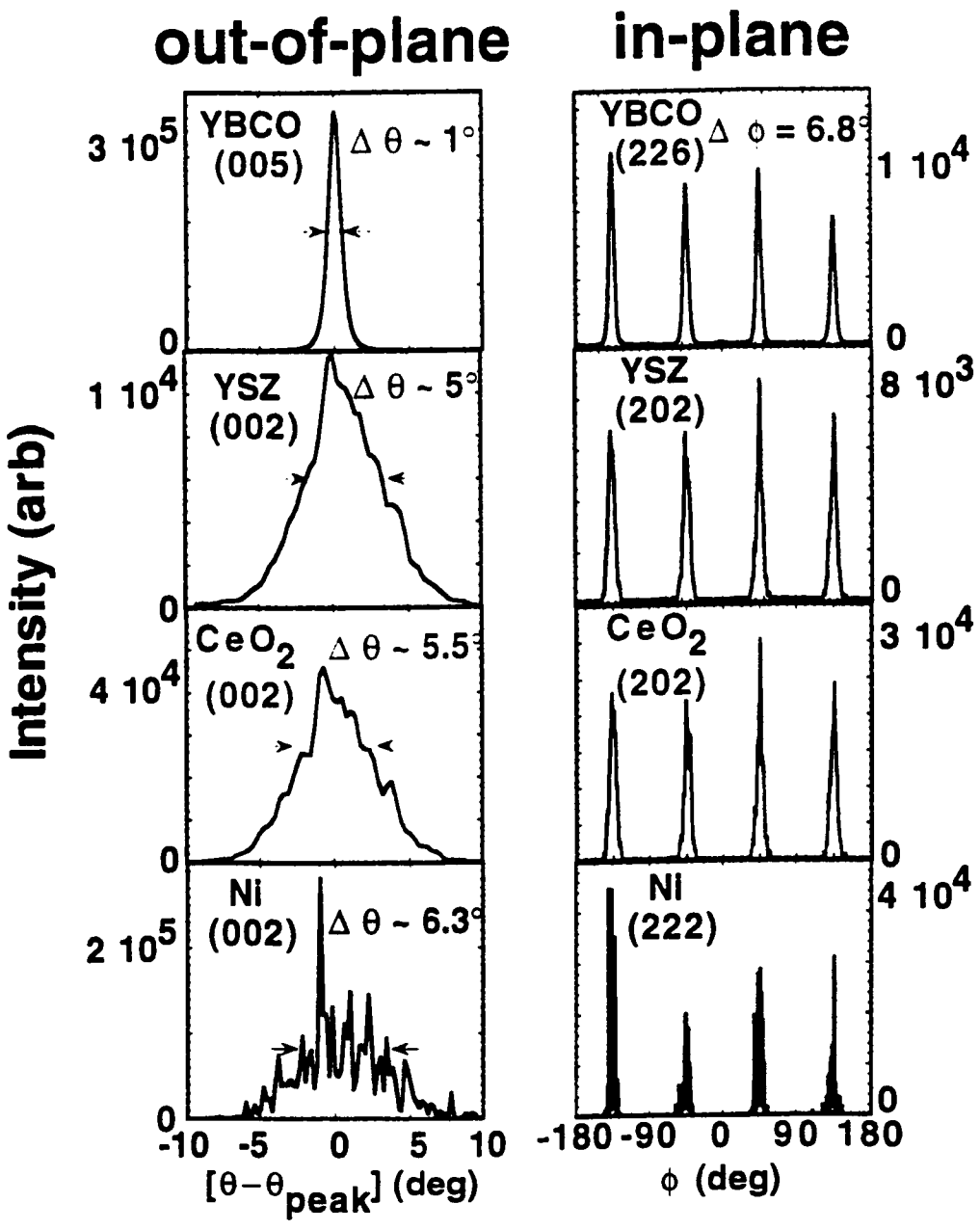


Figure 48 X-ray rocking curves and φ-scans for YBCO/YSZ/CeO_2/Ni laminate showing the out-of-plane and in-plane orientations for each layer.

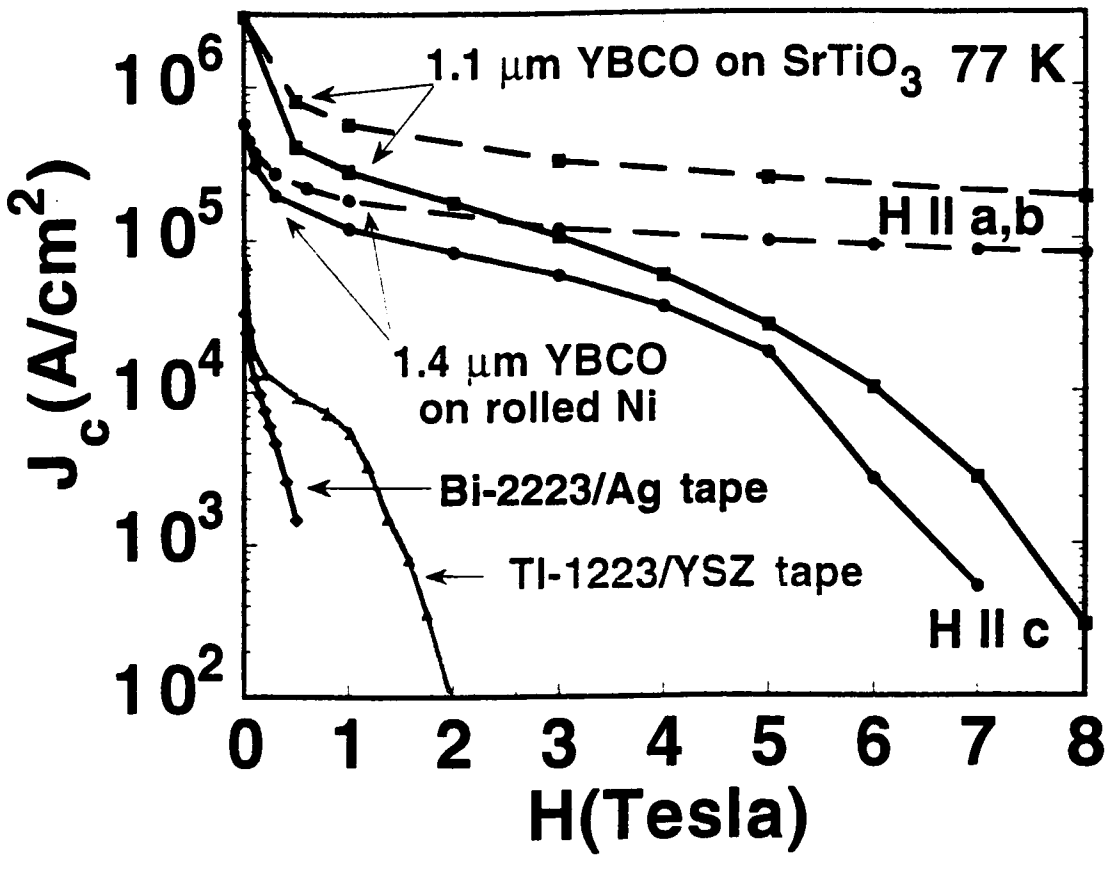


Figure 49 Magnetic field dependence of J_c value at 77 K for a YBCO/YSZ/CeO_2/Ni laminate, YBCO/$SrTiO_3$ (001), Tl-1223/YSZ (polycrystalline), and Bi-2223/Ag tape.

b- axes of the YBCO are rotated 45° with respect to the YSZ axes.

The magnetic field dependence of J_c at 77 K for a 1.4-μm-thick YBCO film deposited on a YSZ/CeO_2/Ni RABiTS tape is shown in Figure 49 with magnetic field, H, applied parallel and perpendicular to the *c*- axis. At zero field, this YBCO film has a J_c (77 K, H=0) of 5.75×10^5 A/cm^2. Recently, the YBCO films with the highest J_c (77 K, H=0) value of 2×10^6 A/cm^2 has been grown on the CeO_2/YSZ/CeO_2/Ni RABiTS substrate, which is comparable to the epitaxial YBCO films grown on $SrTiO_3$ (001). The magnetic field dependence of J_c for the film on rolled-textured Ni is similar to that measured for the epitaxial YBCO film on $SrTiO_3$. In fact, the relative drop of J_c with applied external magnetic field is less for the YBCO film grown on the Ni tape than for the film on $SrTiO_3$ (001), indicating the presence of additional flux-pinning defects in the films grown on the rolled-textured Ni. These pinning sites may be associated with growth-induced defect structures[94] or low-angle grain boundary pinning, or both.[95, 96] The J_c (77 K, H) behavior for Bi-2223/Ag[97] and Tl-1223/YSZ[98] tapes are also shown for comparison.

Figure 50 indicates the temperature dependence of J_c, measured in magnetic fields of 0, 3, and 8 T applied parallel to the c axis for the YBCO/YSZ/CeO_2/Ni laminate. The J_c (T) behavior for the YBCO films on the RABiTS substrates is comparable with that observed for the epitaxial YBCO films on oxide single crystals, which is consistent with the absence of high-angle grain boundaries in the YBCO film. For comparison, we also present data for conventional low-T_c superconducting NbTi and Nb_3Sn wires as well for Bi-2212/Ag, Bi2223/Ag, and Tl-1223/poly-YSZ HTS wires and tapes. The J_c (77 K, H=0) value of the YBCO on RABiTS substrates is significantly higher than the J_c (4.2 K, H=0) of Bi-2223,

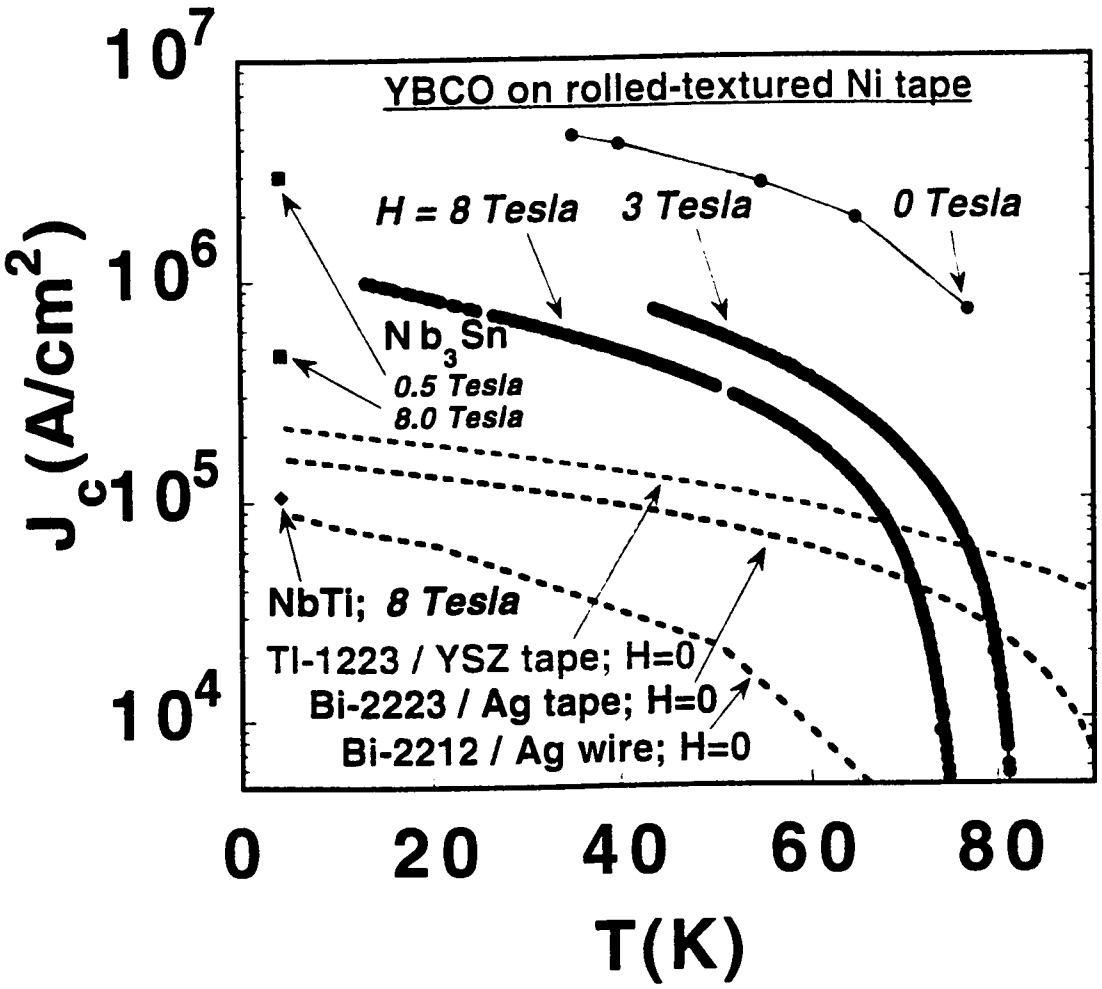


Figure 50 The temperature dependence of J_c value, measured at 0, 3, and 8 T, for a YBCO/YSZ/CeO_2/Ni laminate. For comparison, data are also shown for Bi-2212/Ag wire, Bi-2223/Ag tape, Tl-1223/YSZ (polycrystalline), NbTi, and Nb_3Sn.

Bi-2212, or Tl-1223 wires and tapes at 4.2 K. Moreover, for temperature less than 70 K, J_c (T, H=8T) for the YBCO/RABiTS is higher than J_c (T, H=0) for the Bi-2223/Ag and Tl-1223/YSZ wires.

5. CONCLUSIONS

C-axis oriented thick $Tl_1Ba_2Ca_2Cu_3O_9$ (Tl-1223) films with high J_c value of 4.7×10^4 A/cm^2 at 77 K have been deposited on polycrystalline Ag substrate by spin-coating method. The properties of the Tl-1223 films are not only controlled by the Tl source temperature, reaction time, and sample temperature during the Tl-treatment, but also strongly influenced by the pressing process before the Tl-treatment.

Biaxially textured YBCO films with high J_c values over 10^6 A/cm^2 at 77 K have been grown on the buffered flexible Ni tapes by RABiTS process. In the RABiTS process, the deposition of buffer layers on the aligned Ni substrates plays an important role, which should ensure epitaxy and chemical compatibility of the buffer layers with both the underlying Ni and the final YBCO layer. Two approaches have been developed to grow the buffer layers. The first is to grow biaxially oriented metal or oxide buffer layers, such as Ag and CeO_2, on the Ni tapes by using oxidation-resistant Pd (or Pt) film as an intermediate layer, which transfers the biaxially oriented structure from Ni to the top buffer layers. The second approach is to grow biaxially oriented oxide films, such as CeO_2 and $LaNiO_3$, directly on the Ni substrate by introducing forming gas (Ar/4%H_2) which could prevent the formation of NiO and assure stability of the sputtered oxides. It is found that some biaxially textured films, such as Pd and CeO_2, can be grown at room temperature and that post-annealing can improve the biaxial orientations. The effects of the deposition temperature on the degree of biaxial orientations of the CeO_2 films were investigated. SEM observations show that cracking may occur on the

CeO_2 buffer layer when oxygen-annealing at high temperature. To prevent the cracking, an additional YSZ layer was deposited on the CeO_2 buffered Ni substrates. It is found that the smooth Ni surface can improve the out-of-plane orientation of the deposited films. Conductive buffer layer $LaNiO_3$ with biaxial orientations has also been grown on the textured Ni. Oxygen anneals at 850°C for the $LaNiO_3$ film on Ni neither change the biaxial orientations of the film significantly nor cause any cracks on the surface of the films. The resistivity of the $LaNiO_3$ films can be reduced by oxygen-annealing at high temperature.

REFERENCES

1. G. J. Bednorz and L. A. Muller, Zeitschrift fur Phys. B **64**, 189-93 (1996).

2. M. K. Wu, J. R. Ashbum, C. J. Torng, P. H. Hor, R. L. Meng, L. Gao, Z. J. Huang, Y. Q. Wang, and C. W. Chu, Phys. Rev. Lett. **58**, 908 (1987).

3. C. W. Chu, P. H. Hor, R. L. Meng, L. Gao, Z. J. Huang, Y. Q. Wang, J. Bechtold, D. Campbell, M. K. Wu, J. Ashburn, and C. Y. Huang, Phys. Rev. Lett., **58**, 405 (1987).

4. H. Maeda, Y. Tanaka, M. Fukutomi, and T. Asano, Jpn. J. Appl. Phys. Lett. **27**, 209 (1988).

5. Z. Z. Sheng and A. M. Hermann, Nature **332**, 138 (1988).

6. S. N. Putilin, et al, Nature, **362**, 226 (1993).

7. A. Schilling, et al, Nature **363**, 56 (1993).

8. C. W. Chu, Y. Y. Xue, Z. L. Du, Y. Y. Sun, L. Gao, N. L. Wu, Y. Cao, I. Rusakova, K. Ross, Science, **277**, 1081 (1997).

9. J. R. Thompson, J. G. Ossandon, D. K. Christen, M. Paranthaman, E. D. Specht, and Y. C. Kim, Phys. Rev. B, **54** (10), 1-7 (1996).

10. T. P. Orlando, *et al.*, Phys. Rev. B **19**, 4545 (1979).

11. L. D. Cooley, *et al.*, Appl. Phys. Lett. **58**, 2984 (1991).

12. J. G. Ossandon, *et al.*, Phys. Rev. B **45**, 12534 (1992).

13. J. R. Thompson, *et al.*, Physica B **165**, 1453 (1991).

14. J. R. Thompson, *et al.*, Phys. Rev. B **41**, 7293 (1990).

15. J. R. Thompson, J. G. Ossandon, D. K. Christen, B. C. Chakoumakos, Y. R. Sun, M. Paranthaman, and J. Brynestad, Phys. Rev. B **48** (18), 14031(1993).

16. L. Krusin-elbaum, C. C. Tsuel and A. Gupta, Nature, **373**, 679(1995).

17. Gun Cheol Kim, Young Gheol Kim, Physica C **259** 218-221 (1996).

18. Shen Zhu's Ph.D. dissertation, University of Tennessee, Knoxville, pp3, (1993).

19. Gerald Burns, High-temperature Superconductivity, An Introduction, Academic Press, Inc., 168 (1992).

20. Hongtao Ren, Qing He, Ling Xiao, Wang Ruikun, Dingan Yu, Cui Changgeng, and Li Shanlin, Cryogenics **30**, S837 (1990).

21. K. Sato, T. Hikata, H. Mukai, M. Ueyama, N. Shibata, T. Kato, T. Masuda, M. Nagata, K. Iwata, and T. Mitsui, IEEE Trans. Mag. **27**, 1231 (1991).

22. L. P. Guo, Z. F. Ren, J. Y. Lao, J. H. Wang, D. K. Christen, C. E. Klabunde, J. D. Budai, Physica C **277,** 13-18 (1997).

23. K. J. Song, J. R. Thompson, *et al*, unpublished.

24. L. Krusin-Elbaum, C. C. Tsuel and A. Gupta, Nature, **373**, 679-681, 23 February 1995.

25. K. A. Muller, M. Takashige and J. G. Bednorz, Phys. Rev. Lett. **58**, 408 (1987).

26. Y. Yeshurunand A. P. Molozemoff, Phys. Rev. Lett. **60**, 2202 (1988).

27. M. Tuominen, A. M. Goldman, and M. L. Mecartney, Phys. Rev. B **37**, 548 (1988).

28. A. C. Mota, A. Pollini, P. Visani, K. A. Muller and J. G. Bednortz, Phys. Rev. B **36**, 829 (1987).

29. S. S. P. Parkin, V. Y. Lee, A. I. Nazzal, R. Savoy, R. Beyers, and S. J. La Placa, Phys. Rev. Lett. **61,** 750 (1988).

30. M. A. Subramanian, J. B. Parise, J. C. Calabrese, C. C. Torardi, J. Gopalakrishnan, and A. W. Sleight, J. Solid State Chem. 77 192 (1990).

31. H. Ihara, R. Sugise, M. Hirabayashi, N. Terada, M. Jo, K. Hayashi, A. Negishi, M. Tokumoto, Y. Kimura, and T. Shimonura, Nature **334**, 510 (1988).

32. R. Sugise, M. Hirabayashi, N. Terada, M. Jo, T. Shimomura, and H. Ihara, Physica C **157,** 131 (1989).

33. C. C. Torardi, M. A. Subramanian, J. C. Calabrese, J. Gopalakrishnan, K. J. Morrisey, T. R. Askew, R. B. Flippen, U. Chowdry, Science **240**, 631 (1988).

34. T. Zetterer, H. H. Otto, G. Lugert, and K. F. Renk, Z. Phys. B **73**, 321 (1988).

35. S. S. Parkin, V. Y. Lee, A. I. Nazzal, R. Savoy, T. C. Huang, G. Gorman, and R. Beyers, Phys. Rev. B **38**, 6531(1988).

36. R. Sugize and H. Ihara, Jpn. J. Appl. Phys. **28**, 334 (1989).

37. D. H. Kim, K. E, Gray, R. T. Kampwirth, J. C. Smith, D. S. Richeson, T. J. Marks, J. H. Kang, J. Talvacchio, and M. Eddy, Physica C **177**, 431 (1991).

38. Takeshi Hikata, Ken-ichi Sato, and Yukikazu Iwasa, Physica C, **185-189**, 2363-2364 (1991).

39. J. E. Tkaczyk, J. A. DeLuca, P. L. Kara, P. J. Bednarczyk, M. F. Garbauskas, R. H. Arendt, and K. W. Lay, and J. S. Moodera, Appl. Phys. Lett. **61** (5), 610 (1992).

40. D. N. Zheng, A. M. Campbell, R. S. Liu and P. P. Edwards, Cryogenics **33** (1), 46 (1993).

41. D. H. Kim *et al.*, Physica C, **177**, 431-437 (1991).

42. L. Krusin-Elbaum *et al.*, Appl. Phys. Lett., **64**, 3331-3333 (1994).

43. J. E. Tkaczyk *et al.*, appl. Phys. Lett., **62**, 3031-3033 (1993).

44. Z. F. Ren, M. Qi, and J. H. Wang, Physica C **184**, 24 (1991).

45. Z. F. Ren and J. H. Wang, Appl. Phys. Lett. **61** (14), 1715 (1992).

46. J. A. DeLuca, M. F. Garbauskas, R. B. Bolon, J. G. McMullen, W. E. Balz, and L. Kara, J. Mater. Res. **6**, 1415 (1991).

47. J. A. DeLuca, P. L. Kara, J. E. Thaczyk, P. J. Bednarczyk, M. F .Garbauskas, C. L. Briant and D.B. Sorensen. Physica C **205**, 21 (1993).

48. J. A. DeLuca, P. L. Kara, J. E. Tkaczyk, P. J. Bednarczyk, M. G. Garbauskas, C. L. Briant and D. B. Sorensen, Physica C **205**, 21 (1993).

49. Toshiya J. Doi, Toyotaka Yuasa, Takeshi Ozawa, and Kazutoshi Higashiyama, Jpn. J. Appl. Phys. **33**, 5692 (1994).

50. W. Y. Lee, S. M. Garrison, M. Kawasaki, E. L. Venturini, B. T. Ahn, and R. Byers, Appl. Phys. Lett., **60**, 772 (1992).

51. D. S. Ginley, J. F. Kwak, R. P. Hellmer, R. J. Baughman, E. L. Venturini and B. Morosin, Appl. Phys. Lett. **53**, 406 (1988).

52. K. Endo, Y. Moriyasu, S. Misawa, and S. Yoshida, Physica C **185-189**, 1995 (1991).

53. T. Nabatame, Y. Saito, T. Kamo, and S. Matsuda, Jpn. J. Appl. Phys. **29**, L1813 (1990).

54. Z. F. Ren, C. A. Wang, and J. H. Wang, Appl. Phys. Lett. **65** (2), 237 (1994).

55. J. E. Tkaczyk, JOM **46**, 26 (1994).

56. D. Dimos, P. Chaudhari, J. Mannhart, and F. K. K. LeGoues, Phys. Rev. Lett., **61**, 219 (1988).

57. D. Dimos, P. Chaudhari, and J. Mannhart, Phys. Rev. B **41**, 4038 (1990).

58. A. H. Cardona *et al.*, Appl. Phys. Lett., **62** (4), 411 (1993).

59. M. Kawasaki *et al.*, Appl. Phys. Lett., **62** (4), 17 (1993).

60. T. Nabatame *et al.*, Appl. Phys. Lett., **65** (6), 776 (1994).

61. A. Goyal, E. D. Specht, and T. A. Mason, Appl. Phys. Lett., **68**, 711 (1996).

62. A. Goyal, E. D. Specht, D. K. Christen, D. M. Kroeger, A. Pashitski, A. Polyanskii, and D. C. Larbalestier, JOM, **48**, 24 (1996).

63. Q. Li, X. X. Xi, X. D. Wu, et al. , Phys. Rev. Lett. **64**, 3086-3089 (1990).

64. D. H. Lowndes, D. P. Norton, and J. D. Budai, Phys. Rev. Lett. **65**, 1160-1163 (1990).

65. K. Heine, J. Tenbrink and M. Thoner, Appl. Phys. Lett. **55**, 2441 (1989).

66. X. D. Wu, S. R. Foltyn, P. Arendt, J. Townsend, C. Adams, I. H. Campbell, P. Tivari, Y. Coulter, and D. E. Peterson, Appl. Phys. Lett. **65**, 1961 (1994).

67. R. Chatterjee, S. Aoki, M. Fukutomi, K. Komori, K. Togano, K. Maeda, Physica C **224**, 286 (1994).

68. Y. Iijima, N. Tanabe, O. Kohno, and Y. Ikeno, Appl. Phys. Lett. **60**, 769, 1992.

69. Y. Iijima, K. Onabe, N. Futaki, N. Sadakata and O. Kohno, J. Appl. Phys. Lett. **74**, 1905 (1993).

70. R. P. Reade, P. Burdahl, R. E. Russo and S. M. Garrison, Appl. Phys. Lett. **61**, 2231 (1993).

71. K. Fujino, K. Hasegawa, H. Mukai, K. Sato, T. Hara, T. Ohkuma, H. Ishii, S. Honjo, Proc. of the 8th International Symposium on Superconductivity (ISS'95), Hamamatsu, 67(1995).

72. K. Hasegawa, N. Yoshida, K. Fujino, H. Mukai, K. Hayashi, K. Sato, S. Honjo, Y. Sato, T. Ohkuma, H. Ishii, Y. Iwata, and T. Hara, Proc. of the 9th International

Symposium on Superconductivity (ISS'96), Sapporo, Oct. 21-24 (1996).

73. A. Goyal, D. P. Norton, J. D. Budai, M. Paranthaman, E. D. Specht, D. M. Kroeger, D. K. Christen, Qing He, B. Saffian, F. A. List, D. F. Lee, P. M. Martin, C. E. Klabunde, E. Hatfield and V. K. Sikka, Appl. Phys. Lett. **69**, 1795 (1996).

74. D. P. Norton, A. Goyal, J. D. Budai, D. K. Christen, D. M. Kroeger, E. D. Specht, Qing He, B. Saffian, M. Paranthaman, C. E. Klabunde, D. F. Lee, B. C. Sales, and F. A. List, Science, **274**, 755 (1996).

75. Qing He, D. K. Christen, J. D. Budai, E. D. Specht, D. F. Lee, A. Goyal, D. P. Norton, M. Paranthman, F. A. List, and D. M. Kroeger, Physica C, **275**, 155-161 (1997).

76. M. Paranthaman, A. Goyal, F. A. List, E. D. Specht, D. F. Lee, P. M. Martin, Qing He, D. K. Christen, D. P. Norton, and J. D. Budai, Physica C, **275**, 266 (1997).

77. D. K. Christen, D. P. Norton, A. Goyal, Qing He, C. E. Klabunde, D. M. Kroeger, M. Paranthaman, B. Saffian, and E. D. Specht, Czech. J. Phys. **46**, Suppl., 1531 (1996).

78. M. Paranthaman, A. Goyal, D. E. Heatherly, and D. M. Kroeger, IEEE Trans. Appl. Supercond. (In press)

79. W. L. Holstein, J. Phys. Chem. **97**, 4224 (1993).

80. A. Goyal, E. D. Specht, D. M. Kroeger, J. E. Tkacyzk, C. L. Briant and J. A. Deluca, Appl. Phys. Lett. **67**, 2563 (1996).

81. A. Goyal, E. D. Specht, D. M. Kroeger, T. A. Mason, D. J. Dingley, G. N. Riley

Jr., and M. W. Rupich, Appl. Phys. Lett. **66**, 2903 (1995).

82. D. H. Kim, K. E. Gray, R. T. Kampwirth, J. C. Smith, D. S. Richeson, T. J. Marks, J. H. Kang, J. Talvacchio, and M. Eddy, Physica C **177**, 431 (1991).

83. Qing He, D. K. Christen, C. E. Klabunde, J. E. Tkaczyk, K. W. Lay, M. Paranthaman, J. R. Thompson, A. Goyal, A. J. Pedraza, and D. M. Kroeger, Appl. Phys. Lett. **67**, 294 (1995).

84. J. D. Budai, R. T. Young, and B. S. Chao, Appl. Phys. Lett. **62**, 1836 (1993).

85. Chunyan Tian, Yang Du, and Siu-Wai Chan, MRS Proceeding, Vol. 355 on Evolution of Thin Film and Surface Structure and Morphology, edited by B. G. Demczyk, *et al.*, 1995, ISDN: 1-55899-256-1.

86. T. B. Reed, Free Energy of Formation of Binary Compounds, published by MIT Press, Cambridge, MA, (1971).

87. B. A. Movchan and A. V. Demchishin, Phys. Met. Metallogr. **28**, 83 (1969).

88. J. A. Thornton, Ann. Rev. Mater. Sci. 7, 239 (1977).

89. K. M. Satyalakshmi, R. M. Mallya, K. V. Ramananthan, X. D. Wu, B. Brainard, D. C. Gautier, N. Y. Vasanthacharya and M. S. Hegde, Appl. Phys. Lett. **62** (11), 1223 (1993).

90. Hidehito Obayashi, and Tetsuichi Kudo, Japanese Journal of Applied Physics, **14** (3), 1112 (1975).

91. D. P. Norton, A. Goyal, J. D. Budai, D. K. Christen, D. M. Kroeger, E. D. Specht, Qing He, B. Saffian, M. Paranthaman, C. E. Klabunde, D. F. Lee, B. C. Sales, and F. A. List, Science, **274**, 755 (1996).

92. J. D. Budai, R. T. Young, and B. S. Chao, Appl. Phys. Lett. **62**, 1836 (1993).

93. D. P. Norton et al., Appl. Phys. Lett. **57**, 1164 (1990).

94. D. H. Lowndes *et al.*, Phys. Rev. Lett. **74**, 2355 (1995).

95. R. P. Reade, P. Berdahl, R. E. Russo, S. M. Garrison, Appl. Phys. Lett. **61**, 2231 (1992).

96. X. D. Wu, S. R. Foltyn, P. N. Arendt, W. R. Blumenthal, I. H. Campbell, J. D. Cotton, J. Y. Coulter, W. L. Hults, M. P. Maley, H. F. Safar and J. L. Smith, Appl. Phys. Lett. **67**, 2397 (1995).

97. S. Kobayashi, T. Kaneko, T. Kato, J. Fujikami, K. Sato, Physica C **258**, 336 (1996).

98. J. E. Tkaczyk *et al.*, Appl. Phys. Lett. **62**, 3031 (1993).

99. G. Blatter, M. V. Feigel'man, V. B. Geshkenbein, A. I. Larkin, V. M. Vinokur, Reviews of Modern Physics, **66** (4), 1125 (1994).

APPENDICES

1. Calculation of the depairing current density J_0 value at 0 K

Some basic Ginzburg-Landau expressions are from reference.[99]

Since

$$H_{c_2}=\frac{\Phi_0}{2\pi\xi^2}$$

and

$$H_c=\frac{\Phi_0}{2\sqrt{2}\pi\lambda\xi}$$

where H_{c2} is upper critical magnetic field, H_c is thermodynamic critical magnetic field, λ is GL penetration depth, and ξ is GL coherence length. Φ_0 is the flux quantum, equal to 2.07×10^{-7} G-cm^2. Therefore, we get the depairing current density J_0 value at 0 K for each superconductor by using following formula (in cgs units). For practical laboratory units (currents in A/cm^2, fields in Gauss, and lengths in cm), one may replace the speed of light "c" with the value 10.

$$J_0=\frac{cH_c}{3\sqrt{6}\pi\lambda}=\frac{c}{6}\sqrt{\frac{\Phi_0}{6\pi}}\frac{\sqrt{H_{c_2}}}{\lambda^2}$$

2. Calculation of the depairing current density J_0 value at 77 K

From WHH theory, we have

$$H_{c_2}(0) = -0.69\left(\frac{dH_{c_2}}{dT}\right)T_c,$$

For temperature T above ~ 0.4 T where $H_{c2}(T)$ is approximately linear, we have

$$H_{c_2}(T) = (T_c - T)\left(\frac{dH_{c_2}}{dT}\right) = \frac{\Phi_0}{2\pi\xi^2(T)}.$$

The two fluid model provides that

$$\frac{1}{\lambda^2(T)} = \left[1 - \left(\frac{T}{T_c}\right)^4\right]\frac{1}{\lambda^2(0)}$$

$$J_0(T) = \frac{c}{3\sqrt{6\pi}}\frac{H_c}{\lambda(T)} = \frac{c}{3\sqrt{6\pi}}\frac{\Phi_0}{2\sqrt{2\pi}}\frac{1}{\xi(T)\lambda^2(T)}$$

Combining the above four equations, we get the depairing current density J_0 value at 77 K.

$$J_0(T) = \sqrt{\frac{c^2 H_{c_2}(0)(T_c - T)\Phi_0}{0.69\times\pi^3\times 9\times 24\times T_c}\left[1 - \left(\frac{T}{T_c}\right)^4\right]\frac{1}{\lambda^2(0)}}$$

3. Calculation of the lattice mismatches

The lattice mismatch between a candidate buffer layer and YBCO is expressed as

$$\frac{a^* - a^*_{YBCO}}{a^*_{YBCO}}\%$$

and the lattice mismatch between a candidate buffer layer and Ni is expressed as

$$\frac{a^* - a_{Ni}}{a_{Ni}}\%$$

where the a^* is chosen as either buffer layer lattice parameter a or $a/\sqrt{2}$ and the a^*_{YBCO} is selected as either a = 3.836 Å or b = 3.883 Å based on the achievement of smaller lattice mismatch.

VITA

Qing He was born in Hunan province, China, on September 26, 1959. He received his basic education in Shenyang, Liaoning province. After one-year farm-work like all the Chinese youth at that time, he entered the Northeast University of Technology in 1978 and received a Bachelor of Science degree in Materials Science in 1982. From 1982 to 1986, he did research works on non-ferrous metals in the General Research Institute for Non-ferrous metals (GRINM) in Beijing. In 1986, he entered the graduate school of GRINM and was awarded a Master degree on Materials Science and Engineering three years later. He then took a position of a research engineer in the Department of Superconductivity in GRINM.

In August of 1992, he received a research assistantship and resumed his graduate study toward a Doctor of Philosophy degree at the University of Tennessee, Knoxville. He has performed research in the Solid State Division, Oak Ridge National Laboratory since November of 1992. He expects to receive the Doctor of Philosophy degree with a major in Materials Science and Engineering in Dec., 1997.

Qing He is a member of Sigma Xi Scientific Society, Materials Research Society, and American Physical Society. He holds one patent (US Patent No. 5646097) and is co-inventor on two pending patent applications. He is author or coauthor of 76 journal papers and presentations on films, superconductors, metals and ceramics.